U.S.NRC
United States Nuclear Regulatory Commission
Protecting People and the Environment

NUREG/CR-7137
ANL-10/36

Stress Corrosion Cracking in Nickel-Base Alloys 690 and 152 Weld in Simulated PWR Environment - 2009

Office of Nuclear Regulatory Research

AVAILABILITY OF REFERENCE MATERIALS IN NRC PUBLICATIONS

NRC Reference Material

As of November 1999, you may electronically access NUREG-series publications and other NRC records at NRC's Public Electronic Reading Room at http://www.nrc.gov/reading-rm.html. Publicly released records include, to name a few, NUREG-series publications; *Federal Register* notices; applicant, licensee, and vendor documents and correspondence; NRC correspondence and internal memoranda; bulletins and information notices; inspection and investigative reports; licensee event reports; and Commission papers and their attachments.

NRC publications in the NUREG series, NRC regulations, and *Title 10, Energy*, in the Code of *Federal Regulations* may also be purchased from one of these two sources.

1. The Superintendent of Documents
   U.S. Government Printing Office
   Mail Stop SSOP
   Washington, DC 20402–0001
   Internet: bookstore.gpo.gov
   Telephone: 202-512-1800
   Fax: 202-512-2250
2. The National Technical Information Service
   Springfield, VA 22161–0002
   www.ntis.gov
   1–800–553–6847 or, locally, 703–605–6000

A single copy of each NRC draft report for comment is available free, to the extent of supply, upon written request as follows:

Address: U.S. Nuclear Regulatory Commission
Office of Administration
Publications Branch
Washington, DC 20555-0001
E-mail: DISTRIBUTION.RESOURCE@NRC.GOV
Facsimile: 301–415–2289

Some publications in the NUREG series that are posted at NRC's Web site address http://www.nrc.gov/reading-rm/doc-collections/nuregs are updated periodically and may differ from the last printed version. Although references to material found on a Web site bear the date the material was accessed, the material available on the date cited may subsequently be removed from the site.

Non-NRC Reference Material

Documents available from public and special technical libraries include all open literature items, such as books, journal articles, and transactions, *Federal Register* notices, Federal and State legislation, and congressional reports. Such documents as theses, dissertations, foreign reports and translations, and non-NRC conference proceedings may be purchased from their sponsoring organization.

Copies of industry codes and standards used in a substantive manner in the NRC regulatory process are maintained at—

The NRC Technical Library
Two White Flint North
11545 Rockville Pike
Rockville, MD 20852–2738

These standards are available in the library for reference use by the public. Codes and standards are usually copyrighted and may be purchased from the originating organization or, if they are American National Standards, from—

American National Standards Institute
11 West 42nd Street
New York, NY 10036–8002
www.ansi.org
212–642–4900

Legally binding regulatory requirements are stated only in laws; NRC regulations; licenses, including technical specifications; or orders, not in NUREG-series publications. The views expressed in contractor-prepared publications in this series are not necessarily those of the NRC.

The NUREG series comprises (1) technical and administrative reports and books prepared by the staff (NUREG–XXXX) or agency contractors (NUREG/CR–XXXX), (2) proceedings of conferences (NUREG/CP–XXXX), (3) reports resulting from international agreements (NUREG/IA–XXXX), (4) brochures (NUREG/BR–XXXX), and (5) compilations of legal decisions and orders of the Commission and Atomic and Safety Licensing Boards and of Directors' decisions under Section 2.206 of NRC's regulations (NUREG–0750).

DISCLAIMER: This report was prepared as an account of work sponsored by an agency of the U.S. Government. Neither the U.S. Government nor any agency thereof, nor any employee, makes any warranty, expressed or implied, or assumes any legal liability or responsibility for any third party's use, or the results of such use, of any information, apparatus, product, or process disclosed in this publication, or represents that its use by such third party would not infringe privately owned rights.

U.S.NRC
United States Nuclear Regulatory Commission
Protecting People and the Environment

NUREG/CR-7137
ANL-10/36

Stress Corrosion Cracking in Nickel-Base Alloys 690 and 152 Weld in Simulated PWR Environment - 2009

Manuscript Completed: June 2012
Date Published: June 2012

Prepared by
B. Alexandreanu, Y. Yang, Y. Chen, and W. J. Shack

Argonne National Laboratory
Argonne, IL 60439

Darrell Dunn/Appajosula Rao, NRC Project Managers

Office of Nuclear Regulatory Research

Abstract

Alloys 600 and 182 are used as structural materials in pressurized water reactors (PWRs) and have been found to undergo stress corrosion cracking (SCC). Alloys 690 and 152 are the replacement materials of choice for Alloys 600 and 182, respectively. The primary objective of this work is to determine the crack growth rates (CGRs) in a simulated PWR water environment for the replacement alloys. This is an ongoing effort, and the report presents the initial investigations on Alloys 690 and 152 weld. A second objective was to obtain tensile data for these alloys for a wide temperature range, from operating to extreme conditions. To meet the objectives, testing conducted at ANL included Alloy 690 in the as-received condition and cold-rolled by 26%, as well as a laboratory-prepared Alloy 152 double-J weld in the as-welded condition. For the SCC CGR measurements, the specimens were pre-cracked under cyclic loading in a primary water environment, and the cyclic CGRs were monitored to determine the transition from the fatigue transgranular fracture mode to the intergranular SCC fracture mode. The cyclic CGRs of the cold-rolled Alloy 690 showed significant environmental enhancement compared with the as-received alloy. Compared to Alloy 600, the as-received Alloy 690 proved to be more resistant to SCC in the simulated PWR environment at 320°C (608 °F), with SCC CGRs of 10^{-12} m/s. However, the SCC CGRs for the cold-rolled alloy were an order of magnitude higher, about 10^{-11} m/s, at comparable stress intensity factors in the range of 22 to 32 $\mathrm{MPa{\cdot}m^{1/2}}$ (20 to 29 $\mathrm{ksi{\cdot}in.^{1/2}}$). This finding is consistent with results obtained by industry on similar cold-worked alloys. A possible explanation for the relatively high CGRs in the cold-worked material is the presence of cracked grain boundary carbides, a feature that was observed for all cold-worked alloys displaying relatively high CGRs. The environmental enhancement of cyclic CGRs for Alloy 152 was minimal; nevertheless, the transition from transgranular to intergranular cracking was successful. Weld samples tested from a single heat of Alloy 152 exhibited SCC CGR rates of 10^{-11} m/s in the simulated PWR environment at 320°C (608 °F), which was only about an order of magnitude lower than typical for Alloy 182. The report also presents tensile property data for Alloy 690 and Alloy 152 welds in the temperature range of 25-870°C (81-1598°F). These data meet the minimum requirements of ASME SB-167, and are in excellent agreement with data on similar alloys.

Foreword

Primary water stress corrosion cracking (PWSCC) is a significant issue that has affected nickel base alloy pressurized-water reactor (PWR) components. Observation of PWSCC in the past decade has challenged the assumptions of leak before break analyses that were based on evaluations that did not consider PWSCC as a degradation mechanism that may contribute to potential sources of pipe rupture and subsequently a loss of coolant accident. Operational experience has also shown that PWSCC of penetrations in the reactor pressure vessel head lead to boric acid corrosion of low-alloy pressure vessel steels.

The U.S. Nuclear Regulatory Commission (NRC) mandated that inspections are required for reactor coolant system components constructed from PWSCC susceptible materials, including Alloy 600 and its weld metals, Alloys 182 and 82. These inspections result in occupational exposures and are also both difficult to conduct and costly to implement. Consequently, the industry has proposed methods for PWSCC mitigation such as the use of replacement components manufactured from Alloy 690 and its weld metals, Alloys 152 and 52. Limited operational experience with these higher chromium containing alloys in thick section pressure boundary components has been favorable. However, the effects of fabrication processes on alloy microstructure and PWSCC susceptibility are not fully understood. Ongoing industry research is being conducted to evaluate metallurgical and environmental effects that influence PWSCC resistance. Confirmatory testing sponsored by the NRC is being conducted to verify improvement factors and determine acceptable inspection intervals for components manufactured from the higher chromium-containing alloys.

This report documents work conducted by Argonne National Laboratory (ANL) during calendar years 2008 and 2009 under contract to the NRC. Testing conducted at ANL during this period consisted of microstructural analyses and crack growth rate tests to measure the PWSCC resistance of cold-worked Alloy 690. In addition, microstructural analysis and tests to determine mechanical properties and crack growth rates for an Alloy 152 weld were conducted. Results of these tests indicate that Alloy 690 in the as-received and cold-worked conditions was more resistant to PWSCC compared to Alloy 600. However, results obtained by Bettis Atomic Power Laboratory show that some heats of Alloy 690 in the cold-worked condition have crack growth rates that are greater than those measured for Alloy 600. While results with the Alloy 152 weld metal show improved PWSCC resistance compared to Alloy 182, the measured crack growth rates on limited tests with Alloy 152 were greater than the rates reported by industry and other testing laboratories.

Additional testing will be conducted to evaluate factors that affect PWSCC resistance that may contribute to the range of measured crack growth rates. These tests will include multiple heats of Alloy 690 and 152 weld metals. In addition, the microstructure of cold-worked materials may be similar to weld heat affected zones (HAZ). Subsequent tests will be conducted to determine the microstructural characteristics and crack growth rates in Alloy 690 weld HAZs.

Michael J. Case, Director
Division of Engineering
Office of Nuclear Regulatory Research
U.S. Nuclear Regulatory Commission

Contents

Figures

Tables

Executive Summary

Nickel-base Alloy 600 used as construction material in light water reactors (LWRs) has experienced stress corrosion cracking (SCC). Such cracking was first observed in steam generator tubes, but it has also occurred in components such as instrument nozzles and heater thermal sleeves in the pressurizer and penetrations for control-rod drive mechanisms (CRDM) in the reactor-vessel closure heads. In operating plants, weld Alloys 82 and 182 have been used with Alloy 600; however, less cracking has been observed in the weld materials than in the Alloy 600 wrought material. During the last twenty years, thin-walled steam generator tubing for PWRs has been fabricated from the higher-chromium material, Alloy 690. Only in the last decade has this material begun to be used for thick-section components, particularly nozzle penetrations, during the replacement of heads for reactor pressure vessels. This increased use of Alloy 690 has necessitated the use of the weld Alloys 52 and 152, which also have high chromium content.

The main objectives of the current work are to determine the SCC and cyclic crack growth rates (CGRs) in Alloy 690 and its associated weld materials, and to obtain tensile data for these alloys over a wide temperature range, from operating to extreme conditions. The CGR work is complemented by metallographic examinations conducted to understand the observed CGR behavior.

The following observations were made from the metallographic examinations. The microstructure of Alloy 690 plate cold-rolled by 26% contained TiN inclusions and cracked boundary carbides. The areas close to the two edges of the plate were decorated with carbide streaks – regions with thick grain boundary carbides. In addition, grain size banding was observed near both the edges. The mid-plane of the plate – the region where the material for CGR test specimens was obtained – was free of carbide streaks and grain size banding. The SCC-resistant coincident site lattice boundary (CSLB) fraction was approximately 28%, which is much less than is typical for a Ni-base alloy in this condition. Hence, the proportion of SCC-susceptible random boundaries was approximately 50% higher than in a typical alloy. The microstructure of the second heat of Alloy 690, actually a piece of CRDM tubing, had equiaxed grains and dense grain boundary carbide coverage. The grain boundary character distribution was typical of a conventionally fabricated Ni-base alloy component. The CSLB was approximately 53%, of which a large proportion was twins. The microstructure of Alloy 152 was also found to be typical of a Ni-base alloy weld. Transmission electron microscopy revealed Al-oxide inclusions. The grain boundary character distribution was also typical of a Ni-base alloy weld. The CSLB fraction was approximately 42%, of which a large proportion was low angle boundaries.

The tensile tests, which were conducted in the temperature range 25-870°C (77-1598°F), showed that the tensile properties of the alloys meet the minimum requirements of ASME SB-167, and that they are in good agreement with the properties measured elsewhere on similar alloys. As such, the data set for Alloy 690 is in good agreement with control data on Alloy 600. Similarly, the data set for Alloy 152 is in good agreement with the Alloy 82/152 tensile data obtained elsewhere.

The cyclic CGRs for Alloy 690 cold-rolled by 26% showed significant environmental enhancement, comparable to that observed for a heat of Alloy 600 from the Davis-Besse reactor. In the as-received condition, the cyclic CGRs for the alloy showed some environmental enhancement, although much less than that for the cold-rolled alloy. Moreover, the cyclic CGRs for the as-received alloy appeared to be smaller than the corresponding rates for Alloy 600. Hence, it is expected that Alloy 690 in the as-received condition is more resistant to SCC than Alloy 600.

The SCC CGRs in the PWR environment at 320°C (608°F) for Alloy 690 cold-rolled by 26% were 1-3 x 10^{-11} m/s for moderate stress intensity factors, about an order of magnitude lower than those typical for as-received Alloy 600. The SCC CGRs for as-received Alloy 690 were about an order of magnitude lower, 2-4 x 10^{-12} m/s The data obtained at ANL are in good agreement with data obtained on similar alloys with cold-working in the 20-32% range due to either cold-rolling or tensile pre-straining at other laboratories. The cracked grain boundary carbides appear to be a common feature of all cold-worked alloys that display relatively high CGRs. These results imply that while Alloy 690 in the as-received condition is more resistant to SCC compared to Alloy 600, cold work can increase SCC susceptibility.

The available data on the temperature dependence of SCC CGRs obtained at Argonne National Laboratory and elsewhere were analyzed to investigate the activation energy for SCC growth rates. The results indicated that the activation energy for Alloy 690 is strongly affected by the deformation level of the alloy. Alloys in the as-received condition and at deformation levels of up to 20% cold work have an activation energy close to that for Alloy 600 (130 kJ/mol). At higher deformation levels (24-26%), CGRs are not strongly dependent on temperature. This observation is consistent with the results of other testing laboratories, which show that with 50% cold work, the temperature appears to have little effect on SCC CGRs.

The cyclic CGR data for the two Alloy 152 specimens tested suggest that specific loading conditions can lead to environmental enhancement. However, the enhanced rates were always lower than the corresponding rates for Alloys 82/182. Hence, it is expected that Alloy 152 is more resistant to SCC than Alloys 82/182. The measured SCC CGRs in PWR environment at 320°C (608°F) for as-welded Alloy 152 were 1.6-5 x 10^{-11} m/s for moderate stress intensity factors, about an order of magnitude lower than those typical for Alloy 182.

Acknowledgments

The authors thank E. Listwan and W. Soppett and their contributions to the experimental effort. This work is sponsored by the Office of Nuclear Regulatory Research, U.S. Nuclear Regulatory Commission, under Job Code N6519; Program Managers: Darrell Dunn and Appajosula Rao.

Acronyms and Abbreviations

ANL	Argonne National Laboratory
ASTM	American Society for Testing and Materials
B&W	Babcock and Wilcox
BPR	Back Pressure Regulator
BWR	Boiling Water Reactor
C	Circumferential
CGR	Crack Growth Rate
CL	Constant Load
CRDM	Control Rod Drive Mechanism
CSL	Coincident Site Lattice
CSLB	Coincident Site Lattice Boundary
CT	Compact Tension
DO	Dissolved Oxygen
ECP	Electrochemical Potential
EDS	Energy Dispersive X-ray Spectroscopy
EPRI MRP	Electric Power Research Institute Materials Reliability Program
GBCD	Grain Boundary Character Distribution
GTA	Gas Tungsten Arc
GTAW	Gas Tungsten Arc Welding
HAB	High-Angle Boundary
HAZ	Heat Affected Zone
HX	Heat Exchanger
ICP-OES	Inductively-Coupled Plasma Optical Emission Spectrometry
IG	Intergranular
L	Longitudinal
LWR	Light Water Reactor
MA	Mill Annealed
NRC	Nuclear Regulatory Commission
OIM	Orientation Imaging Microscopy
PWR	Pressurized Water Reactor
PWSCC	Primary Water Stress Corrosion Cracking
R	Radial
RA	Reduction in Area
S	Side
SA	Solution Annealed
SCC	Stress Corrosion Cracking

SEM	Scanning Electron Microscopy
SHE	Standard Hydrogen Electrode
SMA	Shielded Metal Arc
SMAW	Shielded Metal Arc Welding
SS	Stainless Steel
T	Transverse
TC	Thermocouple
TEM	Transmission Electron Microscopy
TG	Transgranular
TT	Thermally Treated
UTS	Ultimate Tensile Strength
YS	Yield Strength

1 Introduction

Nickel-base Alloy 600 used as construction material in light water reactors (LWRs) has experienced stress corrosion cracking (SCC). Such cracking was first observed in steam generator tubes, but it has also occurred in components such as instrument nozzles and heater thermal sleeves in the pressurizer and penetrations for control-rod drive mechanisms (CRDM) in the reactor-vessel closure heads. In operating plants, weld Alloys 82 and 182 have been used with Alloy 600; however, less cracking has been observed in the weld materials than in the Alloy 600 wrought material.[1] During the last twenty years, thin-walled steam generator tubing for PWRs has been fabricated from the higher-chromium material, Alloy 690. This material has only in the last decade begun to be used for thick-section components, particularly nozzle penetrations, during the replacement of heads in reactor pressure vessels. This increased use of Alloy 690 has necessitated the use of the weld Alloys 52 and 152, which have equivalent high chromium content.

A program is under way at Argonne National Laboratory (ANL) to evaluate the resistance of Ni alloys and their welds to environmentally assisted cracking in simulated coolant environments for light water reactors. To date, CGR tests have been performed on Alloys 600 and 690,[2-7] laboratory-prepared deep-groove and double-J welds of Alloy 182,[8] Alloy 600 from Davis–Besse CRDM Nozzle #3, Alloy 182 from a J-groove weld in Davis–Besse Nozzle #11, and Alloys 182 and 82 from a hot-leg nozzle-to-pipe weld in the V. C. Summer reactor coolant system.[9] During the last three years, the research has focused on understanding the cracking behavior of Alloy 690 and its welds.

The main objectives of the current work are to determine the SCC and cyclic crack growth rates (CGRs) in Alloy 690 and its associated weld materials, and to obtain tensile data for these alloys over a wide temperature range, from operating to extreme conditions. The CGR work is complemented by metallographic examinations conducted to understand the observed CGR behavior. Two heats of Alloy 690 were procured, and one Alloy 152 weld was produced specifically for this program. The CGR testing approach consists of precracking in the test environment, followed by a loading sequence conducted with the purpose of transitioning from the transgranular (TG) fatigue fracture mode to an intergranular (IG) SCC fracture mode. In essence, the cyclic CGRs are monitored for environmental enhancement, that is, for conditions where the measured CGRs are larger than the rates expected in air under the same loading conditions. An enhanced CGR signifies that in addition to the mechanical component, the measured CGR also has an environmental component (corrosion fatigue or SCC). The SCC components are isolated by introducing increasing hold times and by setting the specimen at constant load. In this approach, precracking in the environment is an important step as these early data points provide a baseline against which environmental enhancement is subsequently measured.

The complementary metallographic examinations were focused on features known from previous Alloy 600/182 experience to affect the SCC behavior. These examinations consist of scanning electron microscopy (SEM) for the analysis of elemental distribution and general microstructure, orientation imaging microscopy (OIM) for the determination of grain boundary characteristics, and transition electron microscopy (TEM) with emphasis on the nature of grain boundary carbides.

2 Experimental

2.1 Materials

The CGR tests were performed on two heats of Alloy 690 and one of Alloy 152 weld. One heat of Alloy 690 was in plate form, and the other was in CRDM tubing form. The Alloy 152 weld was prepared in a double-J geometry at ANL Central Shops.

Alloy 690 (Heat NX3297HK12) was received from Nuclear Alloy Corp. in a plate form that was 6.4-cm (2.25-in.) thick x 7.6-cm (3-in.) wide x 86.4-cm (34-in.) long. The designation for the metallurgical condition of the as-received plate was MIL-DTL-24802. To reach this condition, the alloy was vacuum-induction-melted, electro-slag-remelted, hot-rolled, de-scaled, and annealed at 1038°C (1900°F) for 2 h, then air-cooled. The chemical composition provided by the vendor, as well as that determined at ANL by inductively-coupled plasma optical emission spectrometry (ICP-OES), is reported in Table 1.

Table 1. Chemical composition (wt.%) of Alloy 690 (Heat NX3297HK12) plate.

Alloy ID (Heat)	Analysis	C	Mn	Fe	S	P	Si	Cu	Ni	Cr	Ti	Nb	Co
A 690WC (NX3297HK12)	Vendor	0.03	0.20	9.9	<0.001	-	0.07	0.01	59.5	29.5	-	-	-
	ANL	0.04	0.33	8.53	0.001	0.003	0.02	0.04	59.67	30.82	0.47	0.01	<0.01

For the CGR tests, the plate was further cold-rolled at room temperature at Special Metals Corp. to reduce the thickness by 26%. The desired reduction was achieved in three passes (10, 8, and 8%). The test plane of interest was the mid-plane of the plate because of its uniform distribution of cold work. The dimensions of this plate and desired orientations necessitated the use of the small (½-T) compact tension (CT) specimens. Four such specimens were machined in two orientations, side longitudinal (SL) and side transverse (ST), as shown in Fig. 1. These specimens are designated A690WC-orientation-number.

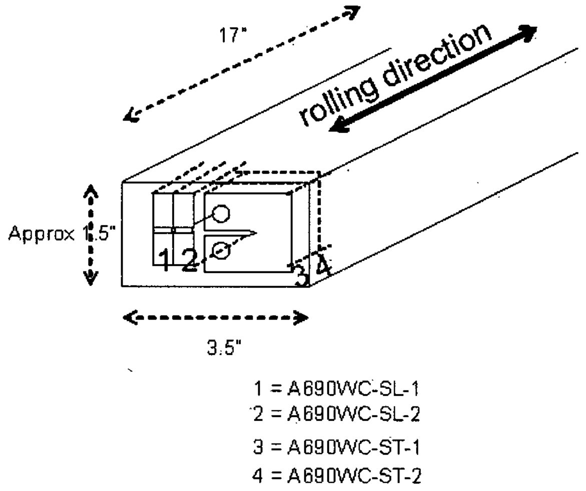

Figure 1.
Orientation of Alloy 690 specimens machined from cold-rolled plate.

The second heat of Alloy 690 used for CGR testing was received in CRDM tubing form. The piece of CRDM tubing was marked "2541 – Heat WP142" and was supplied by Valinox Nucleaire (Fig. 2). As with the plate material, the thickness of the tube necessitated the use of the small ½-T CT specimens. In order to obtain a thickness large enough to fabricate these specimens, a ring was cut from the tubing, and the interior surface was built up with Alloy 152 by the shielded metal arc (SMA) method, as shown in Fig. 3 and Table 2. Four ½-T CT specimens were machined in two orientations, circumferential radial (CR) and longitudinal radial (LR), as shown in Fig. 2. These specimens are designated C690-orientation-number.

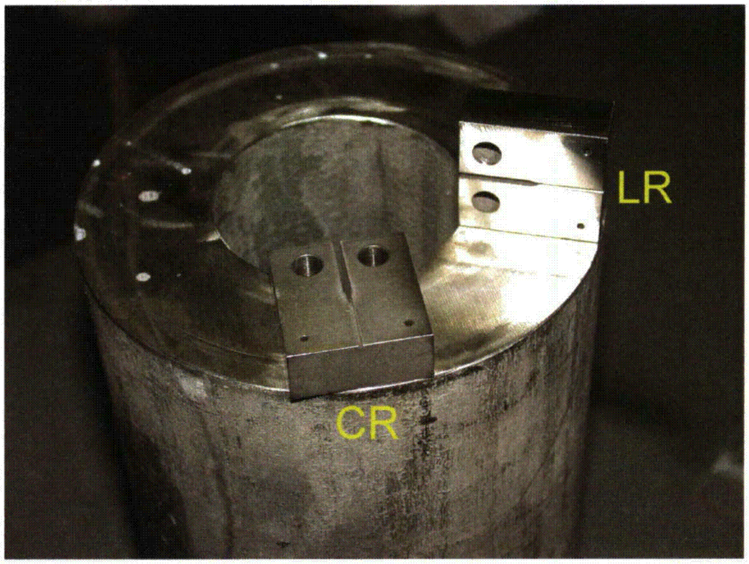

Figure 2.
Orientation of the Alloy 690 specimens cut from the CRDM nozzle.

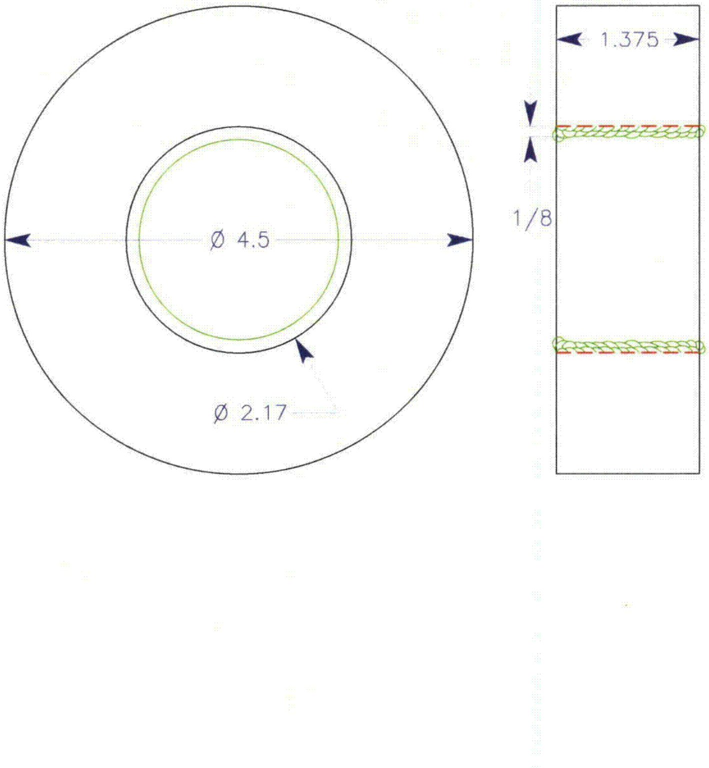

Figure 3.
Schematic of the Alloy 152 weld build-up on the interior of the Alloy 690 CRDM tube.

Table 2. Welding process and conditions used to build up the interior of the Alloy 690 CRDM tube.

Weld Pass	Process	Filler Metal	Heat Code	Filler Size, in.	Current, A	Voltage, V	Travel Speed, in./min
1 - 2	SMA	Alloy 152 (A5.11M-97 ENiCrFe-7)	WC43E9	3/32	55 - 60	21 - 23	6 - 7

The chemical composition of Alloy 690, determined by an ICP-OES analysis conducted at ANL, is shown in Table 3.

Table 3. Chemical composition (wt.%) of Alloy 690 (Heat WP142) in CRDM tubing form.

Alloy ID (Heat)	Analysis	C	Mn	Fe	S	P	Si	Cu	Ni	Cr	Ti	Nb	Co
C690 (WP142)	Vendor	0.018	0.311	10.02	0.0006	0.006	0.296	<0.05	59.71	29.15	0.240	<0.005	0.007
	ANL	-	0.28	9.26	-	<0.05	0.40	<0.05	54.0	27.3	0.3	<0.07	<0.05

The Alloy 152 was fabricated at ANL Central Shops by shielded metal arc welding (SMAW) in a double-J geometry (Fig. 4) following a procedure developed to be consistent with the American Society of Mechanical Engineers (ASME) Boiler and Pressure Vessel Code, Section IX; however, this procedure was not qualified by non-destructive examination, tensile tests, and side bend tests. The weld was produced by joining two Alloy 690 plates (Heat NX3297HK12, described previously) and was prepared by 96 weld passes. Root passes 1 to 5 were made by gas tungsten arc welding (GTAW) with Alloy 52 filler, and the other passes were made by SMAW with Alloy 152 filler. The conditions for each weld pass are listed in Table 4. During welding, the maximum inter-pass temperature was≈120°C (250°F). The weld surfaces were cleaned by wire brushing and grinding, and were rinsed with de-mineralized water or alcohol. The chemical composition of the Alloy 152 weld wire supplied by the vendor and that obtained by ICP-OES analysis of the as-deposited weld are given in Table 5.

The size of the double-J weld allowed for larger (1-T) CT specimens. These were cut from the bottom weld shown schematically in Fig. 4 in the transverse side (TS) orientation, with the notch about 5 mm (0.2 in.) into the weld. This specimen geometry ensured that the CGR tests were conducted in the region of the weld made with a single Alloy 152 heat, WC04F6. These specimens are designated A152-orientation-number.

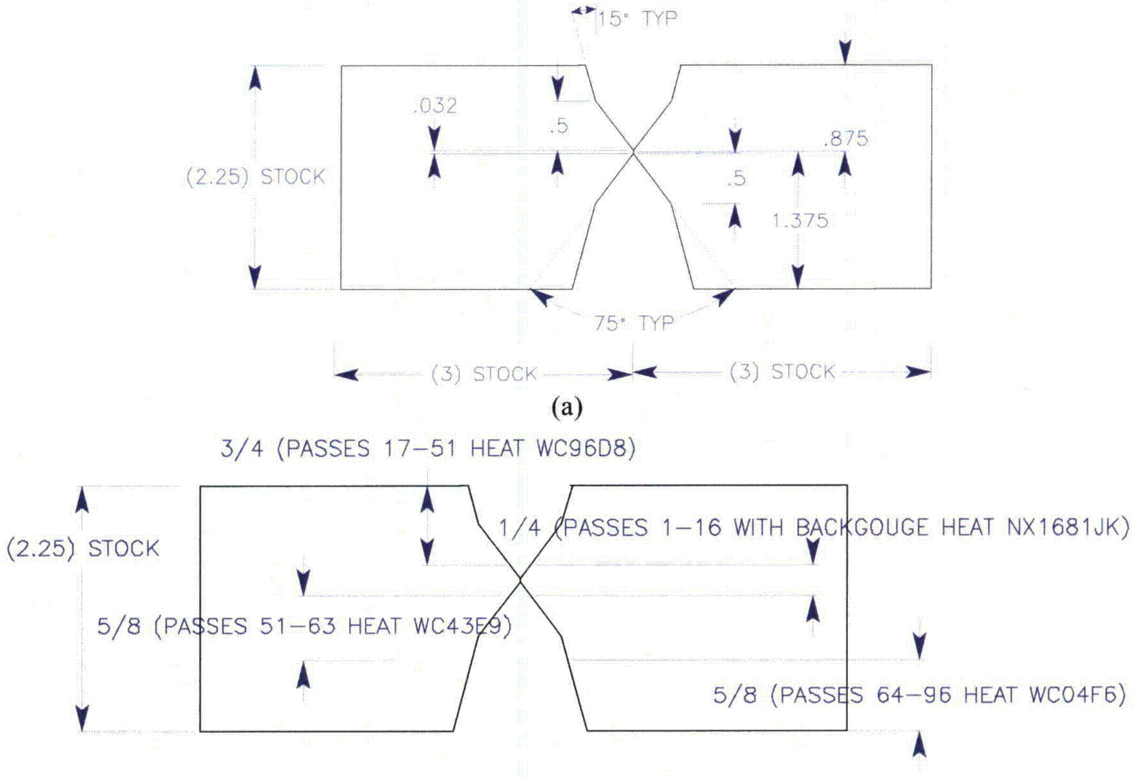

(a)

(b)

Figure 4. Schematic of the weld joint design for the (a) Alloy 152 double-J weld and (b) weld passes and filler heats used. Dimensions are in inch.

Table 4. Welding process and conditions for various weld passes used for fabricating the A152 weld.

Weld Pass	Process	Filler Metal	Heat Code	Filler Size, in.	Current, A	Voltage, V	Travel Speed, in./min
1 - 16	GTA	Alloy 52 (A5.14M-97 ERNiCrFe-7)	NX1681JK	3/32	185-215	21 - 22	6 - 7
17 - 51	SMA	Alloy 152 (A5.11M-97 ENiCrFe-7)	WC96D8	1/8	100 - 110	23 - 25	7 -9
51 - 63	SMA	Alloy 152 (A5.11M-97 ENiCrFe-7)	WC43E9	3/32	55 - 60	22 - 23	6 - 7
64 - 96	SMA	Alloy 152 (A5.11M-97 ENiCrFe-7)	WC04F6	1/8	100 - 110	22 - 25	7 - 9

Table 5. Chemical composition (wt.%) of Alloy 152 weld wire (vendor) and as-deposited weld (ANL).

Alloy ID (Heat)	Analysis	C	Mn	Fe	S	P	Si	Cu	Ni	Cr	Ti	Nb	Co
A52 (NX168IJK)	Vendor	0.02	0.24	10.40	<0.001	0.005	0.12	0.01	59.30	28.68	0.52	<0.01	0.00
A152 (WC96D8)	Vendor	0.04	3.88	9.16	0.007	0.008	0.54	0.01	55.88	29.35	0.07	1.81	0.01
A152 (WC43E9)	Vendor	<0.03	3.95	10.25	<0.003	<0.005	0.51	0.01	54.16	28.60	0.08	1.93	0.01
A152 (WC04F6)	Vendor	0.048	3.48	10.39	0.003	0.003	0.41	<0.01	55.20	28.70	0.09	1.54	<0.005
	ANL	-	3.88	9.56	-	<0.08	0.52	<0.04	53.70	28.40	0.10	1.80	<0.04

2.2 Specimen Design

All crack growth rate tests on Ni alloys and Ni-base welds were conducted in simulated PWR environments at temperatures of 290-350°C in accordance with ASTM E-647, "Standard Test Method for Measurement of Fatigue Crack Growth Rates,"[10] and ASTM E-1681, "Standard Test Method for Determining a Threshold Stress Intensity Factor for Environment-Assisted Cracking of Metallic Materials under Constant Load."[11] Depending on the dimensions of the available materials, the tests were performed on either 1-T or ½-T CT specimens; the configurations of the CT specimens are shown in Fig. 5.

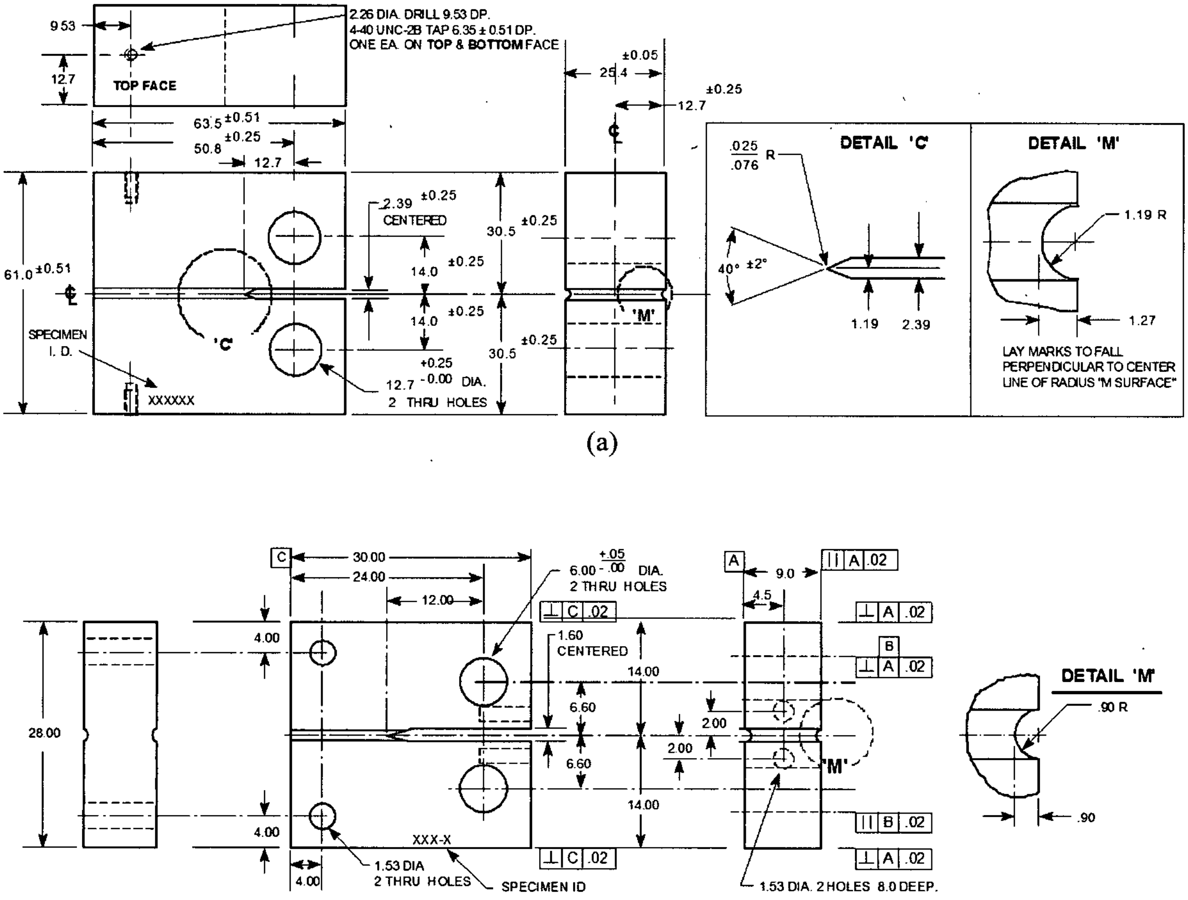

(a)

(b)

Figure 5. **Configuration of the (a) 1-T and (b) ½-T CT specimens used for this study. Dimensions are in mm.**

2.3 Test Facilities

The CGR tests were conducted in three test facilities – two equipped with 6-liter stainless steel (SS) autoclaves and one with a 2-liter SS autoclave. Each system has a suite of calibrated instrumentation, including digitally controlled hydraulic loading and load cells, and an independent water loop with water chemistry monitoring. Also, each system has a DC potential CGR measuring system.

2.3.1 Facility with 6-Liter Autoclave

The 6-liter autoclave facility is typically used for CGR tests at temperatures not exceeding 320°C (608°F). The facility consists of a closed-loop electro-hydraulic material test system equipped with an extended column load frame rated at 89 kN (20,000 lb) maximum. The Type 316 SS autoclave has a 175-mm (6.875-in.) outside diameter and is rated for a working pressure of 5050 psig (35 MPa) at 343°C (650°F). The load frame is accessorized with an Instron Model 8800 control console and a hydraulic pump. The autoclave is connected to a recirculating water system. The test facility also consists of a temperature control unit, a DC potential control console, a DC potential measurement unit, and a data acquisition and recording system. The autoclave, mounted within the load frame, has been modified to permit a ≈19-mm (0.75-in.) dia shaft to load the test specimen through a Bal-Seal® gland in the top of the autoclave cover.

The autoclave is continuously supplied with simulated primary water solution from a feedwater tank. Figure 6 shows a schematic diagram of the water system. The water system consists of a feedwater storage tank, high-pressure pump, regenerative heat exchanger, autoclave preheater, test autoclave, electrochemical potential (ECP) cell, regenerative heat exchanger, back-pressure regulator, and return line to the feedwater tank. The storage tank has a hydrogen cover gas to maintain a desired dissolved hydrogen concentration in the water. In the once-through mode, the return line is connected to the drain. Water is circulated at relatively low flow rates (15-25 mL/min).

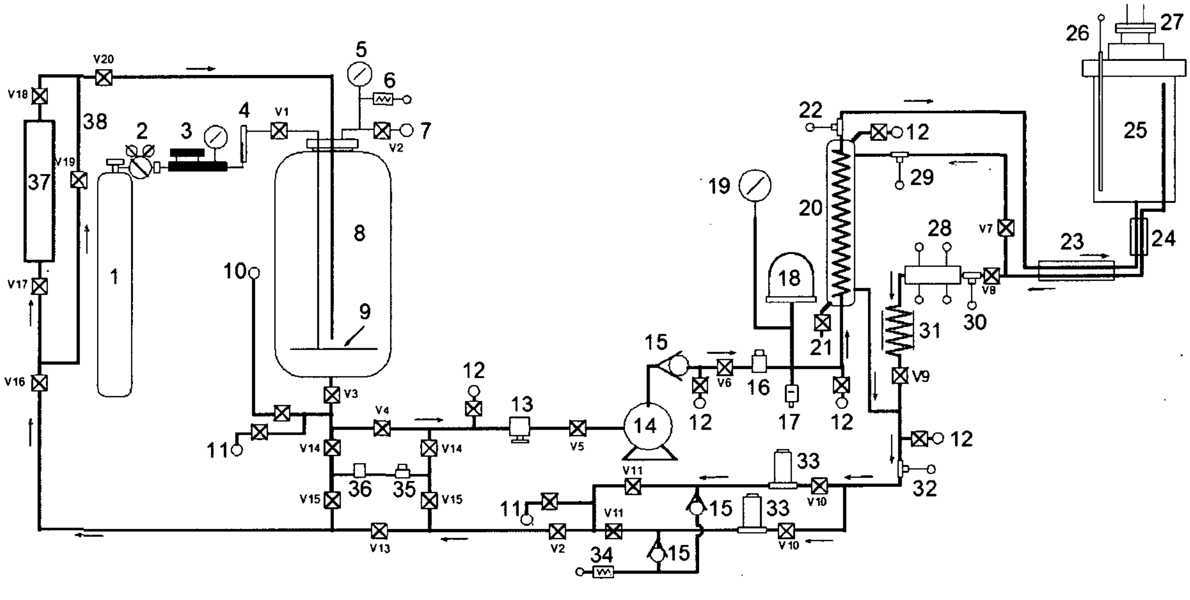

Figure 6. Schematic diagram of the recirculating 6-liter autoclave system.

1. COVER GASS SUPPLY TANK	20. HEAT EXCHANGER (HX)
2. TWO-STAGE HIGH-PRESSURE REGULATOR	21. DRAIN
3. LOW-PRESSURE REGULATOR	22. HX FEEDWATER OUTLET THERMOCOUPLE (TC)
4. FLOW METER	23. AUTOCLAVE & ECP CELL PREHEATER
5. COMPOUND VACUUM & PRESSURE GAUGE	24. HEAT EXCHANGER
6. PRESSURE RELIEF VALVE	25. COMMERCIAL AUTOCLAVE
7. VENT TO AIR & FLASH ARRESTOR	26. THERMOWELL
8. FEEDWATER STORAGE TANK	27. "BAL SEAL" RETAINER
9. SPARGE TUBE	28. ECP CELL
10. FEEDWATER FILL PORT	29. HX EFFLUENT INLET TC
11. WATER SAMPLE PORT	30. ECP CELL INLET TC
12. SYSTEM BLEED PORT	31. AIR-COOLED COIL
13. SOLENOID VALVE	32. BACK-PRESSURE REGULATOR (BPR)INLET TC
14. HIGH-PRESSURE PUMP	33. BPR
15. CHECK VALVE	34. PRESSURE RELIEF VALVE
16. PRESSURE TRANSDUCER	35. CONDUCTIVITY METER
17. RUPTURE DISC	36. PH METER
18. ACCUMULATOR	37. ION EXCHANGE BED
19. HIGH-PRESSURE GAUGE	38. ION EXCHANGE BED BYPASS LINE

Figure 6. (cont.)

2.3.2 Facility with a 2-Liter Autoclave

The 2-liter autoclave test facility was built by Cortest Inc. and allows test temperatures of up to 350°C (662°F). The servohydraulic test frame consists of a load cell, load train, autoclave, and furnace. The hydraulic actuator is mounted on bottom of the test frame, with the test train components suspended above it. The load cell is located at the bottom of the pull rod. An Instron Model 8800 control console is used to load the specimen. A 2-liter autoclave is installed inside the furnace for conducting tests in simulated LWR environments. The heater bands are mounted on the autoclave vessel. Figure 7 is a photograph showing the entire test system.

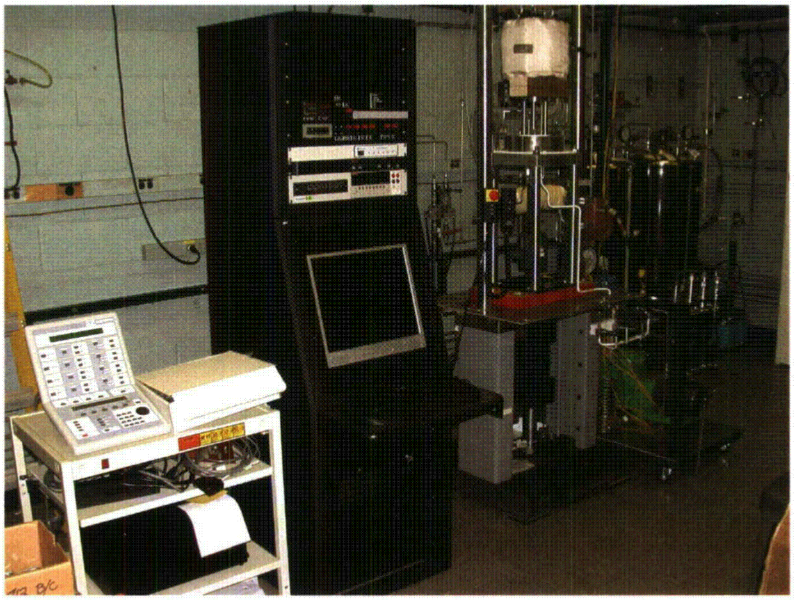

Figure 7. Layout of the 2-liter autoclave system.

The load cage that contains the test specimen consists of the cover plate of the autoclave and a thick bottom plate separated by four compression rods (Fig. 8). The lower two-piece clevis assembly is fastened to the bottom plate of the cage, and the upper piece is connected to the pull rod. A ½-T CT or dog-bone tensile specimen can be mounted between the clevises. The specimen and clevises are kept electrically insulated from the load train by using oxidized Zircaloy pins and mica washers to connect the clevises to the rest of the load train. The crack length is monitored by the same method as for the previous two facilities. Water is circulated through a port in the autoclave body, which serves both as inlet and outlet. A schematic diagram of the recirculating water system is shown in Fig. 9.

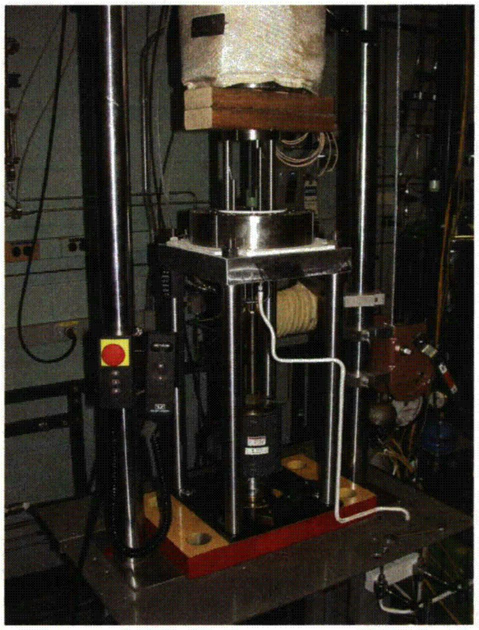

Figure 8.
Photograph of the specimen load train for the 2-liter autoclave.

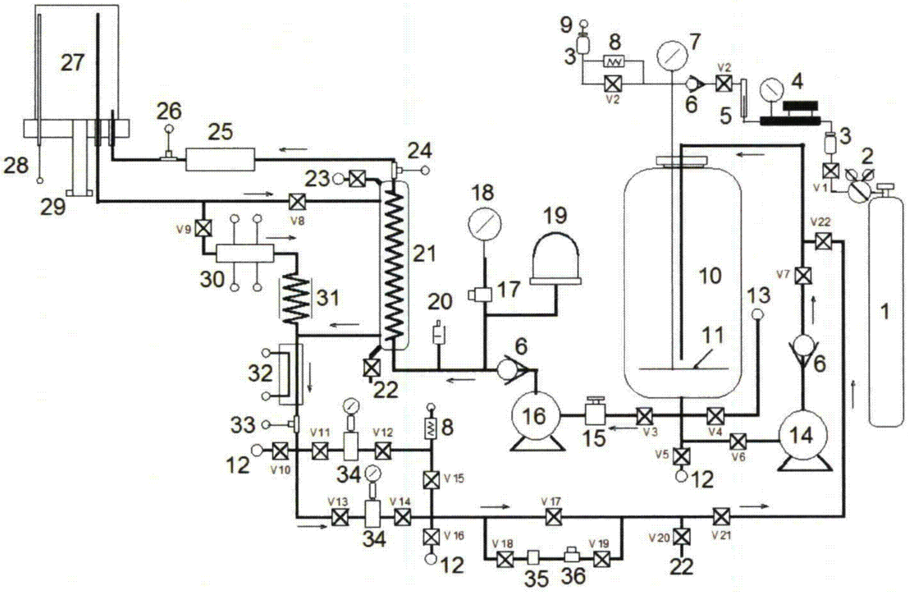

Figure 9. Schematic diagram of the recirculating 2-liter autoclave system.

1. COVER GASS SUPPLY TANK
2. TWO-STAGE HIGH-PRESSURE REGULATOR
3. FLASH ARRESTOR
4. LOW-PRESSURE REGULATOR
5. FLOW METER
6. CHECK VALVE
7. COMPOUND VACUUM & PRESSURE GAUGE
8. PRESSURE RELIEF VALVE
9. VENT TO AIR & FLASH ARRESTOR
10. FEEDWATER STORAGE TANK
11. SPARGE TUBE
12. WATER SAMPLE PORT
13. FEEDWATER FILL PORT
14. FEEDWATER TANK RECIRCULATION PUMP
15. SOLENOID VALVE
16. HIGH-PRESSURE PUMP
17. PRESSURE TRANSDUCER
18. HIGH-PRESSURE GAUGE
19. ACCUMULATOR
20. RUPTURE DISC
21. HEAT EXCHANGER (HX)
22. DRAIN
23. SYSTEM BLEED PORT
24. HEAT EXCHANGER OUTLET TC
25. AUTOCLAVE PREHEATER
26. PREHEATER OUTLET TC
27. COMMERCIAL AUTOCLAVE
28. THERMOWELL
29. "BAL SEAL" RETAINER
30. ECP CELL
31. AIR-COOLED COIL
32. WATER COOLED HEAT EXCHANGER
33. BACK-PRESSURE REGULATOR (BPR) INLET TC
34. BPR
35. PH METER
36. CONDUCTIVITY METER

Figure 9. (cont.)

2.3.3 Primary Water Environment

The simulated PWR feedwater contains 2 ppm Li as LiOH, 1000 ppm B as HBO_3, ≈2 ppm dissolved hydrogen (≈23 cm^3/kg), and less than 10 ppb dissolved oxygen (DO).[12] It is prepared from the laboratory supply of deionized water by first passing this water through a local filtration system that includes a carbon filter, an Organex-Q filter, two ion exchangers, and a 0.2-mm capsule filter. The DO in the deionized water is reduced to <10 ppb by bubbling/sparging pure H_2 through the water. To speed deoxygenation of a fresh tank of water, a vacuum may be applied to the feedwater tank at the vent port. The PWR water is prepared by dissolving boric acid and lithium hydroxide in 20 L of deionized water before adding the solution to the supply tank. The dissolved hydrogen in the water is calculated from the hydrogen pressure and temperature of the supply tank.

Water samples are taken periodically to measure pH, resistivity, and DO concentration both upstream and downstream from the autoclave. An Orbisphere meter and CHEMetrics™ ampoules are used to measure the DO concentrations in the supply and effluent water. The redox and open-circuit corrosion potentials are monitored at the autoclave outlet by measuring the ECPs of platinum and an Alloy 600 electrode, respectively, against a 0.1 M KCl/AgCl/Ag external (cold) reference electrode. The measured ECPs, $E_{(meas)}$ (mV), were converted to the standard hydrogen electrode (SHE) scale, $E_{(SHE)}$ (mV), by the polynomial expression[13]

$$E_{(meas)} + 286.637 - 1.0032 \cdot (\Delta T) + 1.7447 \times 10^{-4} \cdot (\Delta T)^2 - 3.03004 \times 10^{-6} \cdot (\Delta T)^3, \qquad (1)$$

where ΔT(°C) is the temperature difference of the salt bridge in a 0.1 M KCl/AgCl/Ag external reference electrode (i.e., the test temperature minus ambient temperature).

The effect of the proximity of the corrosion potential for the SCC test to the potential at the Ni/NiO phase transition on crack growth rates is well established.[14-16] While the mechanistic origin is unclear, there are consistent data showing that CGRs of Ni-base alloys peak near the Ni/NiO phase boundary.[14-16] Thus, to isolate the effect of temperature, the tests are conducted so that the difference between the corrosion potential of the specimen and that of the Ni/NiO phase transition was maintained approximately constant. The Ni/NiO phase transition is very close to the H_2/H_2O phase transition, and the latter controls the corrosion potential of the simulated primary water environment. As such, the corrosion potential difference reduces to the difference of two hydrogen electrodes:[16]

$$\Delta E = E_{test} - E_{Ni/NiO} = -\frac{RT}{2F}\ln\left(\frac{[H_2]_{test}}{[H_2]_{Ni/NiO}}\right), \tag{2}$$

where: E_{test} = potential at test temperature T,
$E_{Ni/NiO}$ = potential of the Ni/NiO transition at test temperature T,
R = universal gas constant
= 8.314×10^{-3} kJ/mol K (1.103×10^{-3} kcal/mol°R),
F = Faraday constant
= 96485 C/mol,
$[H_2]_{test}$ = hydrogen concentration at test conditions, and
$[H_2]_{Ni/NiO}$ = hydrogen concentration at the Ni/NiO transition.

For two tests, conducted at temperatures T_1 and T_2 and satisfying the constant corrosion potential difference to the Ni/NiO line, Eq. 2 transforms into the following relationship between hydrogen concentrations and test temperatures:

$$\frac{RT_2}{2F}\ln\left(\frac{[H_2]_{test2}}{[H_2]_{Ni/NiO-test2}}\right) = \frac{RT_1}{2F}\ln\left(\frac{[H_2]_{test1}}{[H_2]_{Ni/NiO-test1}}\right), \tag{3}$$

where: $[H_2]_{test2}$ = hydrogen concentration at test temperature T_2,
$[H_2]_{test1}$ = hydrogen concentration at test temperature T_1,
$[H_2]_{Ni/NiO-test2}$ = hydrogen concentration at Ni/NiO transition for test 2, and
$[H_2]_{Ni/NiO-test1}$ = hydrogen concentration at Ni/NiO transition for test 1.

The hydrogen concentration at the Ni/NiO transition as a function of temperature was determined by fitting Attanasio et al.[15] data with a fourth-order polynomial (Fig. 10). The best fit is given by the following expression:

$$[H_2]_{Ni/NiO}\,(T) = -8783.1+53.803\cdot T-0.11961\cdot T^2+0.00011238\cdot T^3-3.628899\times 10^{-8}\cdot T^4 \tag{4}$$

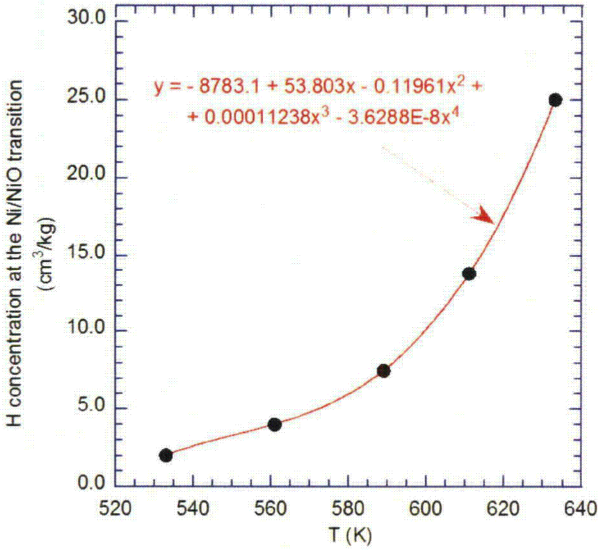

Figure 10.
Hydrogen concentration at Ni/NiO phase transition as a function of temperature (data taken from Ref. 15).

Equation 3 can be solved for the hydrogen concentration at test temperature T_2. This concentration maintains the potential difference to the Ni/NiO line similar to that of a test conducted at temperature T_1. For the purpose of this calculation, test conditions "1" are considered those typical of tests conducted in a PWR environment at 320°C (608°F, 593 K), with $[H_2]_{test1}$ = 23 cm^3/kg.[12] The results for several temperatures of interest are shown in Table 6. For each temperature, the hydrogen concentration at the Ni/NiO transition was calculated by Eq. 4, then the concentration needed to maintain the corrosion potential difference constant was calculated by Eq. 3.

Table 6. Test conditions for various temperatures and hydrogen concentrations.

Test Temperature		$[H_2]_{Ni/NiO}$, cm^3/kg	$[H_2]_{test}$, cm^3/kg	ΔE, mV
°C (°F)	K			
290 (554)	563	3.0	11.01	31.5
300 (572)	573	3.9	13.81	31.3
305 (581)	578	4.5	15.60	31.1
310 (590)	583	5.2	17.71	30.8
320 (608)	593	7.1	23.00	30.1
350 (662)	623	17.8	47.59	26.4

2.4 Test Procedure

The CGR tests are conducted in the load-control mode using a triangular, sawtooth, or trapezoidal waveform with load ratio R of 0.3-0.7. The CT specimens are fatigue precracked with a triangular waveform in the test environment at load ratio $R = 0.3$, frequency ≈ 1 Hz, and maximum stress intensity factor (K_{max}) of 20-25 $MPa \cdot m^{1/2}$ (18-23 $ksi \cdot in^{1/2}$). After ≈ 0.5 -mm (20 mils) extension, R is increased incrementally to 0.5-0.7, and the loading waveform was changed to a slow/fast sawtooth with rise times of 30-1000 s and unload time of 12 s. This loading sequence is considered to result in reproducible CGRs.[17] For sawtooth loading, the CGRs are calculated on the basis of the rise time. During individual test periods, K_{max} was maintained approximately constant by periodic load shedding (less than 2% decrease in load at any given time).

Crack extensions are monitored by the reversing-DC potential difference method. The current leads are attached to the holes on the top and bottom surfaces of the specimen (Fig. 5), and potential leads are either welded on the front face of the specimen across the machined notch but on diagonal ends (1-TCT specimens, Fig. 5a) or attached to pre-machined taps (½-T CT specimens, Fig. 5b). Also, to compensate for the effects of changes in resistivity of the material with time, an internal reference bar of the same material being tested is installed near the test specimen. The CT specimen and reference bar are connected in series, and the DC potential across the specimen as well as the reference bar is monitored continuously during the test. The results for the reference bar are used to normalize potential drop measurements for the CT test specimen.

During crack growth tests in high-temperature water, environmental enhancement of CGRs does not occur from the start of the test. Under more rapid cyclic loading typically applied during precracking and initial periods of cyclic loading the crack growth is dominated by mechanical fatigue. In general, environmental enhancement is typically observed under loading conditions that would lead to CGRs between 10^{-11} and 10^{-9} m/s in air.

The stress intensity factor range (ΔK) was calculated in accordance with ASTM E 1681[11] and E 647[10] as follows:

$$\Delta K = \frac{\Delta P}{(BB_N W)^{1/2}} \frac{\left(2 + \frac{a}{W}\right)}{\left(1 - \frac{a}{W}\right)^{3/2}} f\left(\frac{a}{W}\right), \tag{5}$$

$$\Delta P = P_{max} - P_{min} \qquad \text{for } R > 0, \tag{6}$$

$$f\left(\frac{a}{W}\right) = 0.886 + 4.64\left(\frac{a}{W}\right) - 13.32\left(\frac{a}{W}\right)^2 + 14.72\left(\frac{a}{W}\right)^3 - 5.6\left(\frac{a}{W}\right)^4, \tag{7}$$

where P_{max} and P_{min} are maximum and minimum applied load, a is crack length, W is the specimen width, and the effective thickness $B_{eff} = (B\ B_N)^{0.5}$. The applied K and crack size limits for the tests met the ASTM E 1681 and E 647 criteria. These criteria are intended to ensure applicability and transferability of the cracking behavior of a component or specimen of a given thickness under a specific loading condition to a crack associated with a different geometry, thickness, and loading condition. The

K/size criteria require that the plastic zone at the tip of a crack be small relative to the specimen geometry. For constant load tests, ASTM E 1681[11] requires that

$$B_{eff} \text{ and } (W - a) \geq 2.5\ (K/\sigma_{ys})^2, \tag{8}$$

and for cyclic loading, ASTM 647[10] requires that

$$(W - a) \geq (4/\pi)\ (K/\sigma_{ys})^2, \tag{9}$$

where K is the applied stress intensity factor, and σ_{ys} is the yield stress of the material. In high-temperature water, in circumstances where environmental enhancement occurs, and corrosion fatigue and SCC overtake mechanical fatigue as the primary mechanism for crack growth, Eq. 8 is probably the more appropriate criterion. For high-strain hardening materials (i.e., ultimate-to-yield stress ratio $\sigma_{ult}/\sigma_{ys} \geq 1.3$), both criteria allow the use of the flow stress defined as $\sigma_f = (\sigma_{ult} + \sigma_{ys})/2$ rather than the yield stress. Table 7 provides the maximum allowable stress intensity factors meeting the criteria set by Eqs. 8 and 9 for cyclic and constant load testing of Alloy 690 and 152 in the as-received and the as-welded condition, respectively. Flow stresses used for the calculations are 402 MPa (58 ksi) for Alloy 690 and 474 MPa (68.7 ksi) for Alloy 152 weld (detailed tensile property data are presented in Section 4.1 of this report). Both ½-T CT and 1-T CT specimens (Fig. 5) are considered. In addition, typical total crack extensions of 1.5 mm (0.06 in.) for a ½-T CT and 10 mm (0.4 in.) for a 1-T CT are assumed. As such, the table shows that in a case of a test involving a ½-T CT specimen of Alloy 690 in the as-received condition, a stress intensity factor as high as 39 MPa·m$^{1/2}$ (35.5 ksi·in.$^{1/2}$) can be employed to fatigue precrack the specimen at the beginning of the test. At the end of the test, after an assumed total crack advance of 1.5 mm (0.06 in.), constant load with a stress intensity factor not exceeding 26 MPa m$^{1/2}$ (24 ksi·in.$^{1/2}$) may be used. The table also shows that 1-T CT specimens are more versatile in both crack advance and sampling of microstructure, as well as the range of stress intensity factors that may be used. However, such specimens are not always possible due to the physical size of the material available.

Table 7. Maximum allowable stress intensity factors for cyclic and constant load testing of Alloys 690 and 152 weld in ½-T CT and 1-T CT specimen configurations.

Alloy 690

Specimen type	a, mm (in.)	K_{cyclic}, MPa·m$^{1/2}$ (ksi·in.$^{1/2}$)	K_{SCC}, MPa·m$^{1/2}$ (ksi·in.$^{1/2}$)
½-T CT	12 (0.47)	39.1 (35.6)	27.9 (25.4)
	13.5 (0.53)	36.6 (33.3)	26.1 (23.8)
1-T CT	12.7 (0.50)	69.6 (63.3)	49.6 (45.1)
	22.7 (0.89)	59.8 (54.4)	42.6 (38.8)

Alloy 152

Specimen type	a, mm (in.)	K_{cyclic}, MPa·m$^{1/2}$ (ksi·in.$^{1/2}$)	K_{SCC}, MPa·m$^{1/2}$ (ksi·in.$^{1/2}$)
½-T CT	12 (0.47)	39.1 (35.6)	27.9 (25.4)
	13.5 (0.53)	36.6 (33.3)	26.1 (23.8)
1-T CT	12.7 (0.50)	69.6 (33.3)	49.6 (23.8)
	22.7 (0.89)	59.8 (54.4)	42.6 (38.8)

After each test is completed, the specimen is fractured in liquid nitrogen, and the fracture surfaces are examined by optical and electron microscopy to measure the final crack length using the 9/8 averaging technique; that is, the two near-surface measurements are averaged, and the resultant value is averaged with the remaining seven measurements.

2.5 Analysis of Crack Growth Rate Data

The experimental approach relies on monitoring the cyclic rates for environmental enhancement. As such, only those conditions that show environmental enhancement are chosen for transitioning from TG fatigue to IG SCC. Under cyclic loading, the CGR (m/s) can be expressed as the superposition of the rate in air (i.e., mechanical fatigue) and the rates due to corrosion fatigue and SCC ($\dot{a}_{CF}$ and $\dot{a}_{SCC}$, respectively), given as[2,4]

$$\dot{a}_{env} = \dot{a}_{air} + \dot{a}_{CF} + \dot{a}_{SCC}. \tag{10}$$

The cyclic CGRs for Ni alloys and welds in air were determined from correlations developed earlier at ANL: [2,4,7,9]

$$\dot{a}_{air} = \left(\frac{da}{dN}\right)/t_r = \left[C\cdot(1-0.82\cdot R)^{-2.2}\cdot(\Delta K)^{4.1}\right]/t_r, \tag{11}$$

where da/dN is the growth rate per cycle, t_r is the rise time for the loading cycle, R is the load ratio (i.e., ratio of the minimum and maximum stress intensity factors K_{min}/K_{max}), ΔK is K_{max} - K_{min} in MPa·m$^{1/2}$, and the constant C depends on the material and temperature. For Alloy 600 the constant (C_{A600}) is a third-order polynomial with respect to temperature T (°C), [2,4]

$$C_{A600} = 4.835\times10^{-14} - (1.622\times10^{-17})T + (1.490\times10^{-18})T^2 - (4.355\times10^{-21})T^3 . \tag{12}$$

In LWR coolant environments, the CGRs of Alloy 600 show frequency-dependent enhancement under cyclic loading conditions. In high-DO water [i.e., normal water chemistry in boiling water reactor (BWR)], the environmental enhancement of the growth rates does not appear to depend on the material composition (e.g., C content) or material heat treatment. In contrast, environmental enhancement of CGRs of Alloy 600 in low-DO water does seem to be strongly dependent on material conditions. In the literature,[18-22] such variability has been attributed to thermomechanically controlled parameters, such as yield strength and grain boundary coverage of carbides, although the evidence for this dependence is more substantial for steam generator tubing than for structural components.

For Alloy 690, the constant C_{A690} is given by a third-order polynomial of temperature T (°C), expressed as:[2]

$$C_{A690} = 5.423\times10^{-14} + (1.83\times10^{-16})T - (1.725\times10^{-18})T^2 + (5.490\times10^{-21})T^3. \tag{13}$$

For Ni-alloy welds, the constant C_{Niweld} is given by a fourth-order polynomial with respect to temperature T (°C), expressed as:[9]

$$\begin{aligned} C_{Ni\text{-}weld} = {} & 8.659\times10^{-14} - (5.272\times10^{-17})T + (2.129\times10^{-18})T^2 \\ & - (1.965\times10^{-20})T^3 + (6.038\times10^{-23})T^4 \end{aligned} \tag{14}$$

In earlier ANL work, correlations were developed to estimate the enhancement of cyclic CGRs in LWR environments relative to the CGRs in air under the same loading conditions. In the absence of any significant contribution of SCC to growth rate, the cyclic CGRs for Alloy 600, either in the solution annealed (SA) condition or the SA plus thermally treated (TT) condition, in ≈300 ppb DO water at 289°C are given by the expression[4]

$$\dot{a}_{\mathrm{env,A600}} = \dot{a}_{\mathrm{air,A600}} + 4.4\times10^{-7}\cdot\left(\dot{a}_{\mathrm{air,A600}}\right)^{0.33}. \tag{15}$$

In low-DO environments (e.g., hydrogen water chemistry for the BWR or PWR environment) at 320°C (608°F), some alloys show little enhancement, while others show enhancement comparable to that predicted by Eq. 15.

Similarly, correlations describing the cyclic CGRs of Ni-alloy welds (e.g., Alloys 182 and 82) have been developed.[9] Under similar loading conditions, the CGRs of Ni-alloy welds are a factor of 2-3 higher than those of Alloy 600. The analysis[9] indicated that the cyclic CGRs of Ni-alloy welds in PWR water are represented by the expression

$$\dot{a}_{\mathrm{env,Ni-weld}} = \dot{a}_{\mathrm{air,Ni-weld}} + 0.018\cdot\left(\dot{a}_{\mathrm{air,Ni-weld}}\right)^{0.78}. \tag{16}$$

Figure 11 summarizes the expected behaviors for cyclic rates in air and environment for Alloys 600, 690 and Ni-base welds as described by Eqs. 11-16. All data is plotted as a function of the predicted behavior for Alloy 600 in air.

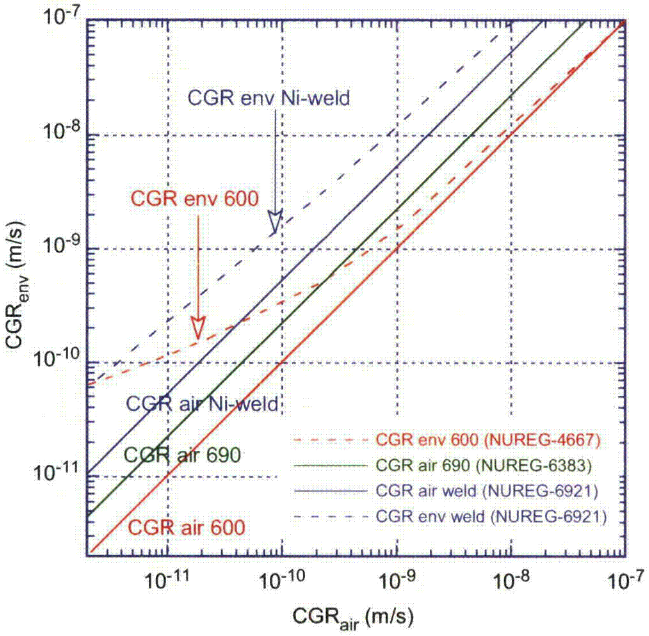

Figure 11.
Crack growth rates in air and environment for Alloys 600, 690 and Ni-base welds as a function of predicted rates in air for Alloy 600 (data taken from Refs. 4,7,9).

The SCC growth rate data for Alloy 600 and its weld metals have been reviewed by White and Hickling (MRP-55[23] and MRP-115[24]) to determine the effects of critical parameters such as stress intensity factor, temperature, material heat treatment, cold work, and water chemistry on growth rates. For Alloy 600, the CGR (m/s) under SCC conditions is represented by the expression,[23]

$$\dot{a}_{A600} = \alpha \exp\left[-\frac{Q}{R}\left(\frac{1}{T}-\frac{1}{T_{ref}}\right)\right](K-K_{th})^{\beta}, \tag{17}$$

where: Q = activation energy for crack growth
= 130 kJ/mol (31.1 kcal/mol) for Alloy 600,
R = universal gas constant
= 8.314×10^{-3} kJ/mol K (1.103×10^{-3} kcal/mol·°R),
T = absolute operating temperature in K (or °R),
T_{ref} = absolute reference temperature used to normalize the CGR data
= 598 K (1076.67°R),
α = crack growth amplitude (2.67×10^{-12} at 325°C),
K = crack tip stress intensity factor (MPa·$m^{1/2}$),
K_{th} = crack tip stress intensity factor threshold (9 MPa·$m^{1/2}$, 8.2 ksi·$in.^{1/2}$) and
β = exponent 1.16.

The effect of K on the SCC growth rate for Ni-alloy welds in PWR environments has been represented by a modified[24] version of the above relationship. Unlike the CGR relationship for Alloy 600, the relationship for Ni-alloy welds has no threshold value for the stress intensity factor K,

$$\dot{a}_{Ni-weld} = \alpha \exp\left[-\frac{Q}{R}\left(\frac{1}{T}-\frac{1}{T_{ref}}\right)\right]K^{\beta}, \tag{18}$$

where Q, R, T, and T_{ref} are the same as in Eq. 17; the crack growth amplitude α is 1.5×10^{-12} at 325°C; and exponent β is 1.6. Also, unlike Alloy 600, for which a reliable value for the activation energy for crack growth was determined, no such number is available for the Ni-weld alloys. Thus, for Ni-weld alloys, the activation energy is assumed to be the same as that for Alloy 600.

3 Microstructural Characterization

The alloys used in the present project were subjected to an extensive metallographic analysis. This section presents the findings for Alloy 690 in plate form and from CRDM nozzle tubing and the laboratory-prepared Alloy 152 weld. The characterization was focused on features known to affect the IG SCC behavior. As such, special attention was paid to grain boundary carbides and grain boundary character distribution. Grain boundary carbides have a profound impact on the SCC behavior of Alloy 600, affecting both crack initiation and propagation. Several early studies reported correlations between high grain boundary carbide coverage and increased cracking resistance,[25-26] and subsequent work has isolated and established the beneficial effect of carbides on SCC behavior.[27-28] Likewise, grain boundary character distribution has been shown to affect crack initiation in several austenitic alloys in high temperature water environments.[29-36] As such, grain boundaries in special orientation relationships have been found to be more resistant to SCC initiation than random boundaries.[30-31] Moreover, SCC was found to propagate preferentially along random boundaries in Alloys X-750[35] and 182 weld.[8]

3.1 Alloy 690 in Plate Form (A690WC)

The metallographic analysis of Alloy 690 was focused on the 26% cold-rolled condition – as this was the form in which this alloy was tested. The analysis included measurements of hardness along the sample thickness, as well as SEM/OIM and TEM analyses, and focused on the grain boundary carbides and, more recently, on the existence of banding in this alloy.

3.1.1 Hardness Testing

The cold-work distribution along the thickness in the 26% cold-rolled plate was evaluated by measuring the microhardness at three positions (a, b, and c, as shown in Fig. 12a).

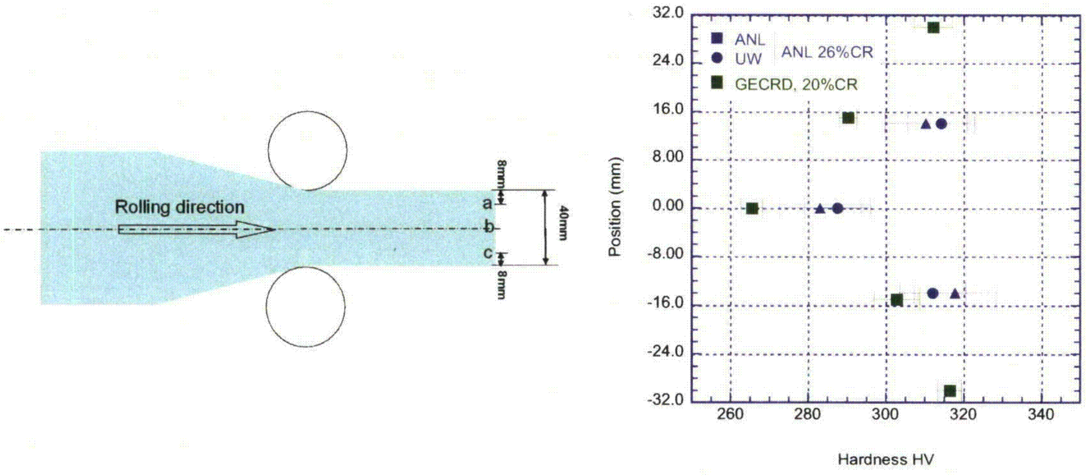

(a) (b)

Figure 12. **(a) Schematic of the rolling process of the ANL plate identifying the locations (a, b, and c) at which hardness was evaluated, and (b) hardness along thickness of the Alloy 690 plate cold-rolled by 26% (ANL). Similar data from a plate cold-rolled by 20% at GE are included for comparison.**

The hardness measurements were performed by Vickers indentation with a load of 1 kg-f and load time of 15 s at the three positions. The results from two sets of measurements (by ANL and University of Wisconsin) are shown in Fig. 12b. For comparison, the results obtained on a different plate (heat B25K) cold-rolled by 20% at GE to a final thickness of 67 mm (2.6 in.) are also included. The data show the same general trend: the mid-plane has a 10-12% lower hardness compared with that for the positions that are closer to the rolling surfaces. Also, because the GE plate was initially thicker and cold-rolled by 20% (vs. 26% for the ANL plate), it had a lower hardness at the mid-plane.

3.1.2 General Microstructure – Grain Boundary Carbides

The microstructure of the Alloy 690 plate that was cold-rolled by 26% was examined by SEM and TEM. Figure 13 shows that the microstructure of the mid-plane has grain boundary carbides and matrix TiN precipitates. Surprisingly, the grains do not appear elongated in these pictures. Figure 14 shows TEM images from specimens prepared from the mid-plane of the plate. Figures 14a and 14b show a highly deformed microstructure, as expected for cold-worked material. Figures 14c and 14d also show several grain boundary carbides, as indicated by the white arrows. Other than the absence of elongated grains, the microstructure of this material did not appear to be unusual.

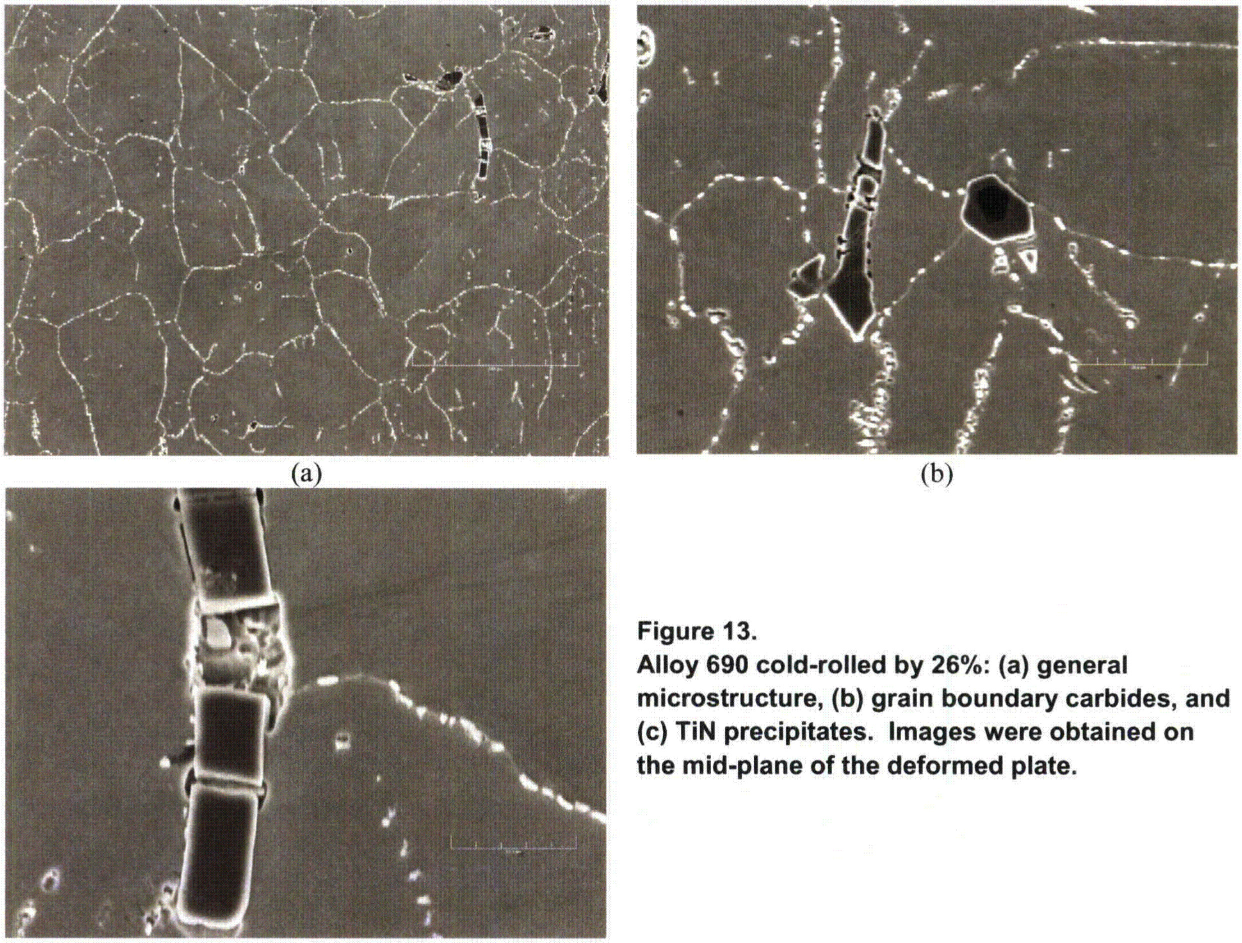
(a)

(b)

(c)

Figure 13.
Alloy 690 cold-rolled by 26%: (a) general microstructure, (b) grain boundary carbides, and (c) TiN precipitates. Images were obtained on the mid-plane of the deformed plate.

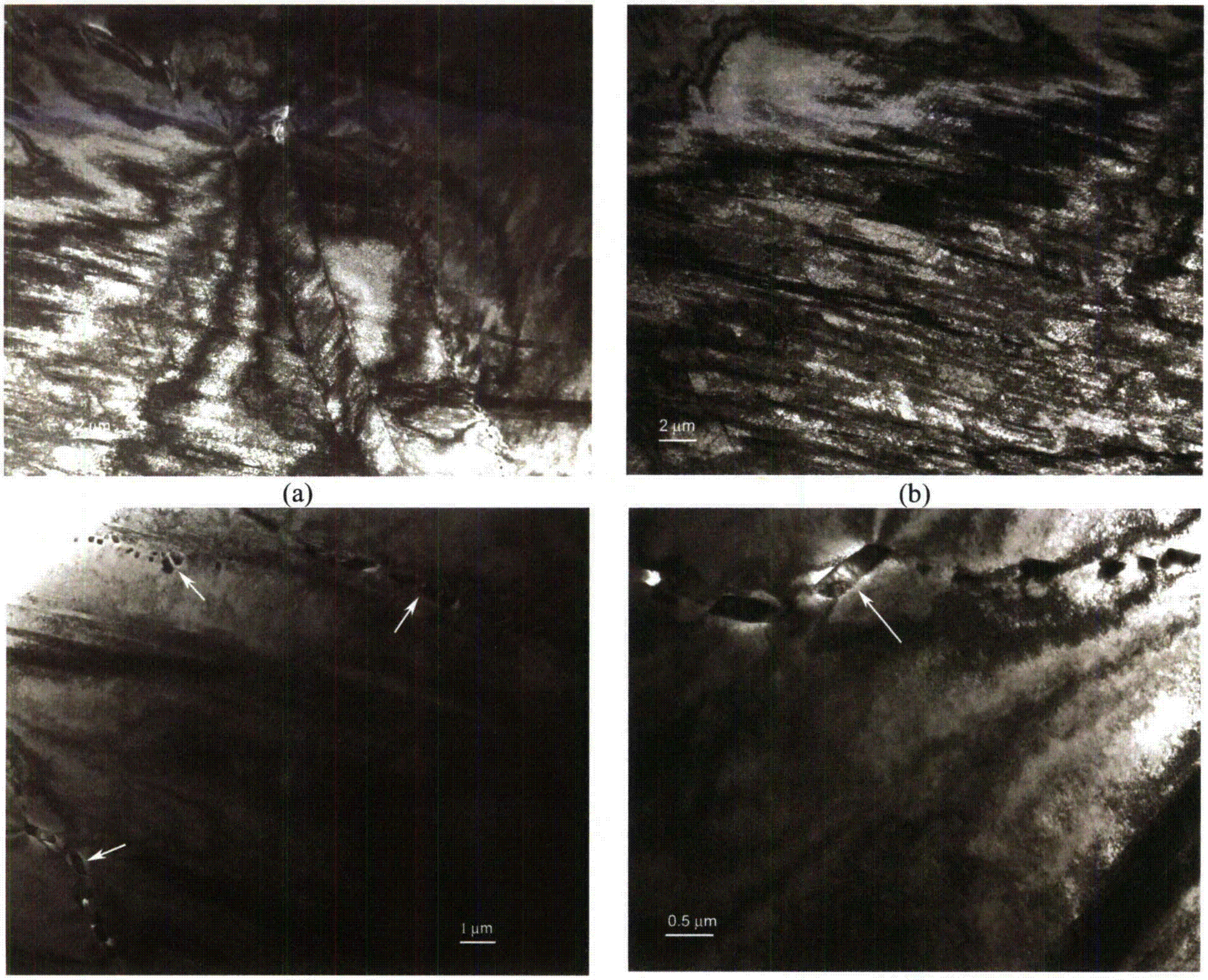

(a) (b)

(c) (d)

Figure 14. **TEM micrographs from mid (rolling plane) Alloy 690 deformed by 26% showing the following: (a,b) high deformation microstructure and (c,d) grain boundary carbides.**

A second round of TEM examinations was prompted by the finding that the fracture surfaces of alloys tested at both ANL and Bettis Atomic Power Laboratory (Bettis)[37] appeared to contain cracked grain boundary carbides. Figure 15 shows images of carbides obtained from the mid-plane of the cold-rolled plate. Some cracked grain boundary carbides are apparent. Figure 16 shows similar images obtained from the mid-plane of a 20% cold-rolled Alloy 690 plate provided by GE. The carbides appear somewhat different in shape (compare Fig. 15a and Fig. 16a); however, cracked grain boundary carbides were also found in this alloy (Fig. 16b).

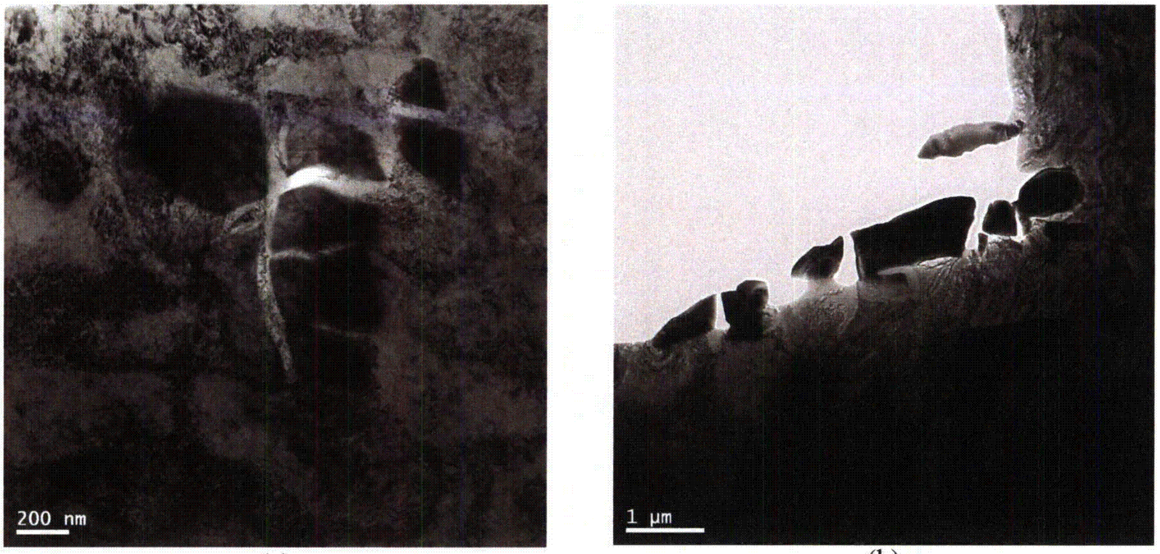

(a) (b)

Figure 15. **Alloy 690 cold-rolled by 26%, which was CGR tested at ANL.**

(a) (b)

Figure 16. **Alloy 690 cold-rolled by 20%, which was provided by GE.**

3.1.3 Grain Boundary Character Distribution

The grain boundary character distribution (GBCD) is essentially a classification of boundaries according to the coincident site lattice model as either coincident site lattice boundaries (CSLBs) or high-angle boundaries (HABs). The CSLBs are formed when the neighboring grains are in specific orientation relationships, and they are described in terms of the fraction $1/\Sigma$ of coincident atomic lattice sites. A boundary that contains a high density of coincident lattice points is expected to have low energy because of a good atomic fit. These boundaries have been shown to possess an increased resistance to IG SCC over HABs.[29-36] The GBCD is obtained by OIM.

Figures 17 and 18 summarize the findings of the OIM analysis for the Alloy 690 in plate form in the as-received and 26% cold-rolled condition. Figure 17a shows a typical OIM map with equiaxed grains. The resulting average grain size is 36 μm (Fig. 17b), and the CSLB fraction is 27.5%, of which a large proportion is twins (Σ=3). The latter result was expected; however, the former indicates a relatively small CSLB fraction for this alloy. The typical fraction for a Ni-base alloy in the as-received solution annealed condition is approximately 50%.[31] Similar results were obtained for the alloy in the 26% cold-rolled condition (Fig. 18). Again, the relatively small proportion of CSLBs should be noted.

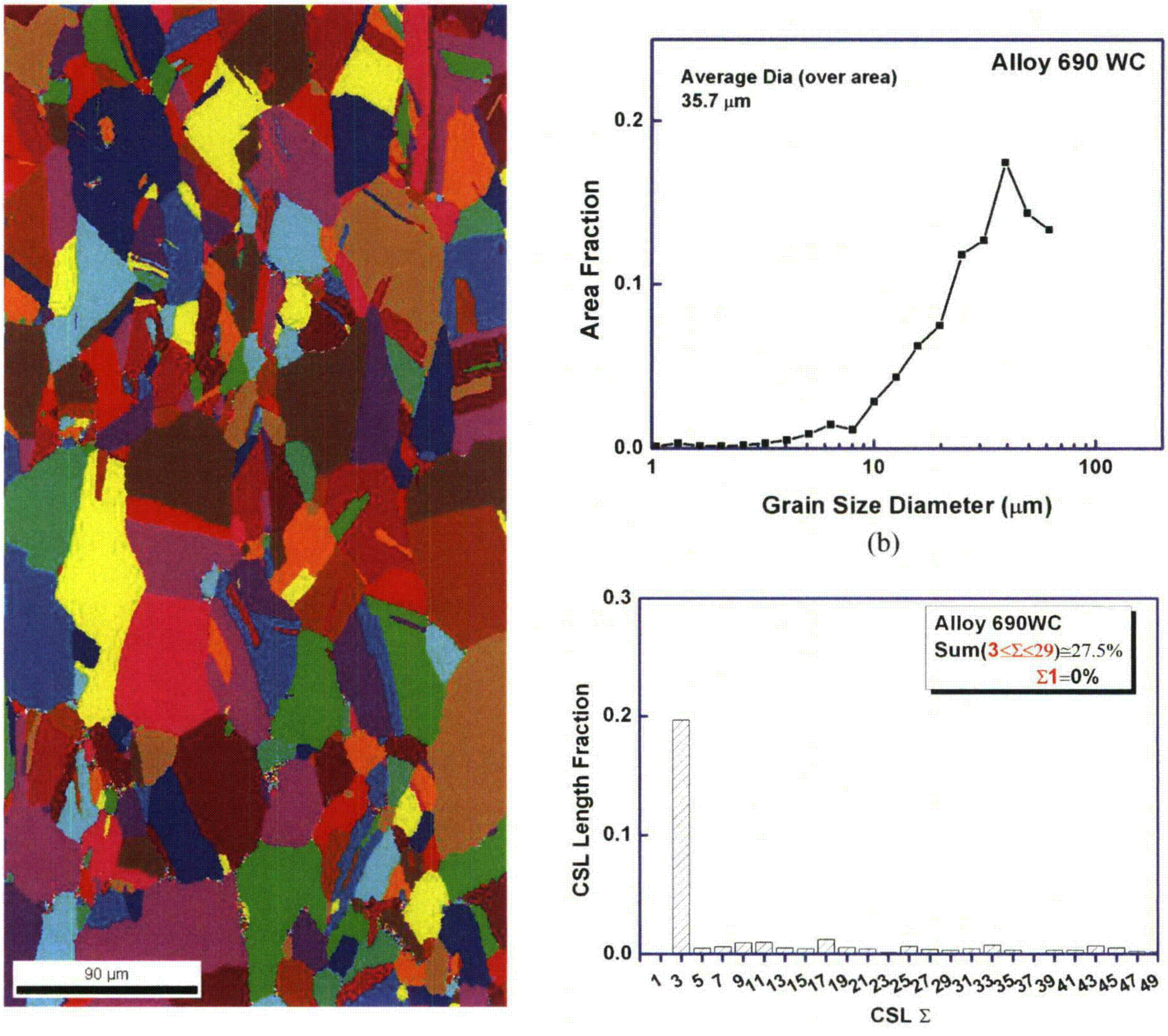

(b)

(a) (c)

Figure 17. **(a) OIM map, (b) graph of grain size distribution, and (c) graph of grain boundary character distribution for Alloy 690 in plate form in the as-received condition.**

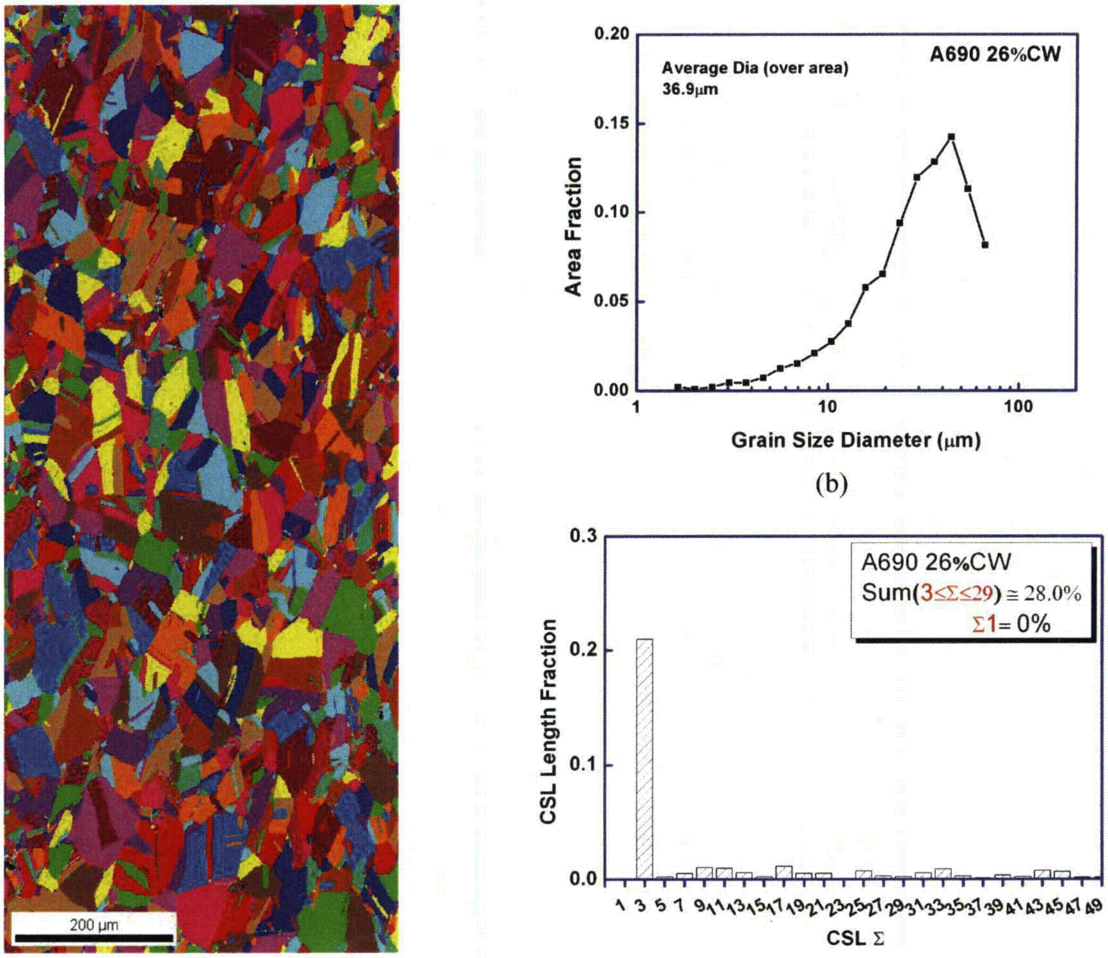

(a) (b) (c)

Figure 18. **(a) OIM map, (b) graph of grain size distribution, and (c) graph of grain boundary character distribution for Alloy 690 in plate form in the 26% cold-rolled condition.**

3.1.4 Carbide and Grain Size Banding

Carbide and grain size banding have been advanced by Andresen et al.[38] as a possible cause for the relatively high CGRs of several heats of Alloy 690 measured in the cold-rolled condition. For this investigation, the Alloy 690 plate at ANL (Heat NX3297HK12) was examined not only in the mid-plane (where the CGR specimens were cut), but also along the thickness. Both the as-received and the 26% cold-rolled conditions were examined. For the examination, specimens #1, 5, 6, and 8 were cut from the as-received Alloy 690 plate (Fig. 19). These specimens were ground to a 1-µm surface finish, electropolished, and etched with Marble's reagent.

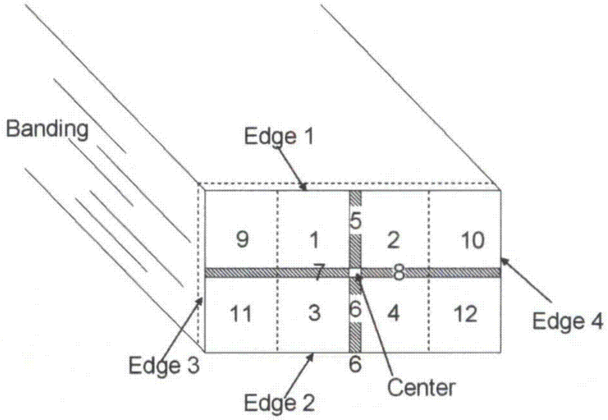

Figure 19.
Schematic showing the positions of the metallography specimens cut from the plate in the as-received condition.

Figure 20 shows the images obtained from specimen #1. This specimen was decorated with short streaks, which were further revealed as areas with thick grain boundary carbides.

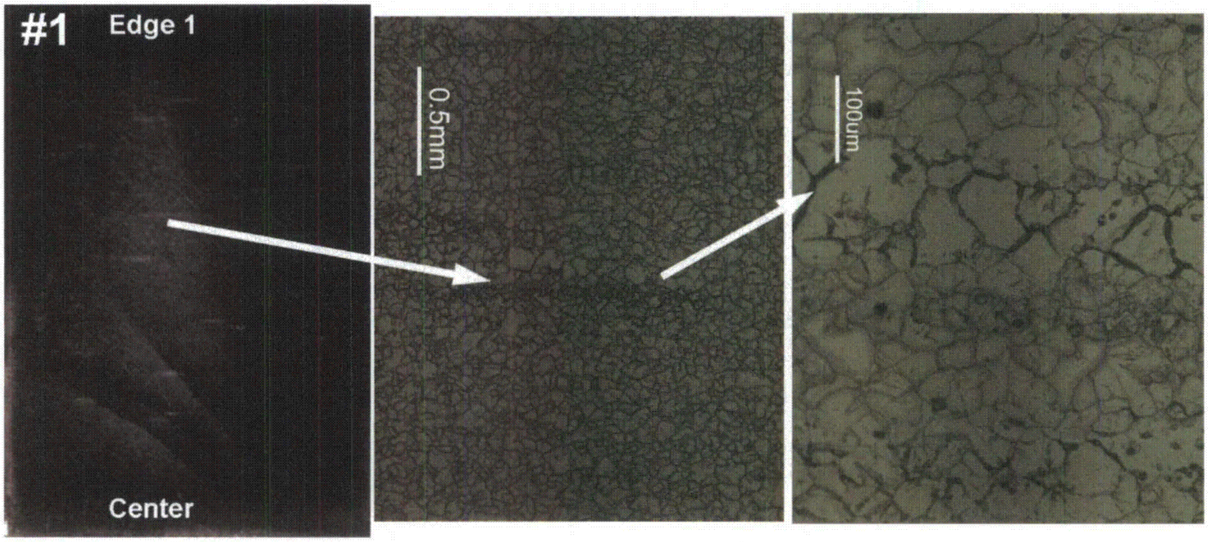

Figure 20. Microstructure of specimen #1 showing carbide streaks.

Grain size banding was found in specimens #5 and #6 close to edges 1 and 2, respectively (Fig. 21). Specimen #8, taken from the middle of the plate, showed neither carbide streaks nor grain size banding (Fig. 22).

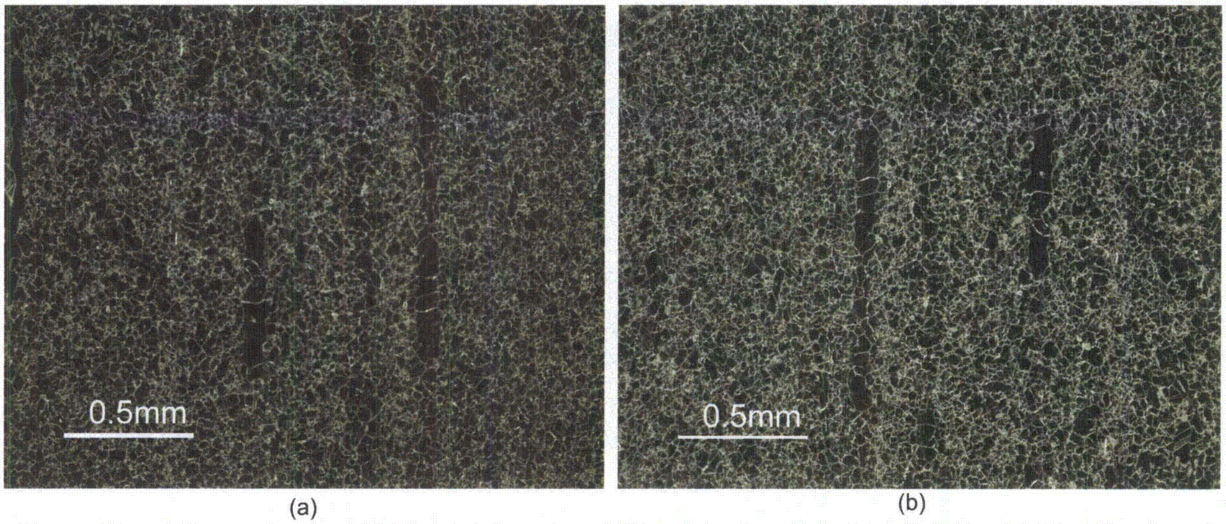

(a) (b)

Figure 21. **Grain size banding in (a) Specimen #5 near edge 1 and (b) Specimen #6 near edge 2 (images rotated by 90°C vs. Fig. 19).**

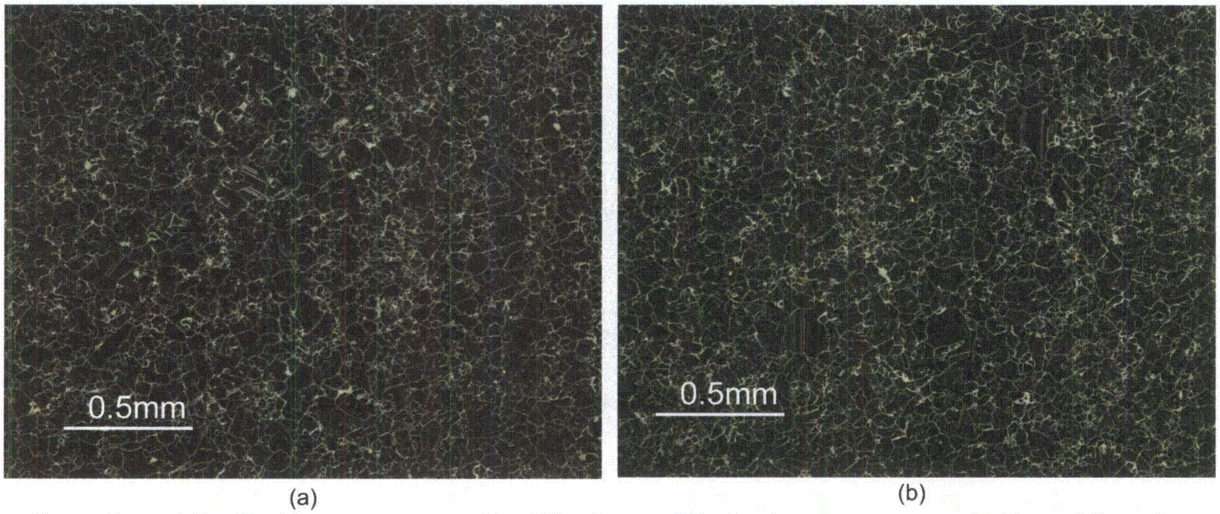

(a) (b)

Figure 22. **Microstructure observed in Specimen #8: (a) near edge 4 and (b) middle of the specimen (images rotated by 90°C vs. Fig. 19).**

The microstructure of Alloy 690 cold-rolled by 26% is shown in Figs. 23 and 24. The areas close to edges 1 and 2 (Fig. 19) are decorated with carbide streaks (Fig. 24), while the center is nearly free from the streaks. In addition, grain size banding was observed near the same edges, as illustrated in Fig. 24.

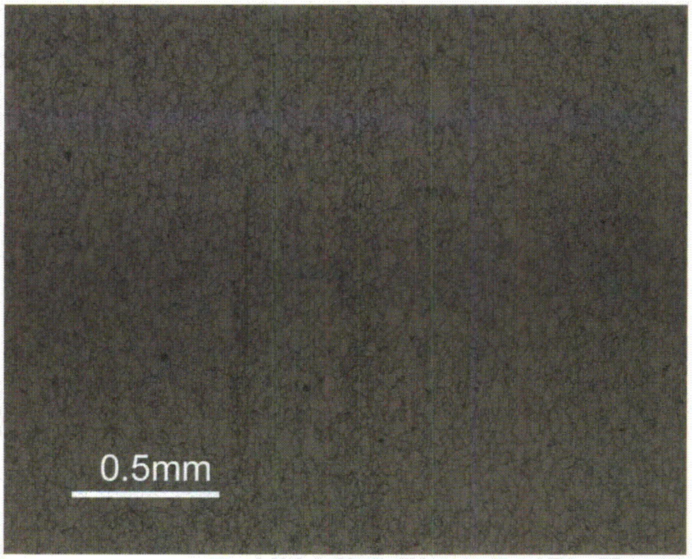

Figure 23.
Carbide streaks in Alloy 690 plate cold-rolled by 26%.

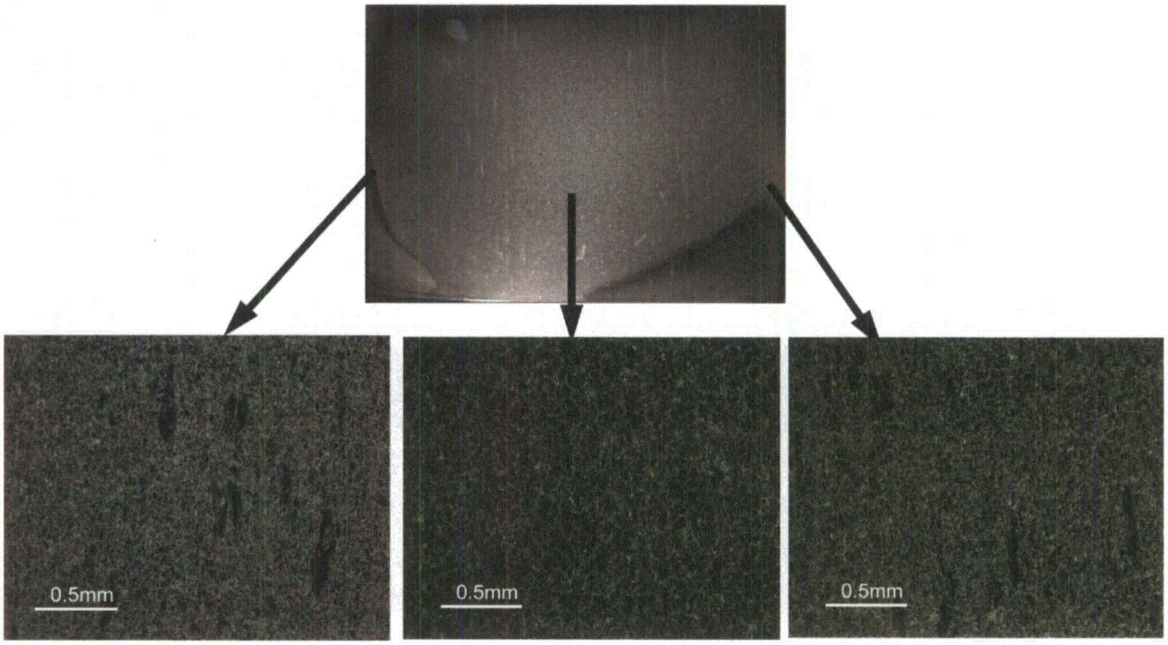

Figure 24. **Grain microstructure in Alloy 690 plate cold-rolled by 26%.**

In summary, carbide streaks and grain size banding occurred near edges 1 and 2 (Fig. 19) of the Alloy 690 plate. The mid-plane appears to be free of carbide streaks and bands. These features were preserved by cold-rolling.

3.2 Alloy 690 TT from CRDM Tubing (C690)

The Alloy 690TT was examined by SEM, TEM, and OIM. The objectives were to observe the microstructure, focusing on grain boundary carbides, and to determine the GBCD. As noted in the previous section, both of these features are known to influence the SCC behavior.

Figure 25 shows an SEM micrograph of the Alloy 690TT microstructure, consisting of equiaxed grains having an average size of 70 µm. Figure 26 shows a TEM image of the microstructure. This alloy has a moderate dislocation density.

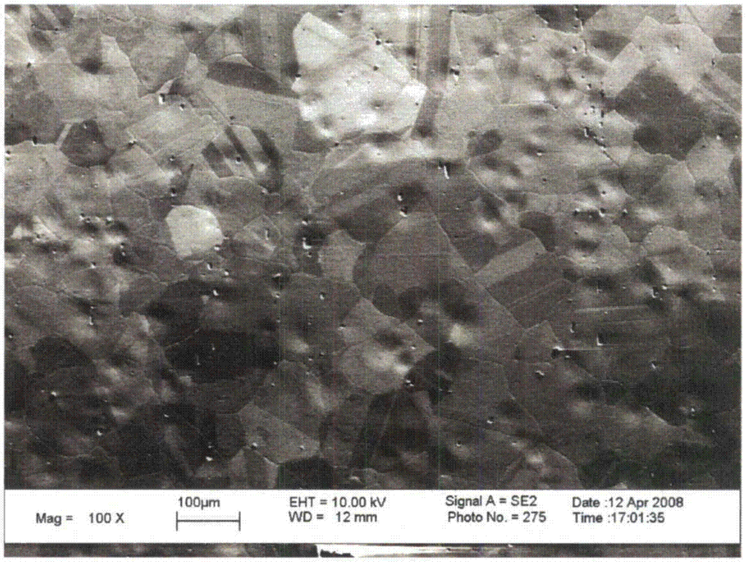

Figure 25.
Microstructure of Alloy 690 TT from CRDM tubing.

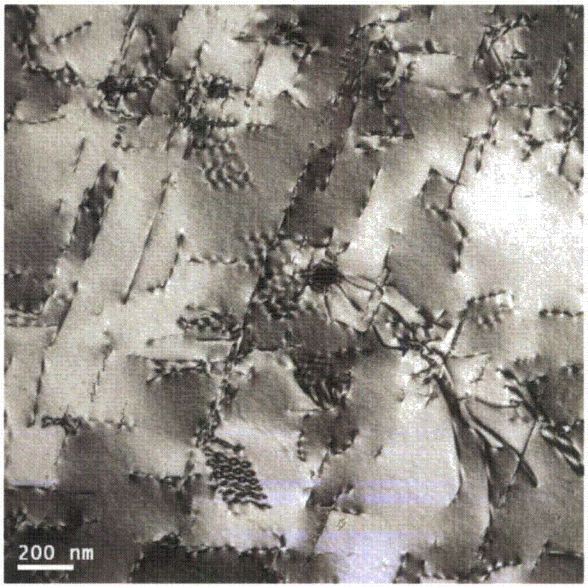

Figure 26.
Microstructure of Alloy 690 TT from CRDM tubing.

Figure 27 shows additional TEM images, with a focus on the grain boundary carbides. The alloy has a dense carbide decoration on the grain boundaries. Hence, it is expected to possess superior SCC resistance.

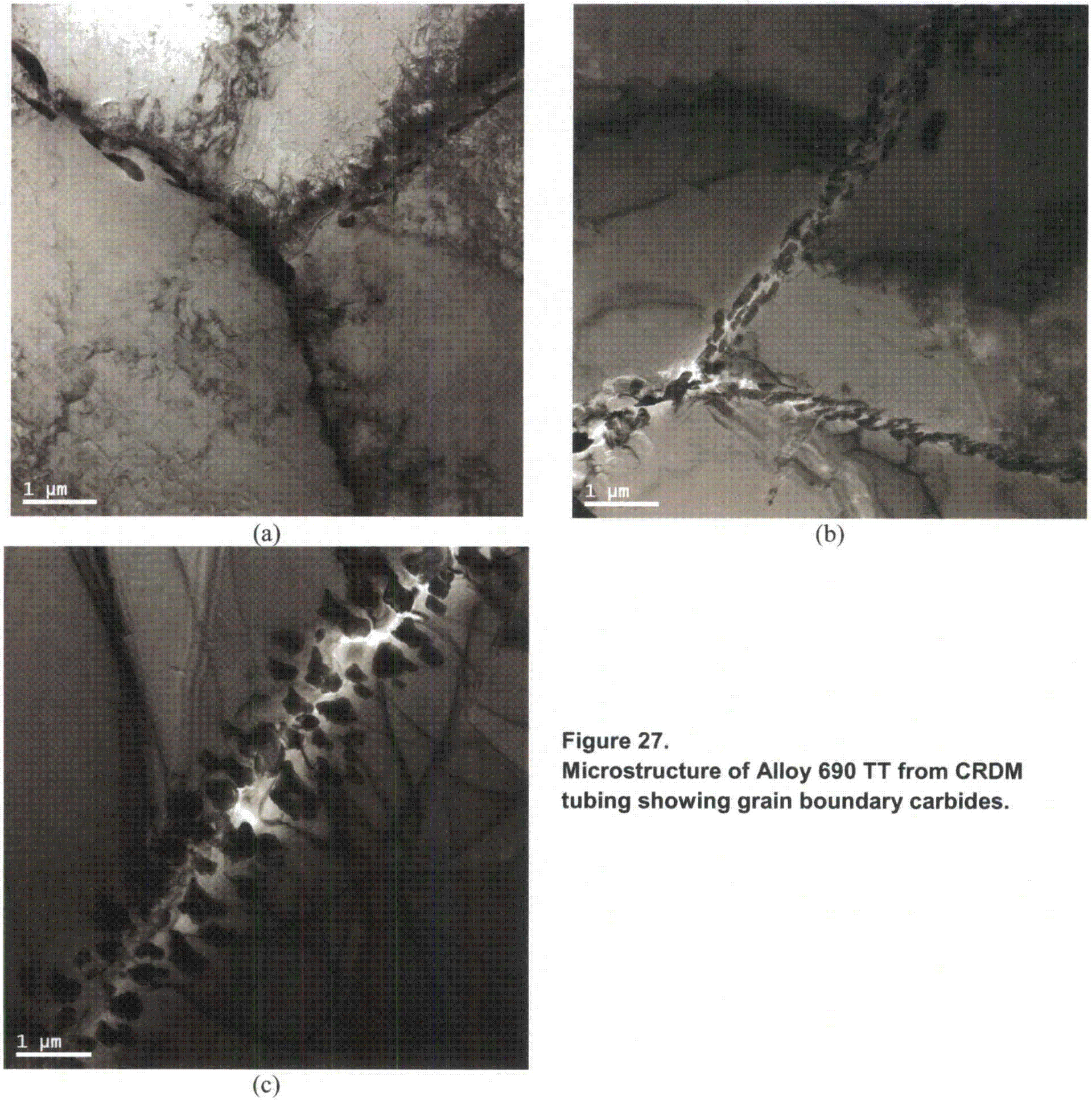

(a)

(b)

(c)

Figure 27.
Microstructure of Alloy 690 TT from CRDM tubing showing grain boundary carbides.

Figure 28 summarizes the findings of the OIM analysis. Figure 28a shows a typical OIM map with equiaxed grains. The resulting average grain size is 73 µm (Fig. 28b), about double the grain size found in the plate alloy (Fig. 17). The CSLB fraction in this material, Fig. 28c, is approximately 53%, of which a large proportion is twins (Σ=3), and 6% is low-angle boundaries. While this GBCD is typical of a Ni-base alloy, [29-32] it should be noted that, again, this fraction is about double that measured for the plate alloy. The significance of this finding is that the plate alloy has 50% more crack-susceptible boundaries than the CRDM alloy.

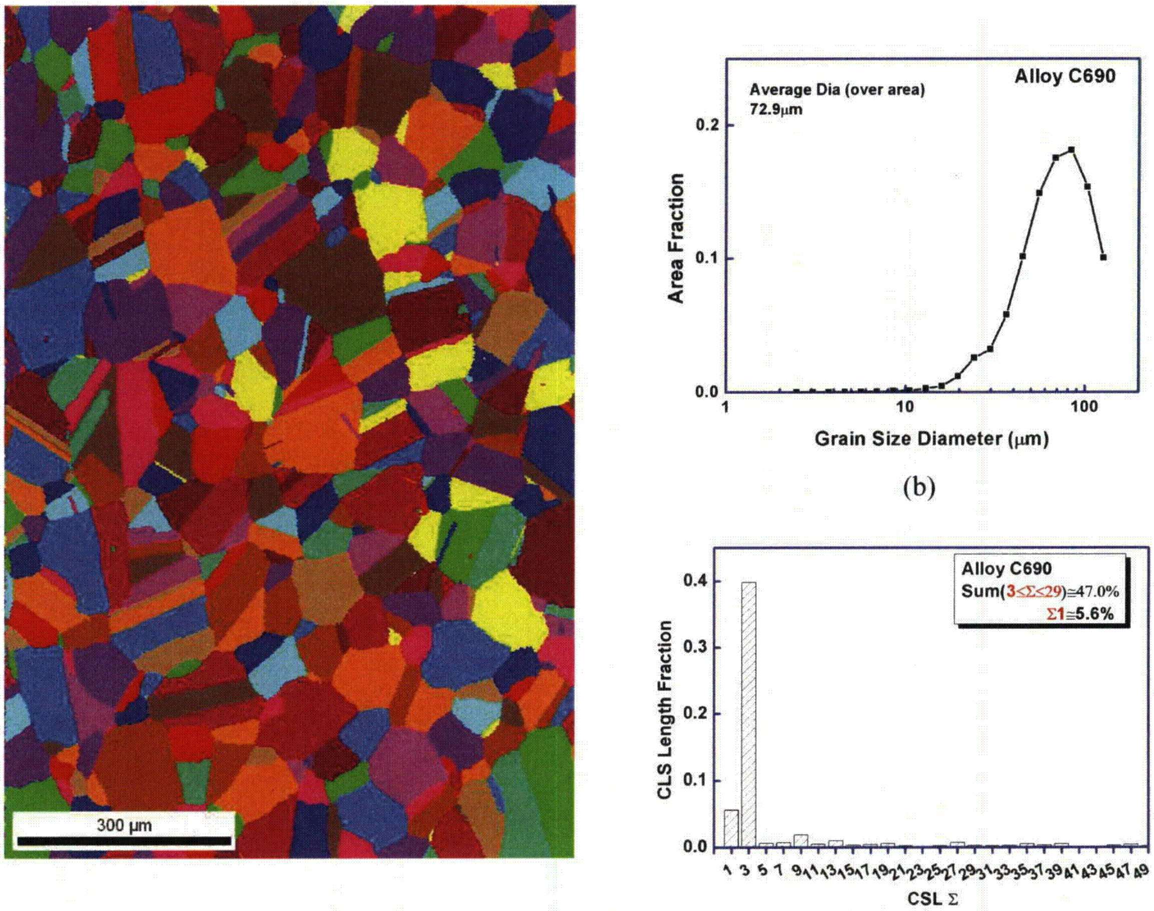

(b)

(a) (c)

Figure 28. **(a) OIM map, (b) graph of grain size distribution, and (c) graph of grain boundary character distribution for Alloy 690 TT from CRDM tubing.**

3.3 Alloy 152 Double-J Weld (A152)

The Alloy 152 double-J weld was examined by SEM, TEM, and OIM. The objective was to observe the microstructure, focusing on inclusions, and to determine the GBCD.

Figure 29 shows the microstructure of the Alloy 152 double-J weld, which has elongated, dendritic grains. The microstructure was also examined by optical microscopy and TEM. Several inclusions are visible in the images.

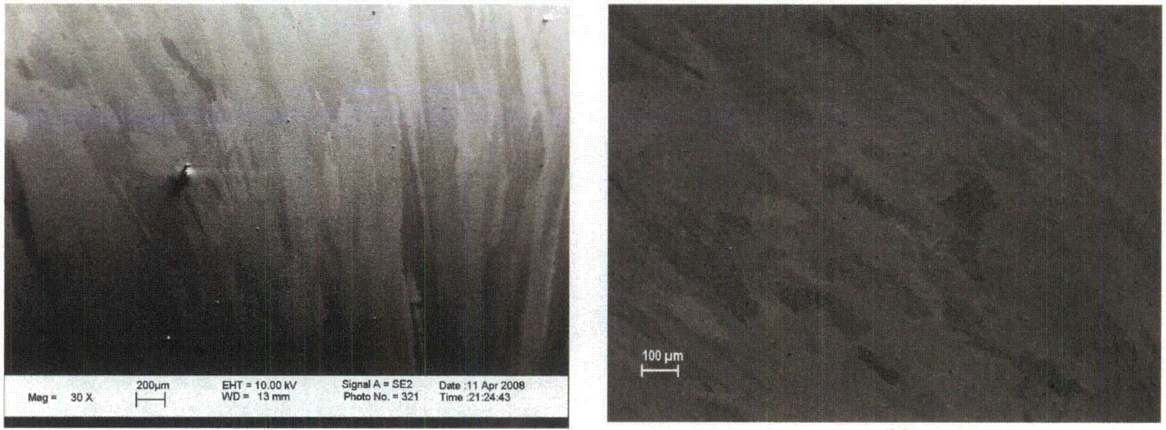

(a) (b)

Figure 29. Microstructure of Alloy 152 weld using SEM: (a) secondary electron detector and (b) back-scattered electron detector.

Figure 30 shows an optical micrograph where the micron-sized inclusions mentioned previously are visible. These appear to be of nearly identical size.

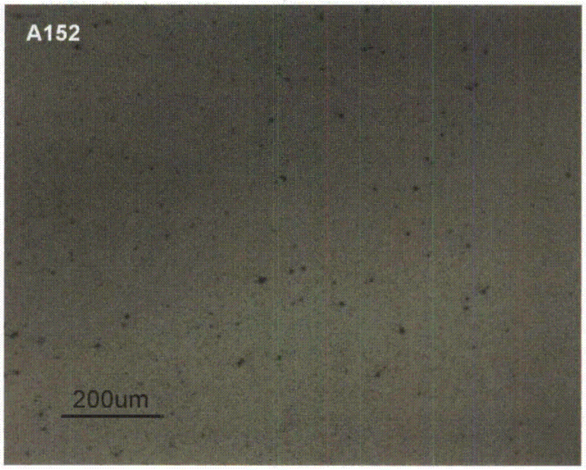

Figure 30.
Optical image of the Alloy 152 weld specimen A152.

The microstructure of the weld was also examined by TEM with the purpose of determining the nature of the inclusion noted previously. The TEM images are presented in Fig. 31. The microstructure appears to show a high density of dislocation loops and dislocation cells. Several inclusions were examined by energy dispersive x-ray spectroscopy (EDS). Results are given in Fig. 31d. These inclusions appear to be oxides, with the major components being Al and O.

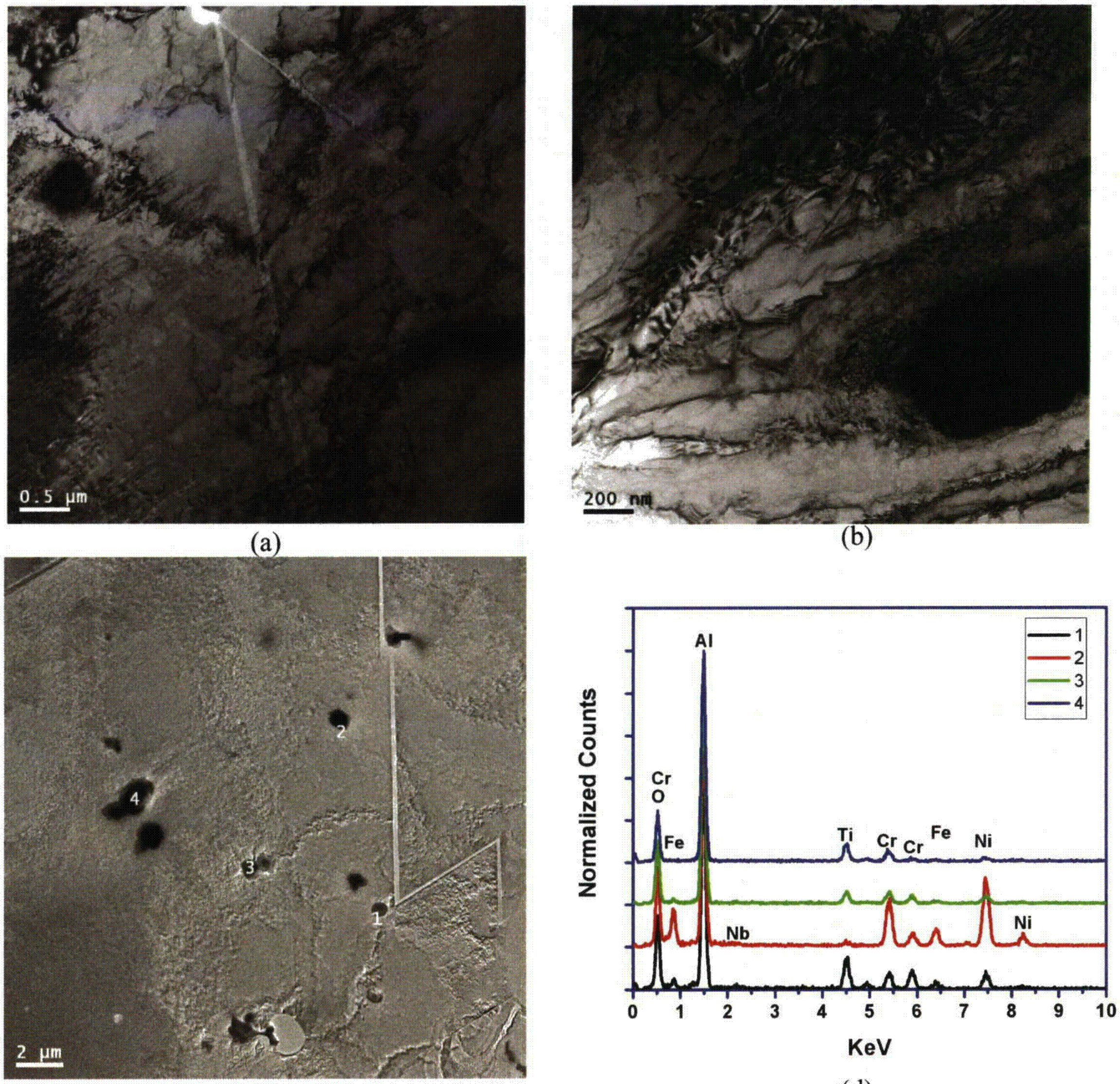

(a) (b)

(c) (d)

Figure 31. **(a-c) TEM images and (d) EDS spectrum of an inclusion in the double-J Alloy 152 weld (A152).**

Figure 32 summarizes the findings of the OIM analysis for the Alloy 152 weld. Figure 32a is a typical OIM map showing elongated dendritic grains, as noted previously. The resulting GBCD (Fig. 32b) is typical of Ni-base weld alloys.[8] As such, the CSLB fractions are approximately 36%. As expected, this weld also has a large proportion of low-angle boundaries (Σ=1).

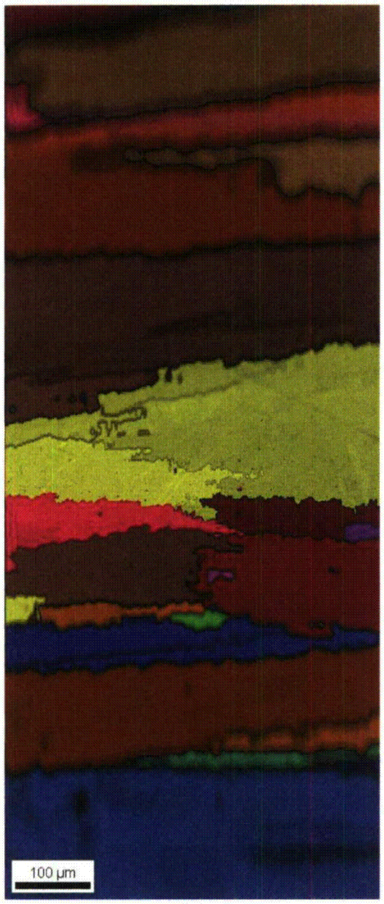

(a)

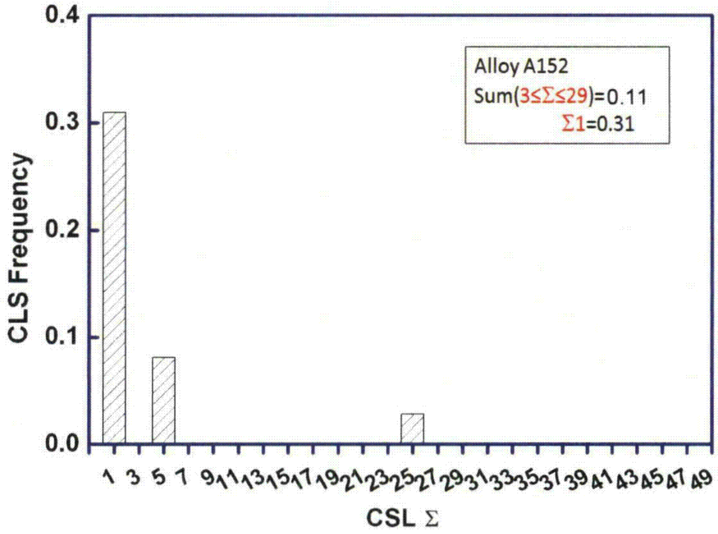

(b)

Figure 32.
Alloy 152 weld in double-J geometry (A152): (a) OIM map and (b) grain boundary character distribution.

4 Stress-Strain and Crack Growth Results

This section presents the tensile property data for Alloy 690TT (thermally treated) and 152 weld in the temperature range of 25-870°C (77-1598°F), as well as the CGR data for specimens in simulated PWR water. The CGR tests were conducted on Alloy 690 plate in the 26% cold-rolled condition, Alloy 690 CRDM tubing in the as-received condition, and Alloy 152 in the as-welded condition. Three tests have been conducted on Alloy 690 in the 26% cold-rolled condition, two tests on Alloy 690 in the as-received condition, and two tests on Alloy 152 weld.

4.1 Tensile Data for Alloy 690TT and Alloy 152 Double-J Weld

Tensile property data were obtained according to ASTM E8/E21[39] on Alloy 690 and Alloy 152 weld specimens as a function of temperature. The tests were conducted in air in the temperature range of 25-870°C (77-1598°F). Two specimens of each alloy were tested at each temperature in the test matrix. For these tests, Alloy 690 Heat NX3297HK12 was given an additional thermal treatment at 720ºC (1328ºF) for 10 h. Companion Alloy 600 specimens were also included in the test matrix. The Alloy 152 round bars were cut to ensure that the tensile specimens consist of only Alloy 152, not the adjacent Alloy 690 plate or the Alloy 52 weld root (Fig. 33). The available Alloy 152 weld piece allowed for 12 tensile specimens.

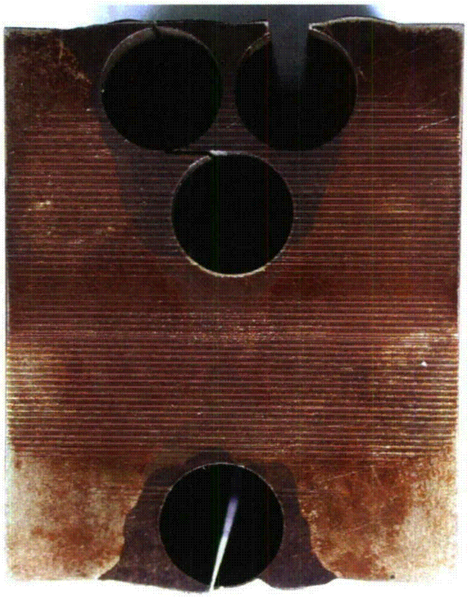

Figure 33.
Locations in the double-J Alloy 152 weld where the tensile specimens were cut.

The results of the tensile tests are shown in Table 8 for Alloy 690TT and in Table 9 for Alloy 152 weld. The data for both alloys meet the minimum requirements of ASME SB-167.

Table 8. Tensile properties of Alloy 690TT in the temperature range 25-870°C (77-1598°F).

Specimen ID	Temp., °F	Temp., °C	UTS, ksi	UTS, MPa	0.2% YS, ksi	0.2% YS, MPa	Elong., %	RA, %	Modulus, msi	Ult. Load, lb-f	0.2% Yield, lb-f	Orig. Dia., in.	Final Dia., in.
A690-1	77	25	96.8	667.4	42.7	294.4	50	65	29.5	9384	4143	0.3514	0.2079
A690-2	77	25	96.6	666.0	42.1	290.3	49	64	23.3	9368	4080	0.3513	0.2105
A690-3	302	150	88.2	608.1	36.1	248.9	46.5	62	31.6	8508	3482	0.3505	0.2156
A690-4	302	150	88.4	609.5	36.0	248.2	46.5	64	29.2	8521	3473	0.3503	0.21
A690-5	572	300	83.4	575.0	33.7	232.4	47	57	24.5	8086	3273	0.3514	0.2303
A690-6	572	300	83.7	577.1	33.5	231.0	48	60	25.8	8063	3231	0.3503	0.2221
A690-7	842	450	80.7	556.4	33.1	228.2	47	62.5	27.1	7780	3193	0.3504	0.2152
A690-8	842	450	80	551.6	32.8	226.1	48	60.5	25.3	7715	3159	0.3504	0.22
A690-9	1112	600	70.4	485.4	31.5	217.2	33.5	34	24.1	6826	3057	0.3513	0.285
A690-10	1112	600	72.6	500.6	29.7	204.8	38.5	41.5	26.2	7045	2880	0.3514	0.2693
A690-11	1382	750	38.4	264.8	28.3	195.1	49.5	49	20.8	3716	2740	0.3512	0.2502
A690-12	1382	750	38.4	264.8	28.4	195.8	48.5	46.5	21.1	3724	2752	0.3512	0.2574
A690-13	1598	870	18.3	126.2	15.8	108.9	43.5	76	16.2	1770	1536	0.3514	0.1728
A690-14	1598	870	17.4	120.0	15.0	103.4	75.5	75	17	1688	1450	0.3514	0.1754

Note: UTS = ultimate tensile strength, YS = yield strength, RA = reduction in area

Table 9. Tensile properties of Alloy 152 weld in the temperature range 25-870°C (77-1598°F).

Specimen ID	Temp., °F	Temp., °C	UTS, ksi	UTS, MPa	0.2% YS, ksi	0.2% YS, MPa	Elong., %	RA, %	Modulus, msi	Ult. Load, lb-f	0.2% Yield, lb-f	Orig. Dia., in.	Final Dia., in.
A152-11	77	25	93.8	646.7	61.7	425.4	44	54	19.4	4677	3073	0.2519	0.1705
A152-12	302	150	85.9	592.3	53.7	370.2	42	50.5	19.6	4275	2671	0.2517	0.1769
A152-13	572	300	85.6	590.2	59.6	410.9	39	48	23.5	4275	2975	0.2522	0.1815
A152-14	572	300	81.6	562.6	51.7	356.5	41	52	22.5	4061	2575	0.2518	0.1746
A152-21	842	450	76.7	528.8	47.9	330.3	45	51	15.8	3824	2386	0.2519	0.1761
A152-22	842	450	76.7	528.8	50.4	347.5	42	44.5	18.4	3827	2513	0.252	0.1877
A152-23	1112	600	70.8	488.1	50.2	346.1	34	38.5	16	3532	2507	0.2521	0.198
A152-24	1112	600	67.4	464.7	45.3	312.3	41	48.5	18.1	3360	2258	0.2519	0.1807
A152-31	1382	750	38.7	266.8	38.4	264.8	38	43	13.3	1934	1918	0.2522	0.1907
A152-32	1382	750	39.2	270.3	39.1	269.6	37	36.5	13.5	1953	1951	0.2519	0.2009
A152-33	1598	870	22.6	155.8	22.2	153.1	21	25.5	17.6	1125	1105	0.2519	0.2172
A152-34	1598	870	19.7	135.8	19.4	133.8	25	24.5	10.9	984	968	0.252	0.2187

Note: UTS = ultimate tensile strength, YS = yield strength, RA = reduction in area

The resulting stress-strain and true stress-true strain curves as a function of temperature for Alloy 690TT are shown in Fig. 34. As expected, the yield strength decreases with increasing temperature. Figure 35 shows the 0.2% YS and UTS as a function of temperature. Also included are data obtained on companion Alloy 600 specimens. Both 0.2% YS and UTS decrease with temperature. The data set for Alloy 690TT is in good agreement with control data on Alloy 600.

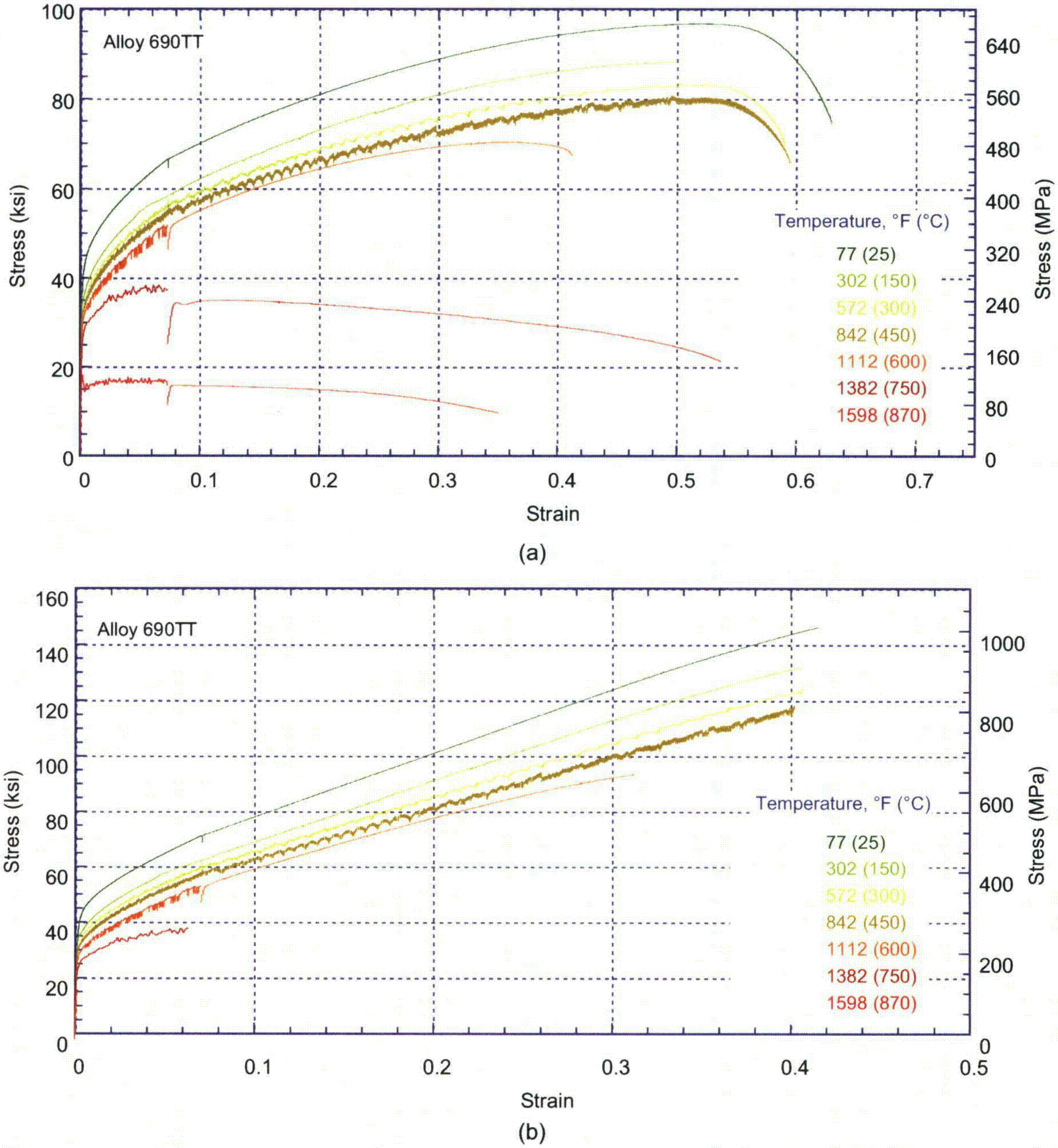

Figure 34. (a) Stress–strain and (b) true stress–true strain curves for Alloy 690 TT as a function of temperature.

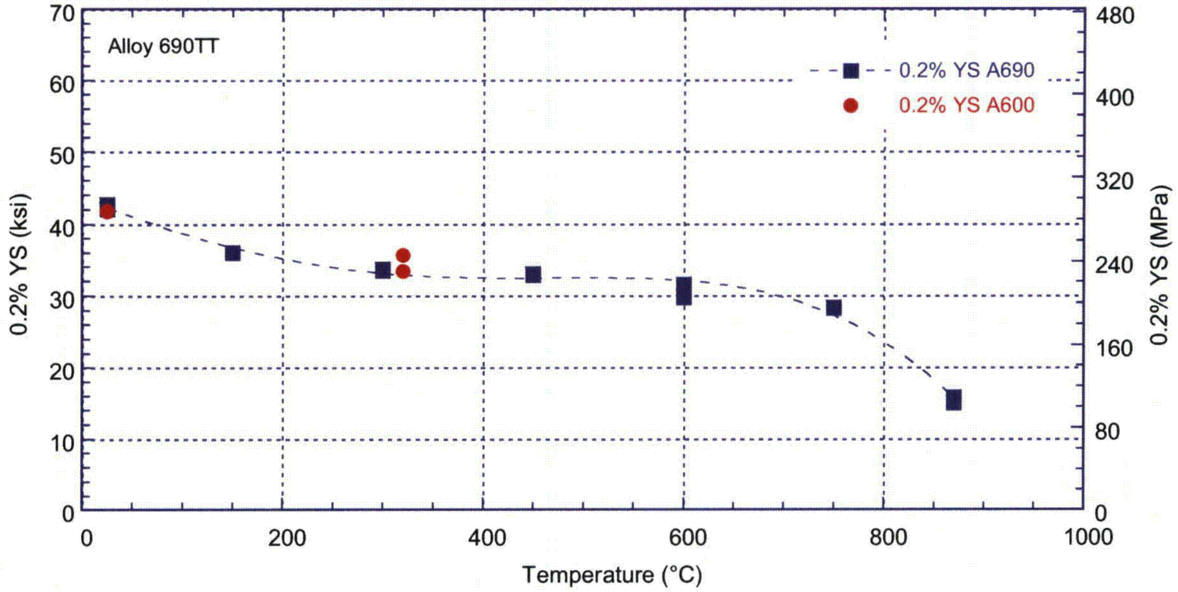

(a)

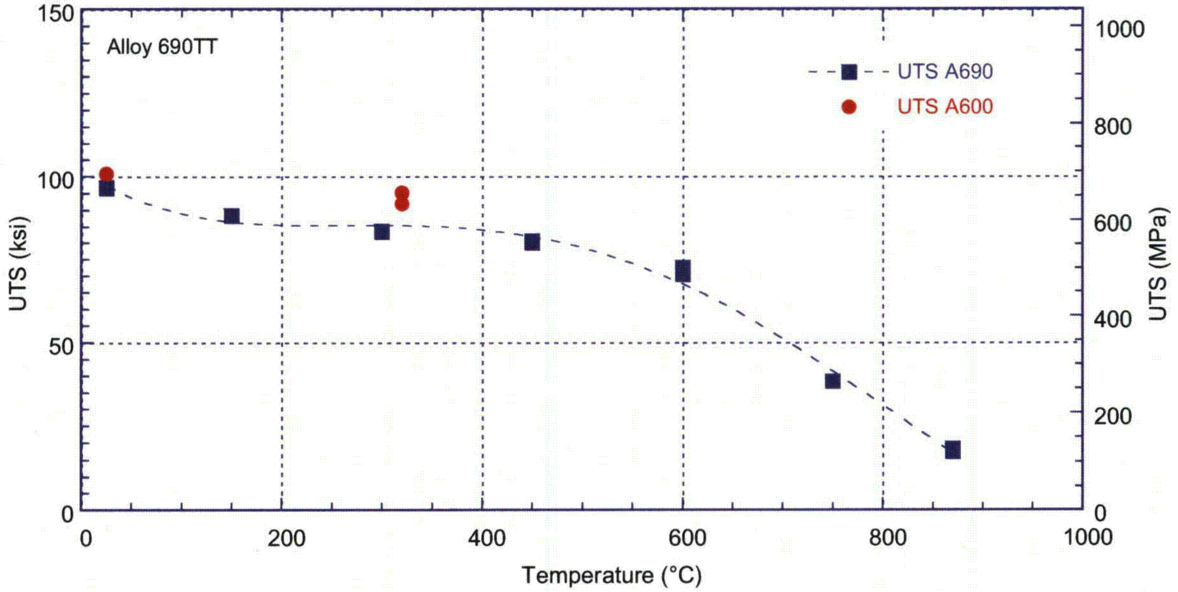

(b)

Figure 35. **(a) Yield stress and (b) ultimate tensile stress of Alloy 690TT as a function of temperature.**

The resulting stress-strain and true stress-true strain curves as a function of temperature for Alloy 152 weld are shown in Fig. 36. As expected, the yield strength decreases with increasing temperature. Figure 37 show the 0.2% YS and UTS as a function of temperature. Both the 0.2% YS and UTS decrease with temperature. Also included are data on Alloys 52/152 and 82 from other sources.[40] The data sets for Alloy 152 are in good agreement with the Alloy 82/152 data obtained elsewhere.[40]

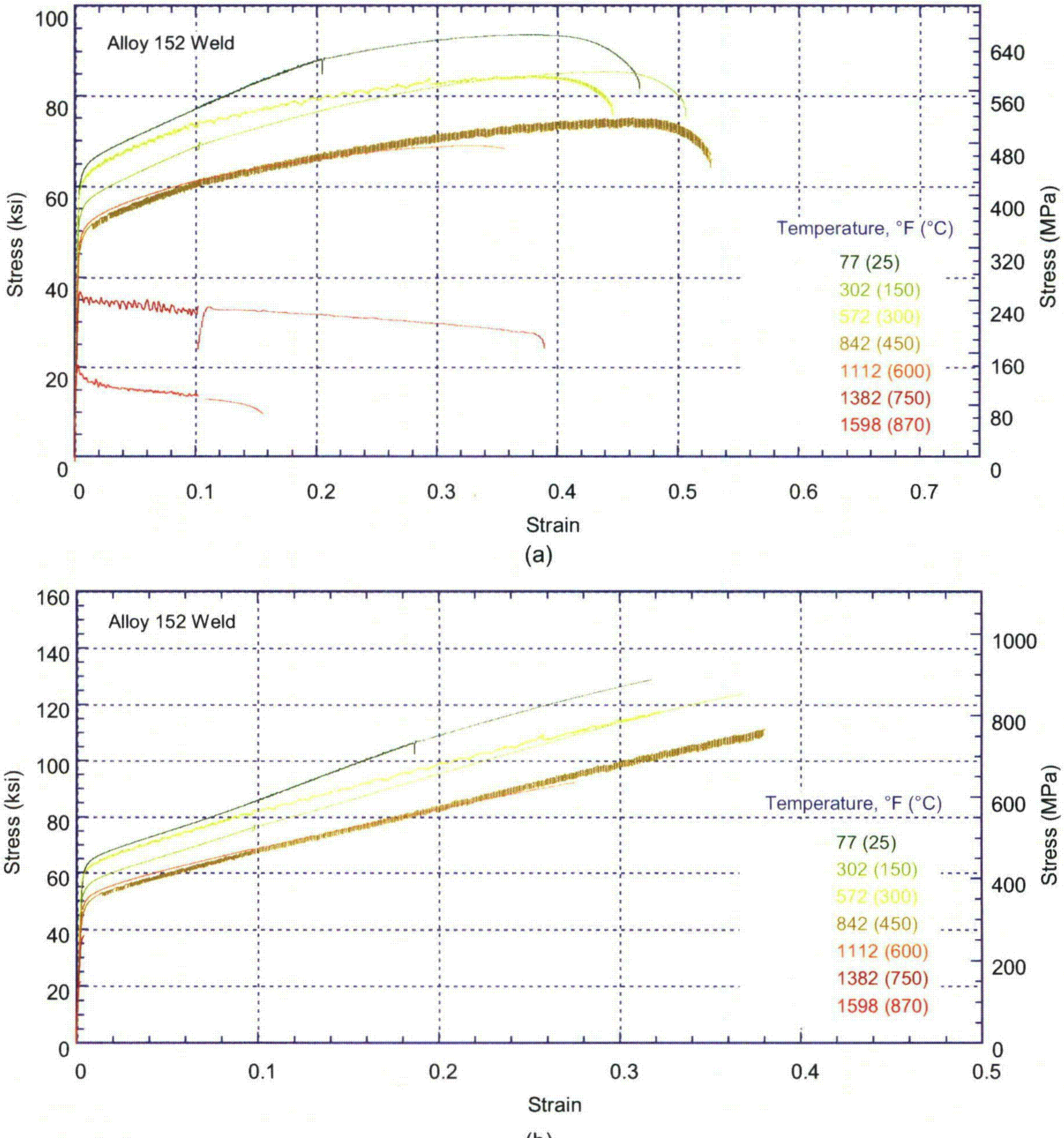

Figure 36. **(a) Stress–strain and (b) true stress–true strain curves for Alloy 152 weld as a function of temperature.**

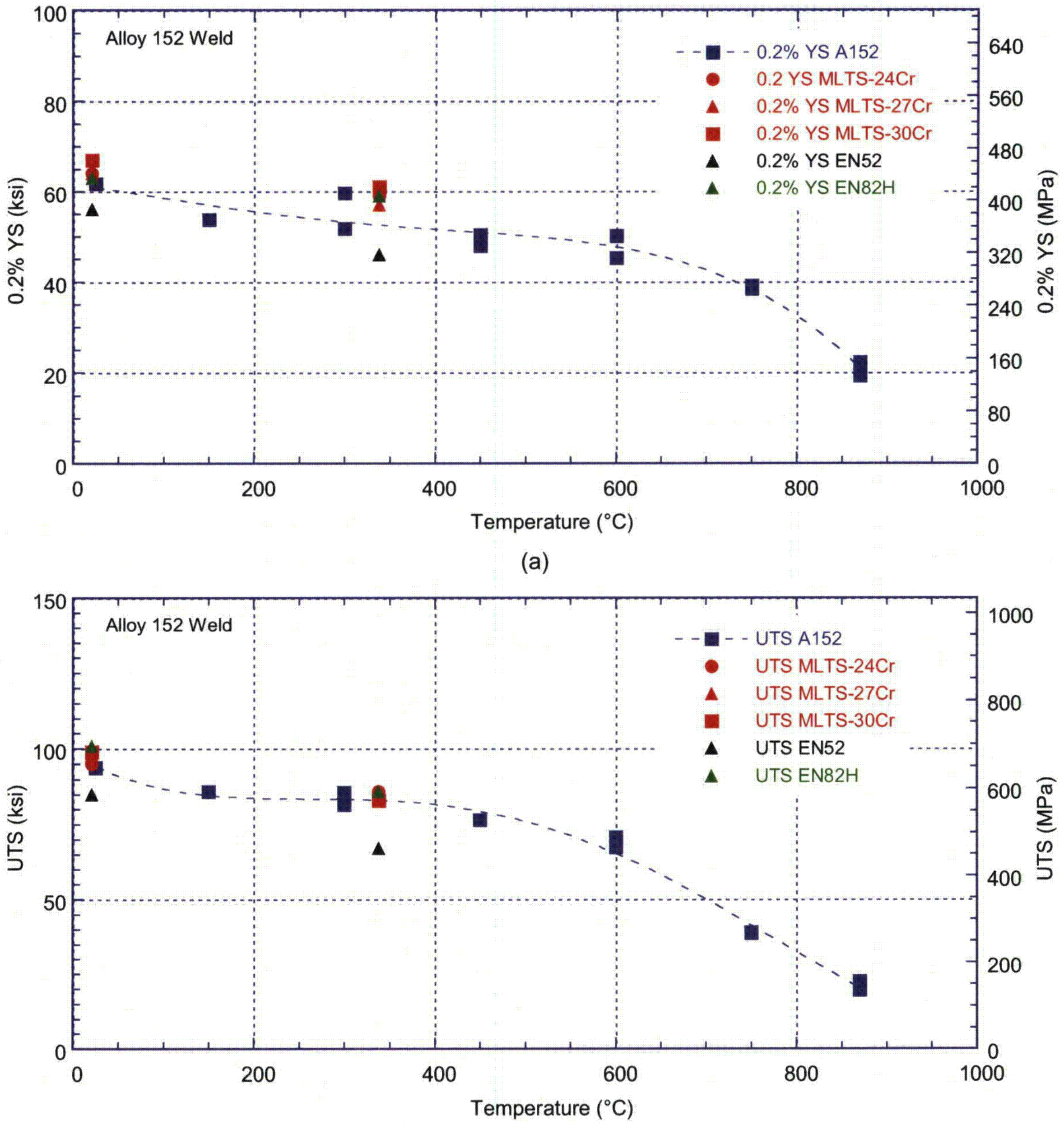

(a)

(b)

Figure 37. **(a) Yield stress and (b) ultimate tensile stress of Alloy 152 weld as a function of temperature.**

4.2 Crack Growth Data for Alloy 690 Cold-Rolled by 26%

Three CGR tests in simulated PWR environments were completed on Alloy 690 cold-rolled by 26%. These tests were conducted on ½-T CT specimens designated A690WC-SL-1, A690WC-ST-1, and A690WC-ST-2.

4.2.1 Specimen A690WC-SL-1

This test was a "screening" test at a time when no other similar data were available. The specimen orientation was chosen to be SL, as this was expected to be the most susceptible to SCC. Standard transitioning procedures developed for Alloys 600 and 182 were applied. During the constant load portion of the test (Period 9), no periodic unloading was used.

The testing conditions for Specimen A690WC-SL-1 are given in Table 10, and the changes in crack length and K_{max} with time are shown in Fig. 38. Surprisingly, transitioning from TG to IG SCC occurred readily. The measured CGRs at constant load were between 1.5 and 2.8 x 10^{-11} m/s for K_{max} = 26.7-28 MPa·m$^{1/2}$ (24.3-25.5 ksi·in.$^{1/2}$).

Table 10. Crack growth data for specimen A690WC-SL-1 in PWR water[a] at 320°C.

Test Period	Test Time, h	Load Ratio R	Rise Time, s	Down Time, s	Hold Time, s	K_{max}, MPa·m$^{1/2}$	ΔK, MPa·m$^{1/2}$	CGR_{env}, m/s	Estimated CGR_{air}, m/s	Crack Length, mm
1	48	0.30	0.50	0.5	0	19.4	13.6	2.44E-08	1.89E-08	11.772
2	62	0.30	50	50	0	19.9	13.95	1.45E-09	2.12E-10	11.973
3	80	0.30	0.5	0.5	0	21.0	14.7	4.96E-08	2.67E-08	12.731
4	105	0.50	50.0	12	0	25.2	12.6	2.57E-09	2.39E-10	12.958
5a	170	0.50	500	12	0	25.8	12.9	5.45E-10	2.62E-11	13.081
5b	216	0.50	500	12	0	25.9	12.9	5.33E-10	2.71E-11	13.173
6	346	0.50	500	12	0	26.2	13.1	3.63E-10	1.41E-11	13.318
7	2190	1.00	0	0	0	26.2	0.0	1.46E-11	-	13.447
8	2234	0.50	500	12	0	27.8	13.9	7.15E-10	3.58E-11	13.561
9	2831	1.00	0	0	0	28.0	0.0	2.83E-11	-	13.627
10	2854	0.50	50	120	0	29.7	20.8	4.31E-09	1.09E-09	13.983

[a] Simulated PWR water with 2 ppm Li, 1000 ppm B, DO<10 ppb. Conductivity was 21 ± 3 µS/cm, and pH 6.4.

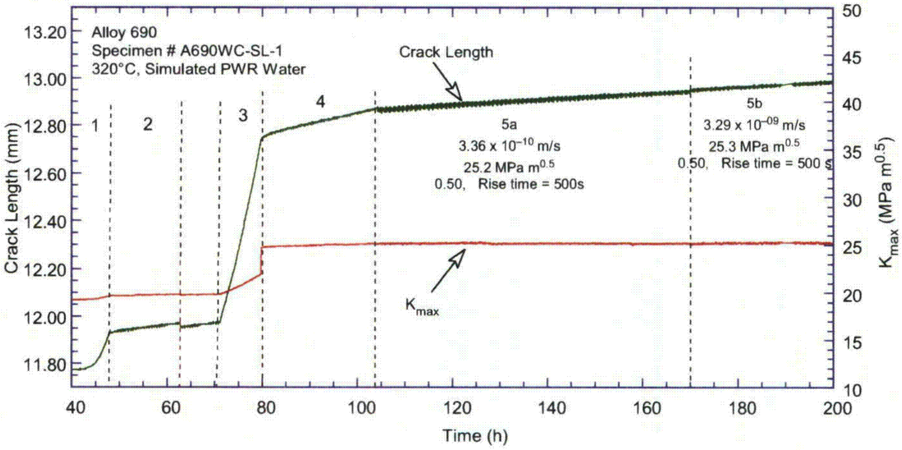

(a)

Figure 38. Crack length vs. time for Alloy 690 specimen A690WC-SL-1 in simulated PWR environment during test periods (a) 1-5 and (b) 6-9.

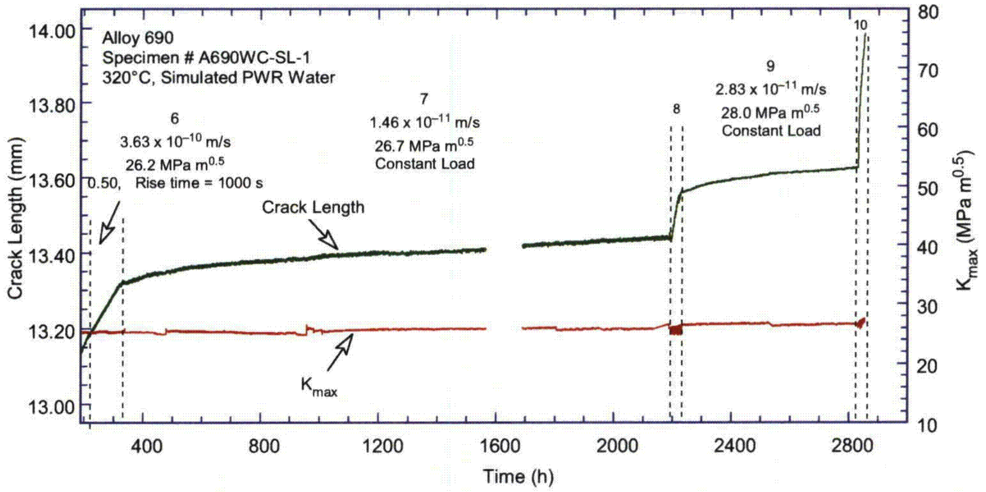

(b)

Figure 38 (cont.)

The resulting fracture surface was examined by both optical and electron microscopy. Figure 39 shows the fracture surface of the specimen by both optical and electron microscopy. The images indicate that the testing procedure resulted in a straight, uniform fracture surface. Two fracture modes can be distinguished: TG, corresponding to mechanical fatigue, and IG SCC. The images shown in Fig. 39 were used to determine the correction factors for the DC potential data. No correction was necessary for the mechanical fatigue periods, and a factor of 2.24 was applied to the SCC periods.

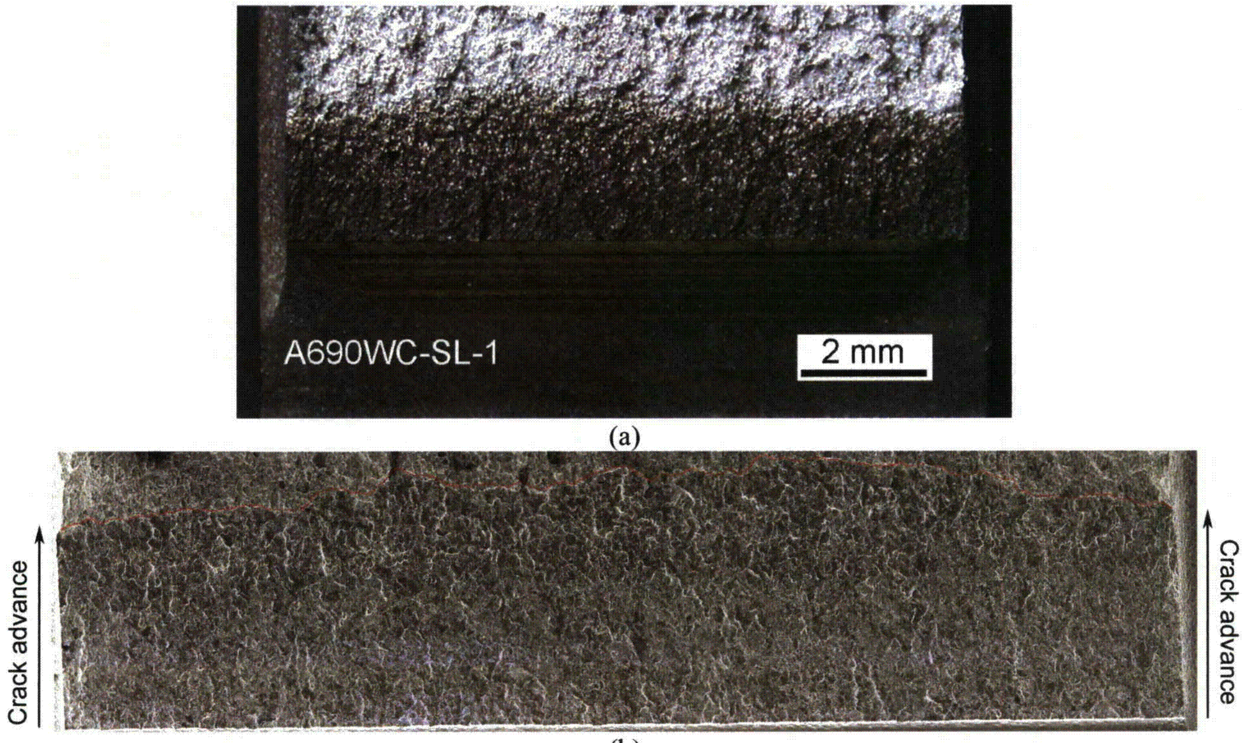

(b)

Figure 39. Fracture surface of specimen A690WC-SL-1 by (a) optical and (b) electron microscopy.

Figure 40 illustrates the fracture modes that were observed: (a) TG, corresponding to the mechanical fatigue periods, and (b) faceted IG, almost "granular," corresponding to the SCC periods. Figures 40c and 40d show additional images. Of interest are the secondary cracks and, especially, the cracked carbides on the facets.

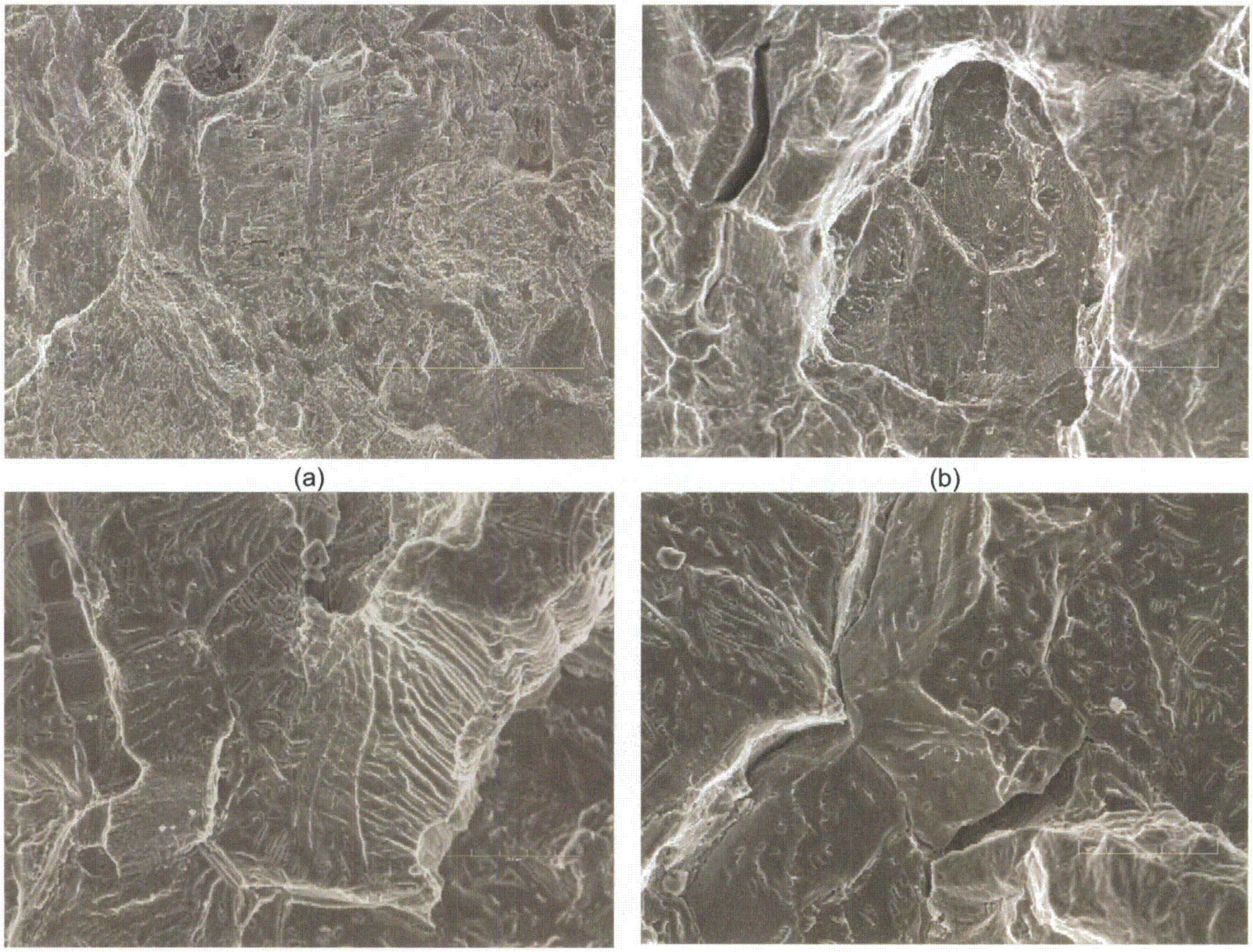

(a) (b) (c) (d)

Figure 40. Fracture modes observed on the fracture surface of A690WC-SL-1: (a) transgranular; (b,c) faceted with elements of IG; and (d) IG showing carbides on the facets. Crack advance is from bottom to top.

Figure 41 shows an additional set of micrographs from the fracture surface of specimen A690WC-SL-1 with the purpose of comparing the features observed on the TG and IG fracture surfaces. Figure 41a is a low magnification micrograph showing both fracture morphologies: TG, corresponding to the mechanical fatigue test periods, and faceted IG, corresponding to the SCC periods. Figure 41b shows the IG region where secondary cracks can also be observed. Figures 41c and 41d show the TG fracture mode; however, elements of IG cracking – granular appearance and smooth facets – are also apparent.

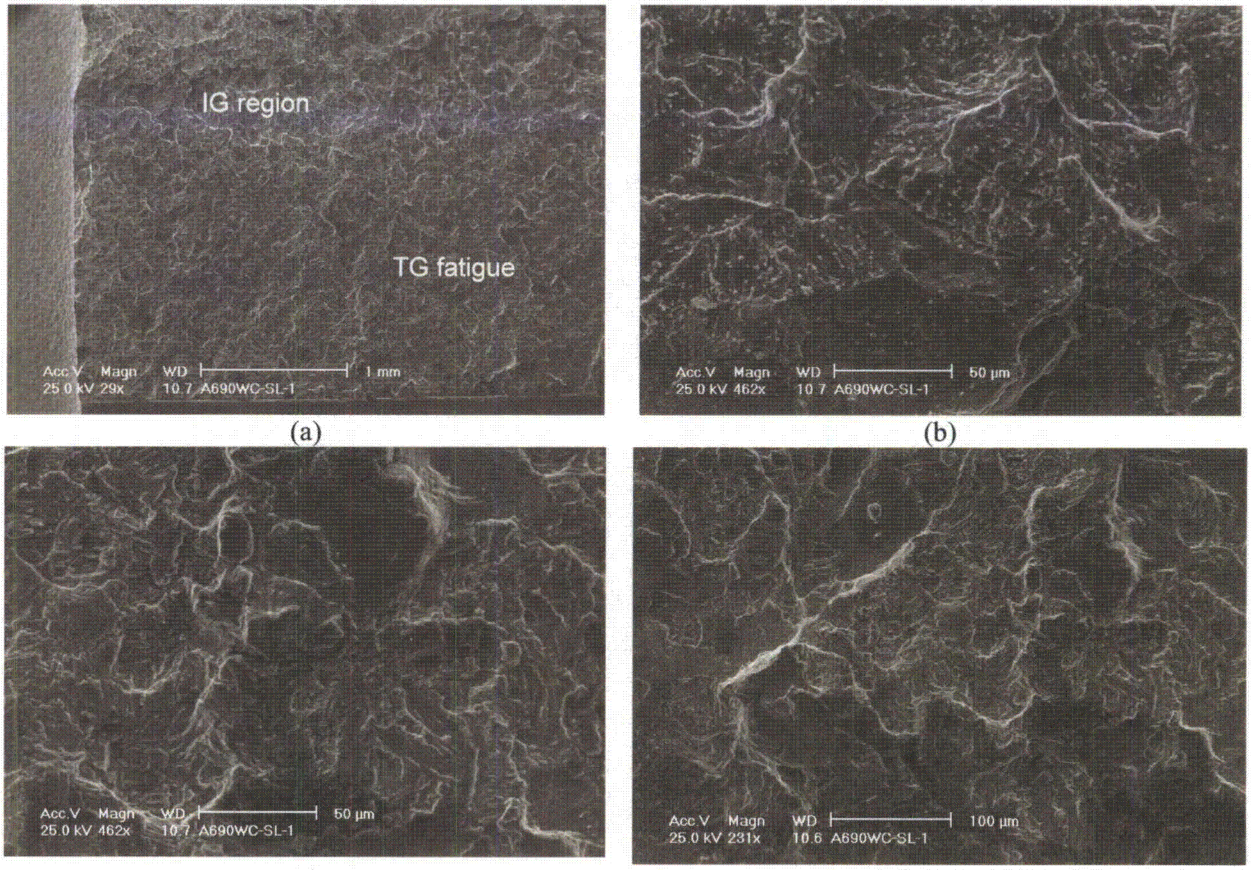

(a) (b)

(c) (d)

Figure 41. Fracture modes observed on the fracture surface of A690WC-SL-1: (a) IG and TG, (b) IG fracture, and (c,d) TG fracture with elements of IG (smooth facets). Crack advance is from bottom to top.

To examine the fracture characteristics in more detail, the surface oxides were removed by standard metallographic procedures. Figure 42 shows a set of micrographs after the oxides were removed. Figures 42a and 42b show the IG region. The fracture mode appears to be a combination of "granular" and smooth IG, and a higher number density of narrow secondary cracks is now visible. Figure 42c shows the TG fracture mode; however, as noted previously, elements of IG cracking – granular appearance, smooth facets, and narrow secondary cracks – are visible.

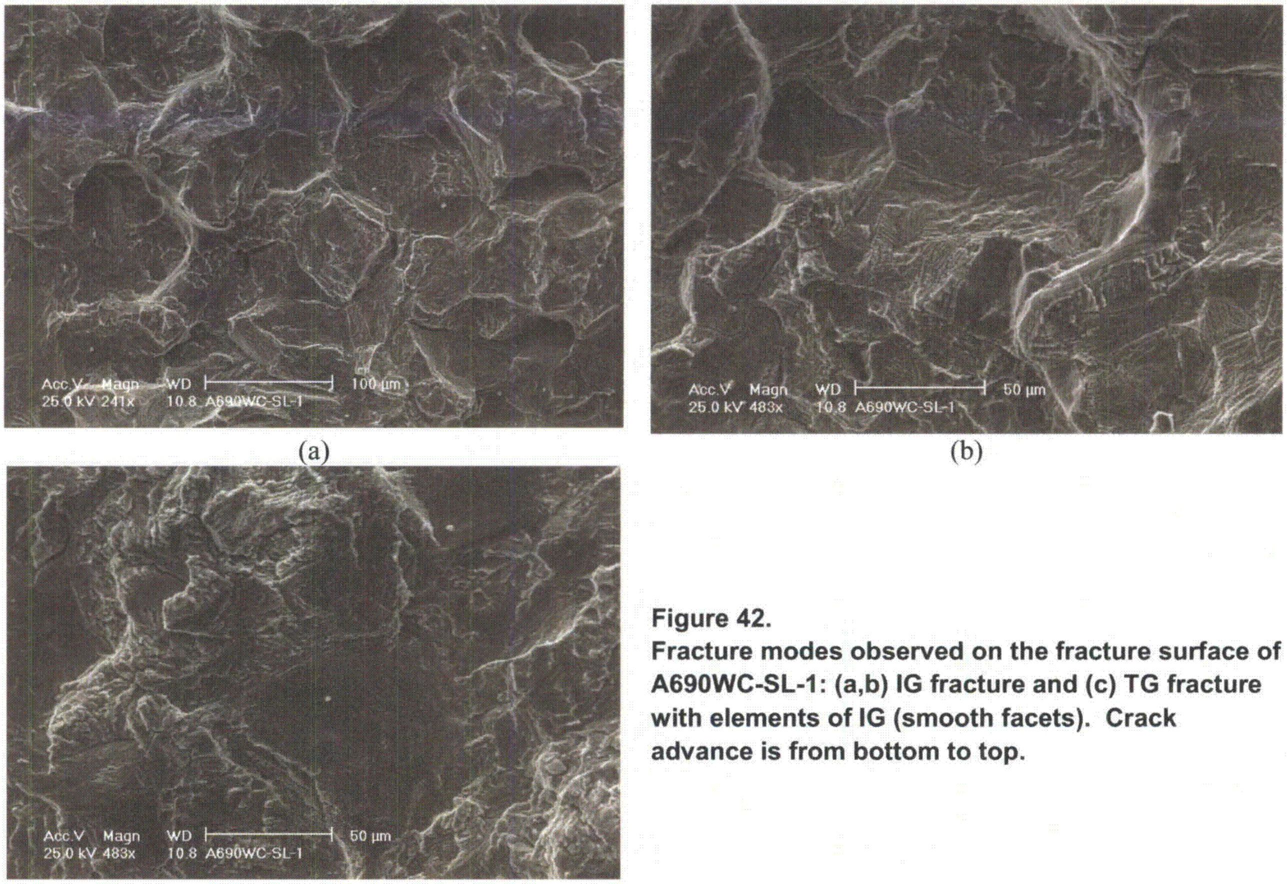

(a) (b)

(c)

Figure 42.
Fracture modes observed on the fracture surface of A690WC-SL-1: (a,b) IG fracture and (c) TG fracture with elements of IG (smooth facets). Crack advance is from bottom to top.

Figure 43 shows a cross section of specimen A690WC-SL-1. The side of the specimen was mechanically polished by finishing with a 1-µm diamond paste, then was electrochemically etched in 10% nital solution to show grain boundaries. Figure 43a shows the entire crack length, and arrows mark the beginning of the IG portion of the crack and the end of the test. The overall crack appearance is straight, with no departures from the initial test plane. Figure 43b shows the IG region at a higher magnification. As noted previously, because there is no significant deviation from the initial test plane, the crack does not appear to favor any particular microstructure. Crack branching or deep secondary cracks were not observed on the cross section.

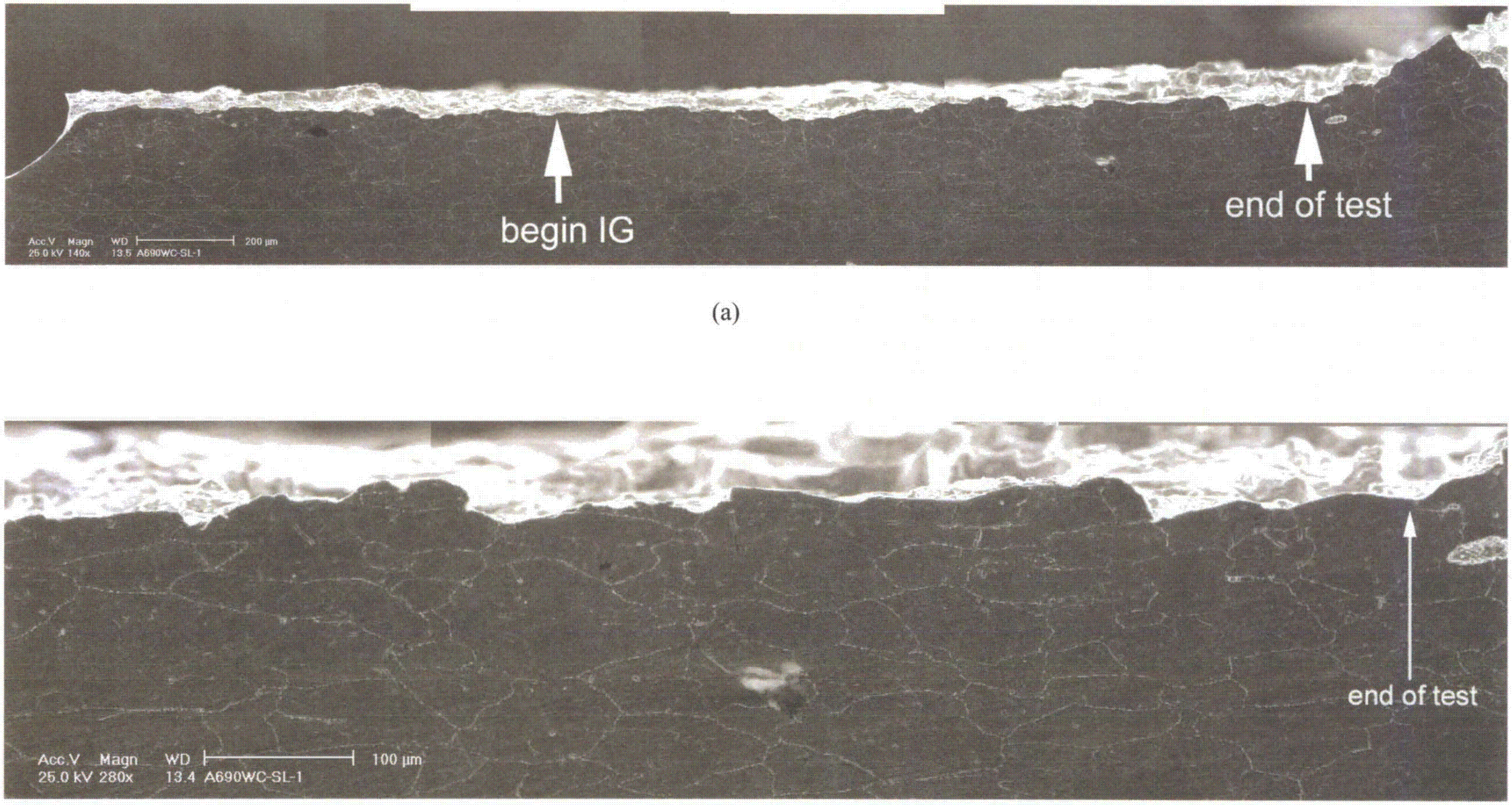

(a)

(b)

Figu Figure 43. Cross section of specimen A690WC-SL-1: (a) entire (IG and TG) crack front and (b) IG region at the end of test.

4.2.2 Specimen A690WC-ST-1

This test was conducted on a companion specimen to the one tested previously. As with the previous specimen, the crack front was in the mid-plane of the 26% cold-rolled plate, while the direction was normal to the rolling direction. As in the previous test, standard transitioning procedures were applied, and no hold times or periodic unloading was used.

The testing conditions for Specimen A690WC-ST-1 are given in Table 11, and the changes in crack length and K_{max} with time are shown in Fig. 44. The measured CGRs at constant load were between 1.31 and 3.3 x 10^{-11} m/s for $K_{max} = 31.3$ MPa·m$^{1/2}$ (28.5 ksi·in.$^{1/2}$), in good agreement with the previous specimen.

Table 11. Crack growth data for specimen A690WC-ST-1 in PWR water[a] at 320°C.

Test Period	Test Time, h	Temp., °C	Load Ratio R	Rise Time, s	Down Time, s	K_{max}, MPa·m$^{1/2}$	ΔK, MPa·m$^{1/2}$	CGR_{env}, m/s	Estimated CGR_{air}, m/s	Crack Length, mm
Pre a	27	319.8	0.28	0.5	0.5	20.4	14.7	4.02E-08	2.51E-08	12.062
Pre b	44	319.9	0.28	50	50	20.6	14.8	2.10E-09	2.62E-10	12.129
Pre c	49	319.8	0.28	0.5	0.5	22.4	16.1	5.60E-08	3.66E-08	12.618
1	75	319.8	0.47	50	12	23.2	12.3	1.44E-09	1.98E-10	12.746
2	139	319.8	0.46	300	12	24.1	13.0	1.00E-09	4.06E-11	12.977
3	212	319.8	0.45	600	12	24.3	13.3	5.65E-10	2.18E-11	13.111
4	309	319.7	0.45	1000	12	24.9	13.7	3.75E-10	1.48E-11	13.260
5	407	319.7	0.67	1000	12	25.6	8.4	9.81E-11	4.21E-12	13.287
6	476	319.7	0.45	1000	12	25.9	14.2	3.76E-10	1.71E-11	13.366
7	714	319.7	0.45	4350	12	26.1	14.3	1.18E-10	4.06E-12	13.471
8	810	319.7	0.48	1000	12	26.7	13.9	5.59E-10	1.69E-11	13.648
9	1413	319.6	1.00	0	0	27.2	0.0	2.08E-12	-	13.674
10	1816	319.4	1.00	0	0	31.3	0.0	1.31E-11	-	13.697
11	1816	319.4	1.00	0	0	29.9	0.0	4.76E-12	-	13.711
12	1816	319.4	0.49	300	12	30.7	15.6	2.07E-09	9.41E-11	13.880
13	4000	319.5	1.00	0	0	31.4	0.0	3.27E-11	-	14.040

[a] Simulated PWR water with 2 ppm Li, 1000 ppm B, DO <10 ppb. Conductivity was 21 ± 3 μS/cm, and pH 6.4.

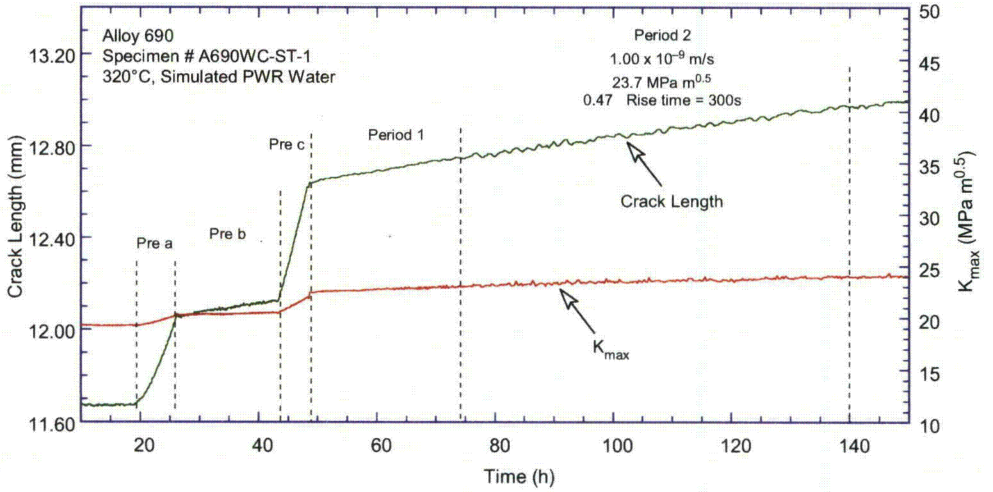

(a)

Figure 44. Crack length vs. time for Alloy 690 Specimen A690WC-ST-1 in simulated PWR environment during test periods (a) precracking-2, (b) 3-7, (c) 8-11, and (d) 12-13.

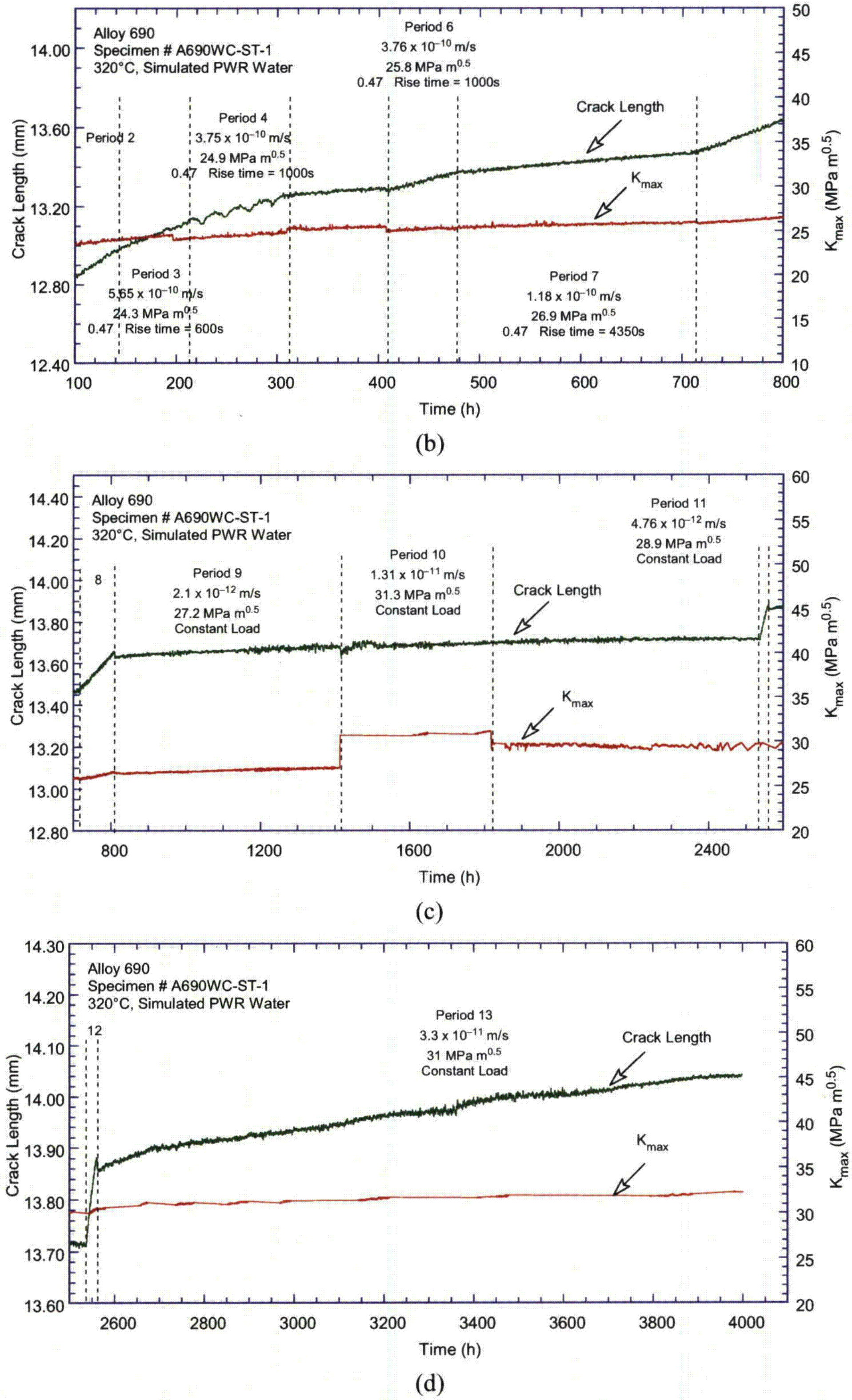

Figure 44. **(cont.)**

The resulting fracture surface was examined by both optical and electron microscopy. Figure 45 shows the fracture surface of specimen A690WC-ST-1 as determined by optical microscopy. The image indicates that the testing procedure resulted in a straight, uniform fracture surface. Two fracture modes – TG, corresponding to mechanical fatigue, and IG SCC – can be distinguished. The image shown in Fig. 45 was used to determine the correction factors for the DC potential data. No correction was necessary for the mechanical fatigue periods, and a factor of 2.15 was applied to the SCC periods.

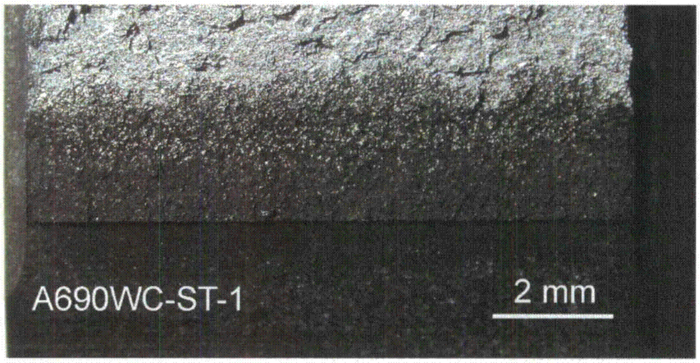

Figure 45. Fracture surface of specimen A690WC-ST-1. Crack advance is from bottom to top.

Figure 46 illustrates the fracture modes observed. Figure 46a shows the TG fracture mode, corresponding to the mechanical fatigue periods, and Figs. 46b and 46c show the faceted IG – almost "granular" – fracture mode, corresponding to the SCC periods.

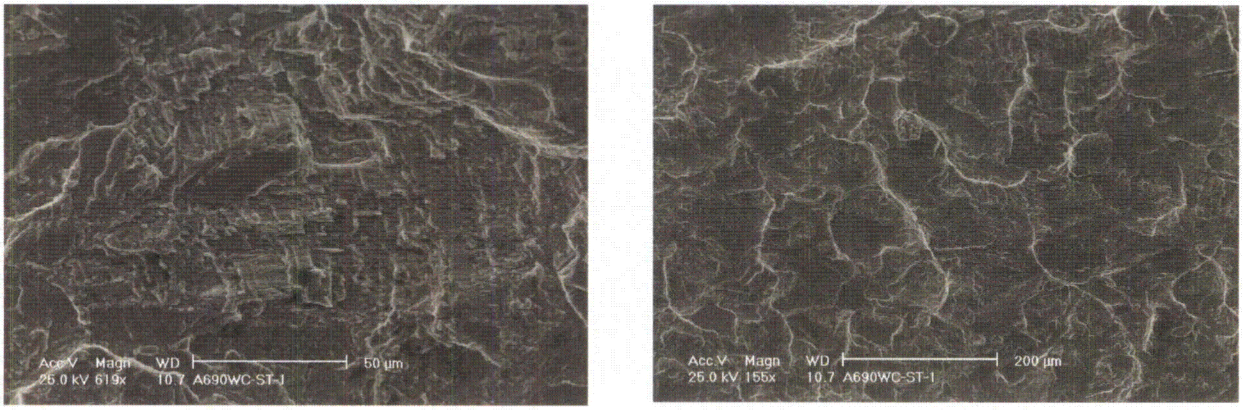

(a) (b)

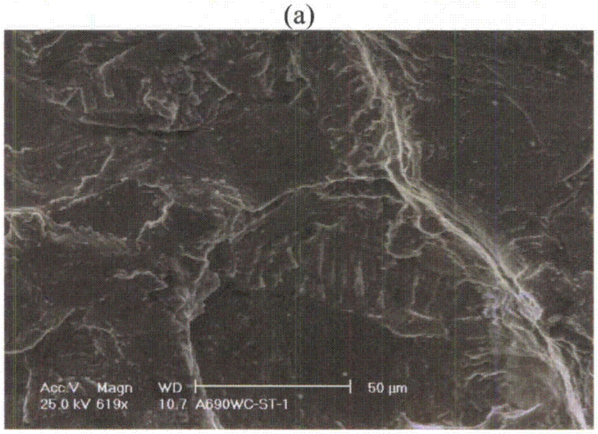

(c)

Figure 46.
Fracture modes observed on the fracture surface of A690WC-ST-1: (a) TG, (b) IG fracture, and (c) IG fracture detail. Crack advance is from bottom to top.

4.2.3 Specimen A690WC-ST-2

This test was conducted to determine the activation energy for SCC crack growth in Alloy 690 cold-rolled by 26%. The approach was to perform a test on a single specimen and observe the effects of changes in temperature on a propagating crack.

The test conditions for Specimen A690WC-ST-2 are given in Table 12, and the changes in crack length and K_{max} with time are shown in Fig. 47.

Table 12. Crack growth data for specimen A690WC-ST-2 of Alloy 690 in PWR water.[a]

Test Period	Test Time, h	Temp., °C	Load Ratio R	Rise Time, s	Down Time, s	Hold Time, s	K_{max}, MPa·m$^{1/2}$	ΔK, MPa·m$^{1/2}$	CGR_{env}, m/s	Estimated CGR_{air}, m/s	Crack Length, mm
Pre a	510	350.4	0.29	1	1	0	18.2	12.9	7.65E-09	9.26E-09	11.755
Pre b	647	350.0	0.29	100	100	0	18.4	13.0	3.23E-10	9.71E-11	11.828
Pre c	654	350.0	0.29	1	1	0	18.8	13.4	1.57E-08	1.07E-08	12.032
Pre d	671	349.7	0.29	50	50	0	18.9	13.4	8.40E-10	2.17E-10	12.059
1	743	350.0	0.60	50	12	0	18.9	7.6	1.08E-10	5.07E-11	12.084
2	841	349.9	0.62	50	12	0	19.9	7.6	2.80E-10	5.38E-11	12.131
3	959	349.2	0.62	300	12	0	19.9	7.6	8.48E-10	9.16E-12	12.167
4	1,014	349.6	0.62	600	12	0	20.0	7.6	6.16E-11	4.62E-12	12.178
5	1,183	349.2	0.62	1000	12	0	20.1	7.6	5.56E-11	2.80E-12	12.211
6	1,384	349.5	1.00	0	0	0	20.2	0.0	5.57E-12	-	12.217
7	1,473	349.9	0.49	300	12	0	24.2	12.3	2.90E-10	4.37E-11	12.244
8	1,487	349.8	0.49	600	12	0	24.2	12.4	1.78E-10	2.20E-11	12.266
9	1,511	349.5	0.49	1000	12	0	24.2	12.4	9.42E-11	1.31E-11	12.271
10	1,917	350.0	0.49	300	12	0	24.6	12.5	3.42E-10	4.69E-11	12.370
11	1,990	349.7	0.49	600	12	0	24.7	12.6	1.81E-10	2.39E-11	12.418
12	2,085	349.4	0.49	1000	12	0	24.8	12.7	1.29E-10	1.46E-11	12.462
13	2,189	350.3	0.48	300	12	0	25.0	13.0	2.41E-10	5.28E-11	12.534
14	2,194	352.2	0.48	600	12	0	24.9	13.0	2.33E-10	2.64E-11	12.539
15	2,210	321.5	0.43	300	12	0	23.1	13.2	6.43E-10	3.97E-11	12.570
16	2,234	321.1	0.43	600	12	0	23.2	13.2	2.63E-10	2.02E-11	12.592
17	2,282	321.3	0.43	1000	12	0	23.4	13.3	1.63E-10	1.24E-11	12.621
18	2,404	320.3	1.00	0	0	0	23.4	0.0	4.04E-12	-	12.624
19	2,410	320.4	0.49	300	12	0	24.9	12.7	6.94E-10	4.02E-11	12.634
20	2,428	320.2	0.49	600	12	0	24.9	12.7	3.02E-10	2.04E-11	12.652
21	2,536	319.7	0.49	1000	12	0	25.1	12.8	1.83E-10	1.25E-11	12.727
22	2,698	320.7	0.49	1000	12	3600	25.5	12.9	6.45E-11	1.33E-11	12.769
23	2,938	319.9	0.49	1000	12	7200	25.6	13.0	6.15E-11	1.35E-11	12.820
24	3,799	320.1	1[b]	0	0	0	25.8	-	2.54E-11	-	12.890
25	4,154	311.9	1[b]	0	0	0	26.0	-	2.63E-11	-	12.925
26	4,747	319.7	1[b]	0	0	0	25.9	-	2.84E-11	-	12.993
27	5,090	300.0	1[b]	0	0	0	26.4	-	3.77E-11	-	13.039

[a] Simulated PWR water with 2 ppm Li, 1000 ppm B, DO <10 ppb. Conductivity was 21 ± 3 μS/cm, and pH 6.4.
[b] Includes periodic unloading by 50% (12 s/12 s) every 8 h.

The test was initiated at 350°C (662°F) with a dissolved hydrogen concentration of 50 cc/kg. This concentration maintains approximately the same potential difference between the specimen and the Ni/NiO line (Table 6) as the standard testing environment used at ANL (320°C or 608°F, 23 cc/kg dissolved hydrogen). However, the environmental enhancement of cyclic rates was less than in the previous two tests (Fig. 48). While the reason for the observed behavior is unknown, it was decided to return to the standard testing environment to transition the crack from TG to IG. Given the relatively low SCC CGRs initially measured for this specimen, it was also decided to continue load cycling and introduced hold times to determine the SCC CGR component by superposition. Periods 22 and 23 had the same loading as period 21, but hold times of 3600 s and 7200 s, respectively. Using the superposition model (Eq. 10), SCC CGR components of 2.97 x 10^{-11} m/s and 3.52 x 10^{-11} m/s were calculated for periods 22 and 23, respectively. These rates are in good agreement with those measured previously for this alloy condition. Next, an unload/reload cycle was introduced. The sample was initially cycled every 2 h, then the hold period was increased to 4 h and 8 h. At approximately 3 cycles per day (period 24), the rate appeared to have stabilized to 2.54 x 10^{-11} m/s again in good agreement with previous determinations on this alloy condition and temperature. The temperature was decreased to 310°C (590°F); no significant effect on the CGR (2.63 x 10^{-11} m/s) was observed. The temperature was increased back to 320°C (608°F), and again the CGRs were essentially unchanged (2.86 x 10^{-11} m/s). With a more drastic change in temperature, to 300°C (572°F), the rate still stayed unchanged. In summary, the behavior suggests that for this cold-rolled alloy, once a steady-state SCC CGR is achieved, changes in temperature do not affect that rate.

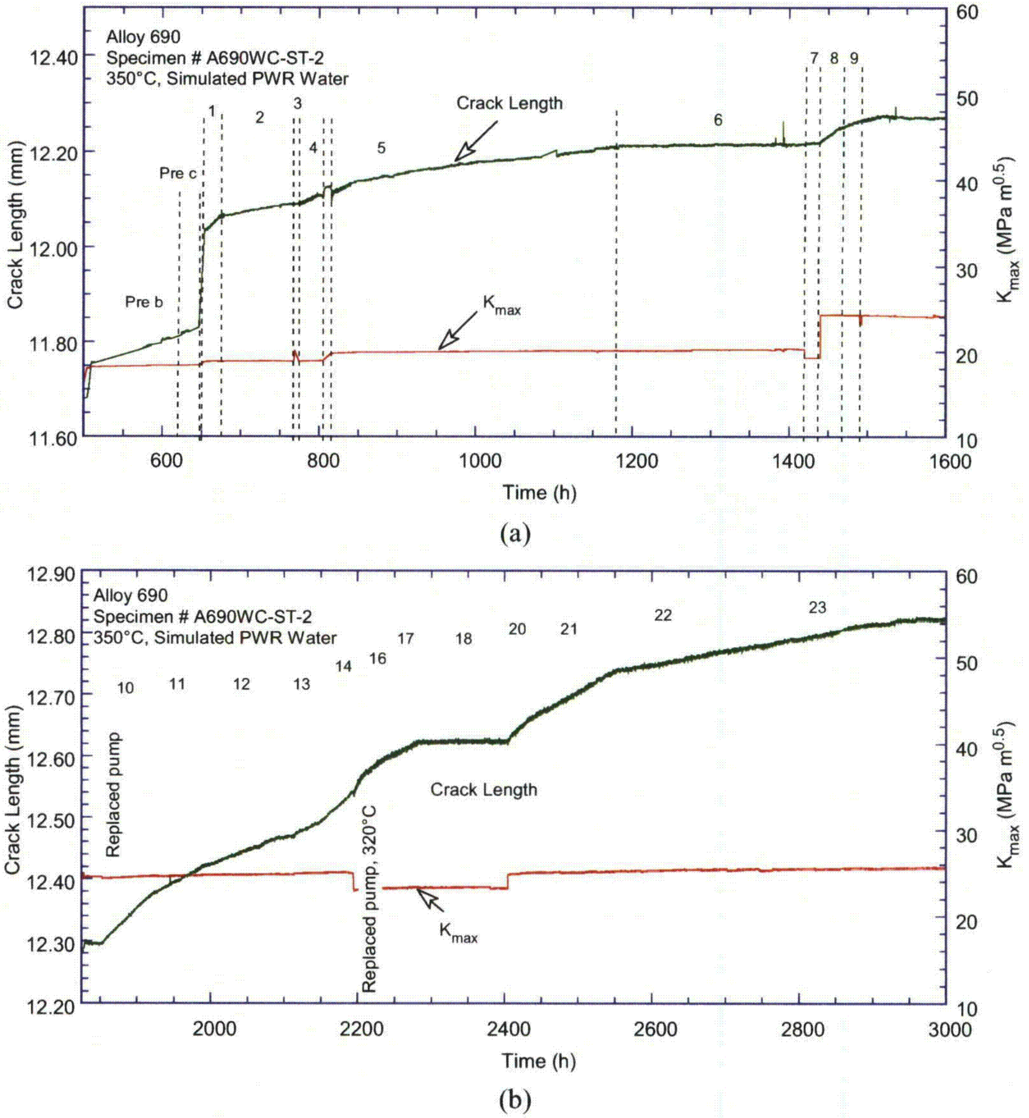

(a)

(b)

Figure 47. **Crack length vs. time for Alloy 690 Specimen A690WC-ST-2 in simulated PWR environment during test periods (a) precracking-9, (b) 10-23, and (c) 24-27.**

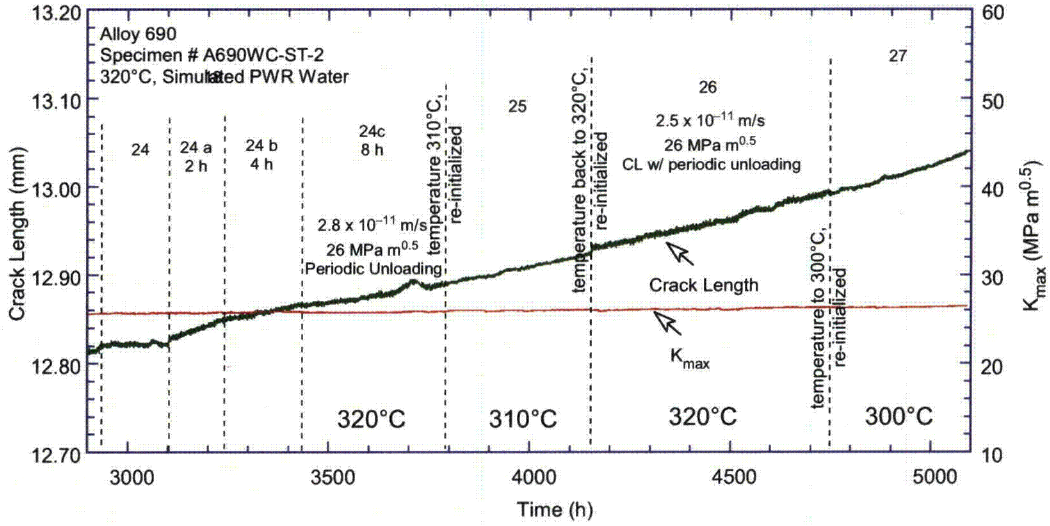

(c)

Figure 47. (cont.)

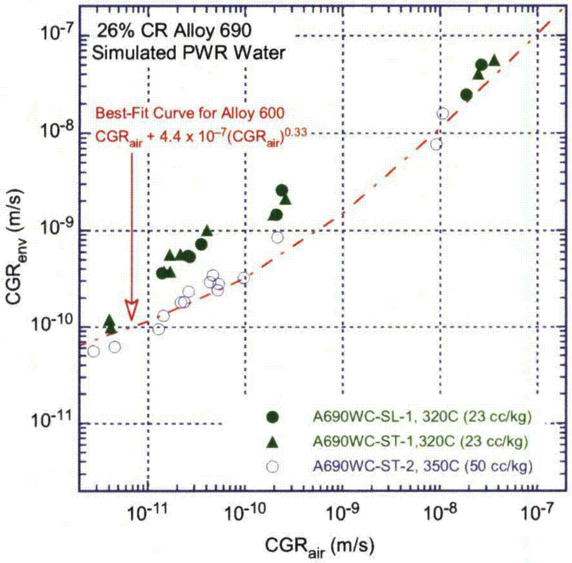

Figure 48.
Cyclic CGR data for Alloy 690 Specimen A690WC-ST-2 at 350°C (662°F) and for previous two specimens under similar conditions in PWR environment at 320°C (608°F).

The resulting fracture surface was examined by SEM (Fig. 49). The image indicates that the testing procedure resulted in a straight, uniform fracture surface. Two fracture modes – corresponding to mechanical fatigue and SCC – can be distinguished. The image shown in Fig. 49 was used to determine the correction factors for the DC potential data. In this case, the DC potential method underestimated the crack advance by 14%. The good agreement is not surprising as a cycling component was almost always present.

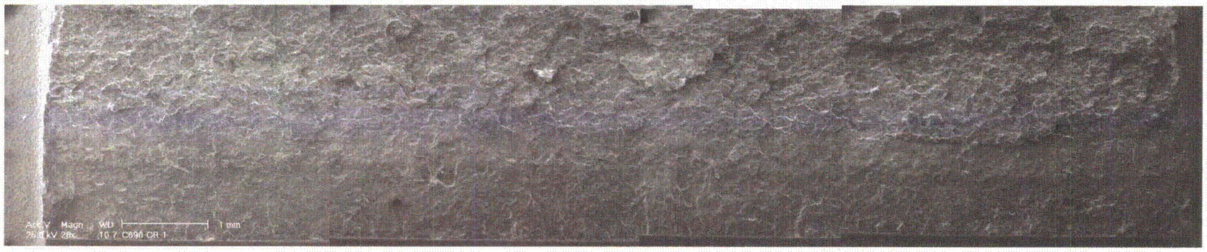

Figure 49. Fracture surface of specimen A690WC-ST-2. Crack advance is from bottom to top.

Figure 50 illustrates the fracture modes observed. Figure 50a shows a region of the fracture surface with both TG and IG fracture modes. Figures 50b and 50c focus on the transition area from TG to IG, which is marked with arrows in the figures. Unlike previous specimens where elements of IG (smooth facets, IG cracks, etc.) were found on the fracture surface in the TG region (see, for example, Fig. 41), the current specimen appears to show a more abrupt transition from a predominantly TG fracture mode. Note that the fracture mode started to change to IG after approximately 1 mm (0.04 in.), i.e., after transitioning at 320ºC (608°F). This result further substantiates the earlier observation regarding the low enhancement of the cyclic rates at 350ºC (662°F), as shown in Fig. 48.

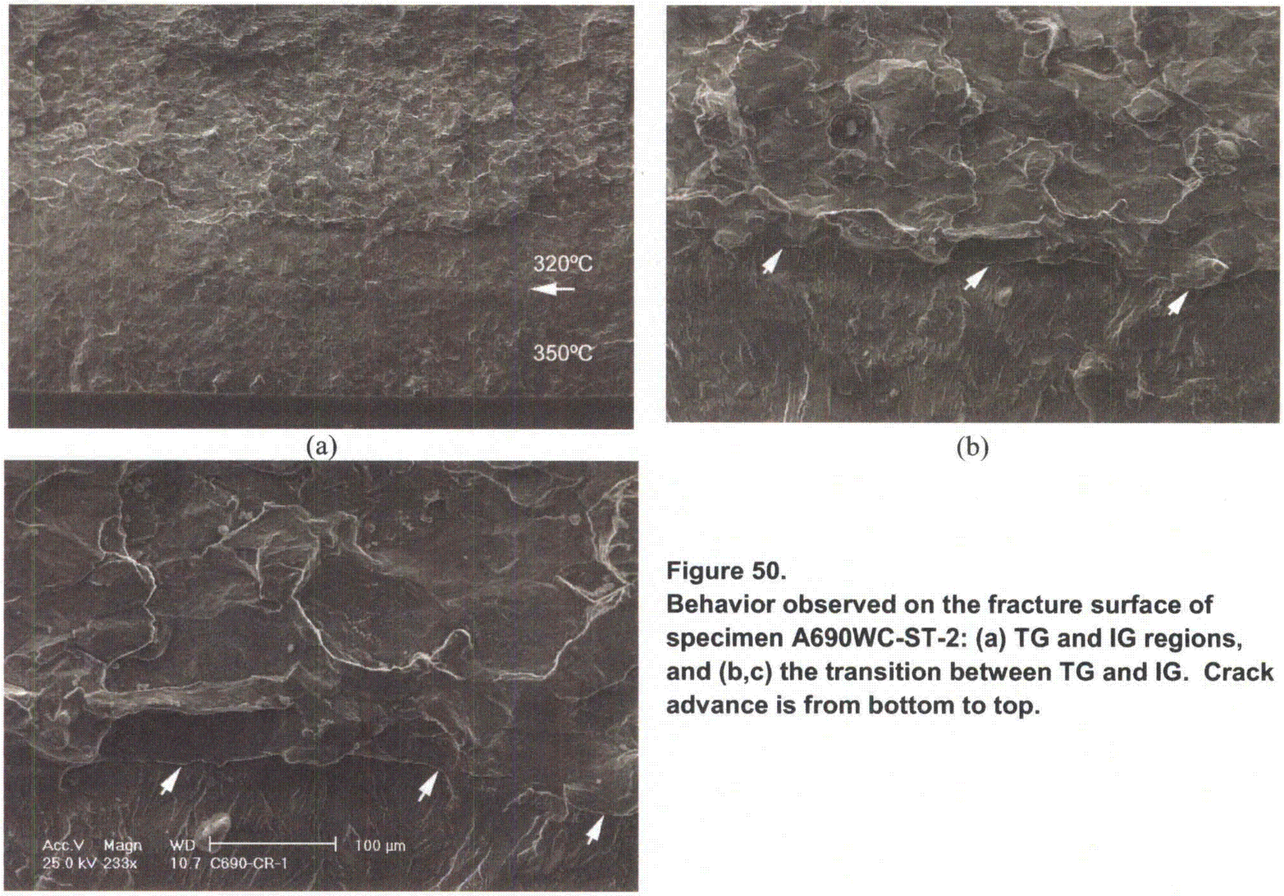

(a) (b) (c)

Figure 50.
Behavior observed on the fracture surface of specimen A690WC-ST-2: (a) TG and IG regions, and (b,c) the transition between TG and IG. Crack advance is from bottom to top.

4.3 Crack Growth Data for Alloy 690 in As-received Condition

Two CGR tests in the simulated PWR environment were completed on as-received Alloy 690. These tests were conducted on ½-T CT specimens designated C690-CR-1 and C690-LR-2.

4.3.1 Specimen C690-CR-1

The test conditions for Specimen A690WC-SL-1 are given in Table 13, and the changes in crack length and K_{max} with time are shown in Fig. 51. The first measured SCC CGR at constant load (period 5 in Table 13) was approximately 5 x 10^{-12} m/s for K_{max} = 24.9 MPa·$m^{1/2}$ (22.7 ksi·$in.^{1/2}$). After introducing a periodic unloading component, the estimated SCC CGRs were found to be similar to that at pure constant load, on average ≈ 5 x 10^{-12} m/s. Also, in period 9 the CGR_{air} component was about an order of magnitude smaller than the measured CGR in the test environment; thus, one can safely assume that the measured CGR is entirely due to SCC. Finally, the specimen was set at constant load one more time to reconfirm the 10^{-12} m/s rate.

Table 13. Crack growth data for specimen C690-CR-1 of Alloy 690 in PWR water.[a]

Test Period	Test Time, h	Temp., °C	Load Ratio R	Rise Time, s	Down Time, s	Hold Time, s	K_{max}, MPa·$m^{1/2}$	ΔK, MPa·$m^{1/2}$	CGR_{env}, m/s	Estimated CGR_{air}, m/s	Crack Length, mm
Pre a	33	321.2	0.30	1	1	0	23.2	16.2	9.06E-09	2.01E-08	11.716
Pre b	48	321.2	0.30	100	100	0	23.3	16.3	3.14E-10	2.03E-10	11.723
Pre c	50	321.2	0.30	0.5	0.5	0	23.5	16.4	1.60E-08	4.20E-08	11.756
Pre d	53	321.2	0.30	2	2	0	23.6	16.5	8.38E-09	1.07E-08	11.808
Pre e	57	321.2	0.30	5	5	0	23.6	16.5	5.40E-09	4.26E-09	11.844
1	80	321.2	0.48	50	12	0	23.6	12.3	4.61E-10	2.06E-10	11.855
2	195	321.1	0.48	300	12	0	24.0	12.5	1.17E-10	3.65E-11	11.935
3	313	321.1	0.49	600	12	0	24.1	12.3	7.63E-11	1.78E-11	11.969
4	480	321.8	0.48	1000	12	0	24.3	12.6	4.25E-11	1.16E-11	11.993
5	1,681	320.7	1	-	-	0	24.9	0.0	5.40E-12	-	12.027
6	2,568	321.2	0.48	1000	12	7200	21.5	11.2	8.87E-12	8.48E-13	11.054
7	2,882	321.4	1[b]	-	-	0	25.6	13.3	1.72E-11	-	12.088
8	3,340	321.3	1[c]	-	-	0	25.6	13.3	9.36E-12	-	12.101
9	3,912	321.5	1[d]	-	-	0	24.8	12.9	5.50E-12	-	12.111
10	4,678	320.0	1	-	-	0	24.5	0.0	1.26E-12	-	12.118

[a] Simulated PWR water with 2 ppm Li, 1000 ppm B, DO <10 ppb. Conductivity was 21 ± 3 μS/cm, and pH 6.4.

[b] Includes periodic unloading by 50% (12 s/12 s) every 2 h.

[c] Includes periodic unloading by 50% (12 s/12 s) every 4 h.

[d] Includes periodic unloading by 50% (12 s/12 s) every 8 h.

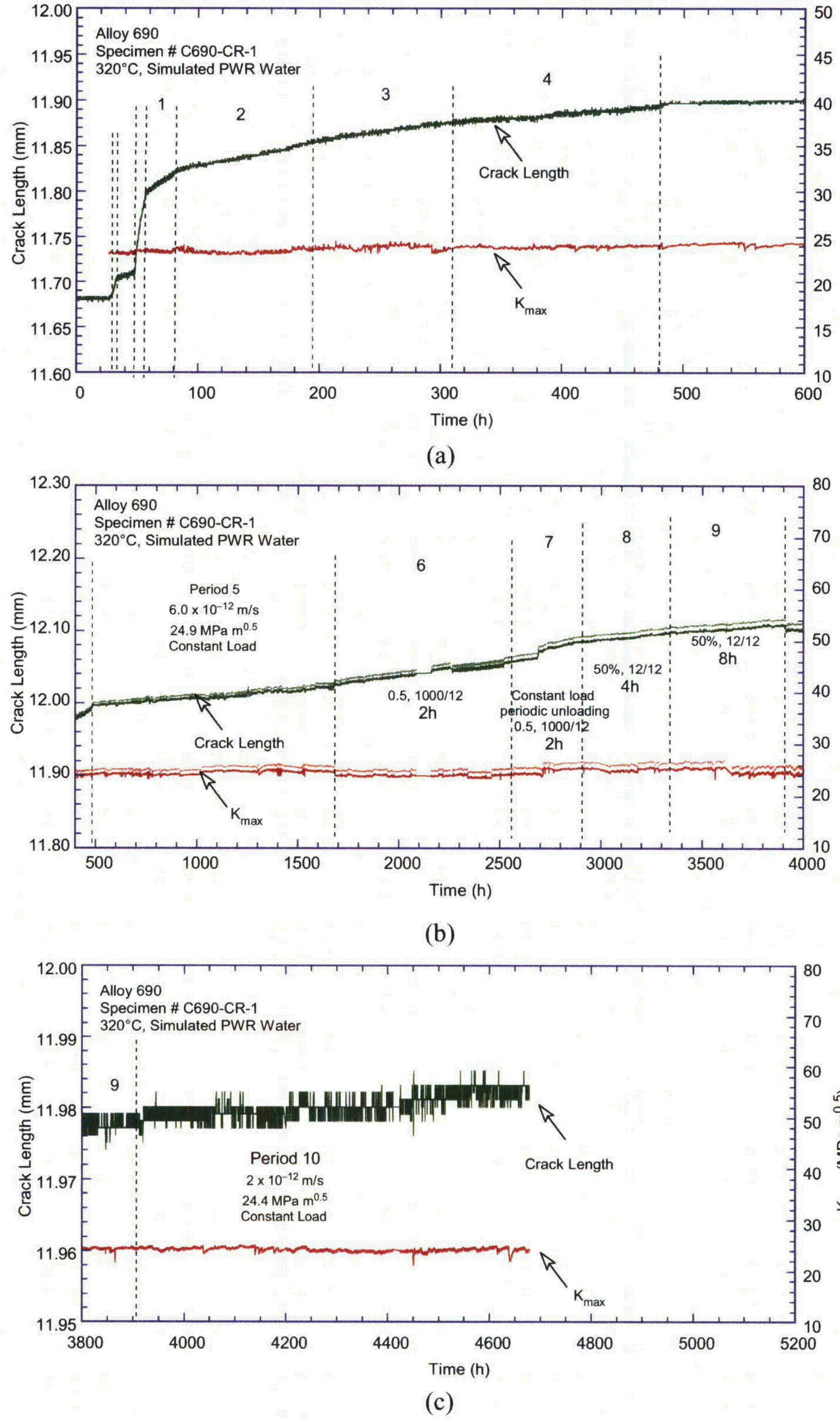

(a)

(b)

(c)

Figure 51. Crack length vs. time for Alloy 690 specimen C690-CR-1 in simulated PWR environment during test periods (a) precracking-4, (b) 5-9, and (c) 10.

The resulting fracture surface was examined by SEM. Figure 52 shows a small region of the fracture surface, and Fig. 53 shows the full fracture surface of the specimen, broken into two halves. The images indicate that the testing procedure resulted in a straight, uniform fracture surface. The full fracture surface, shown in Fig. 53, was used to determine the correction factors for the DC potential data. The correction was small (4%) as a cycling component was almost always present, and growth under constant load was limited.

Figure 52 shows that the fracture mode appears to be predominantly TG for the entire test. However, as the transitioning ends (approximately halfway through the test), the fracture surface appears to become smooth. This and other features were examined in detail, and will be discussed next.

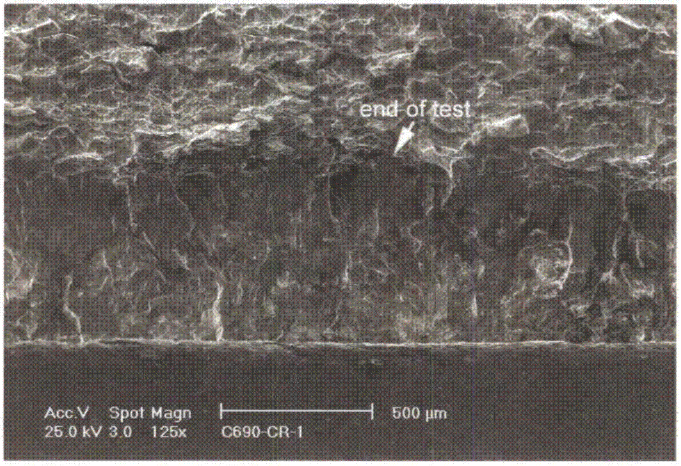

Figure 52.
Region of fracture surface of specimen C690-CR-1. Crack advance is from bottom to top.

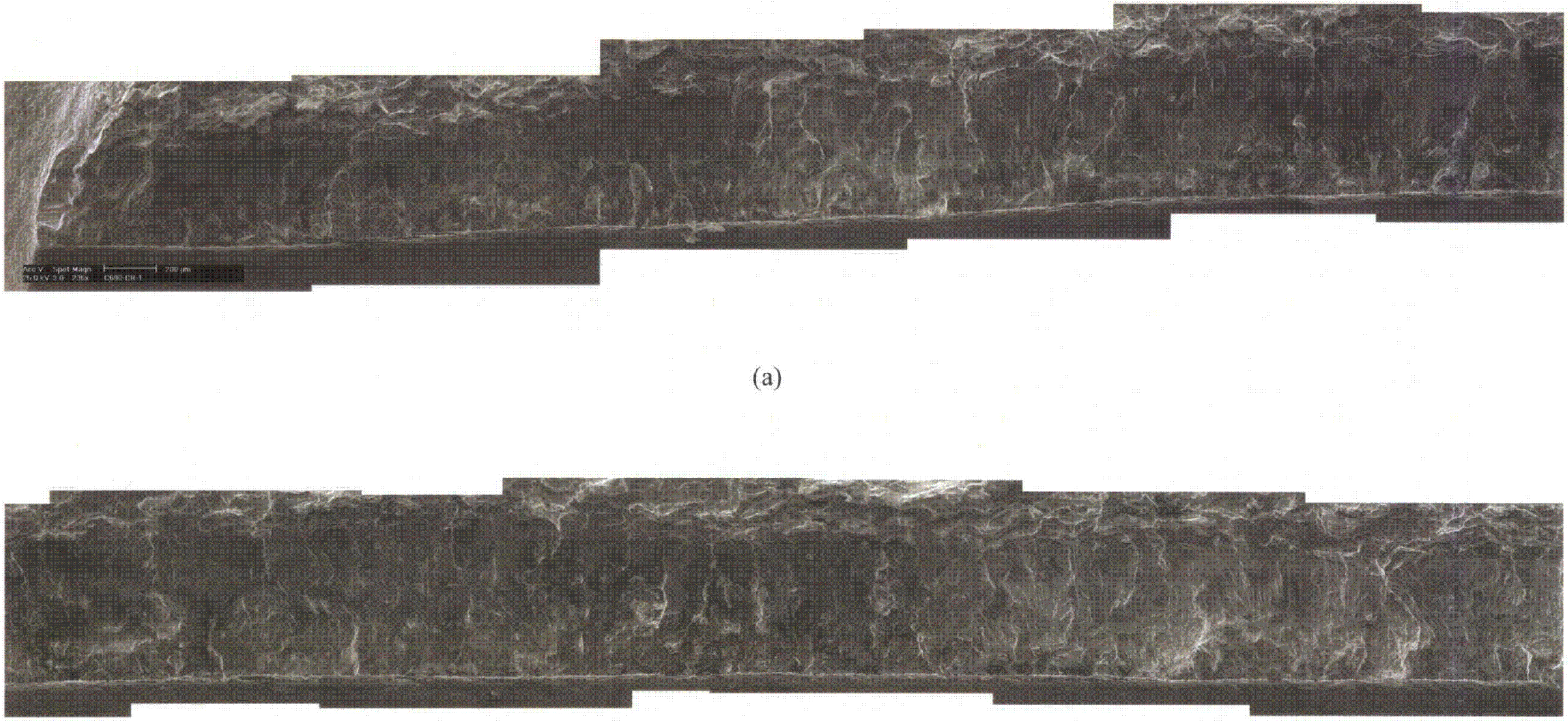

(a)

(b)

Figure 53. Fracture surface of specimen C690-CR-1: (a) first half and (b) second half.

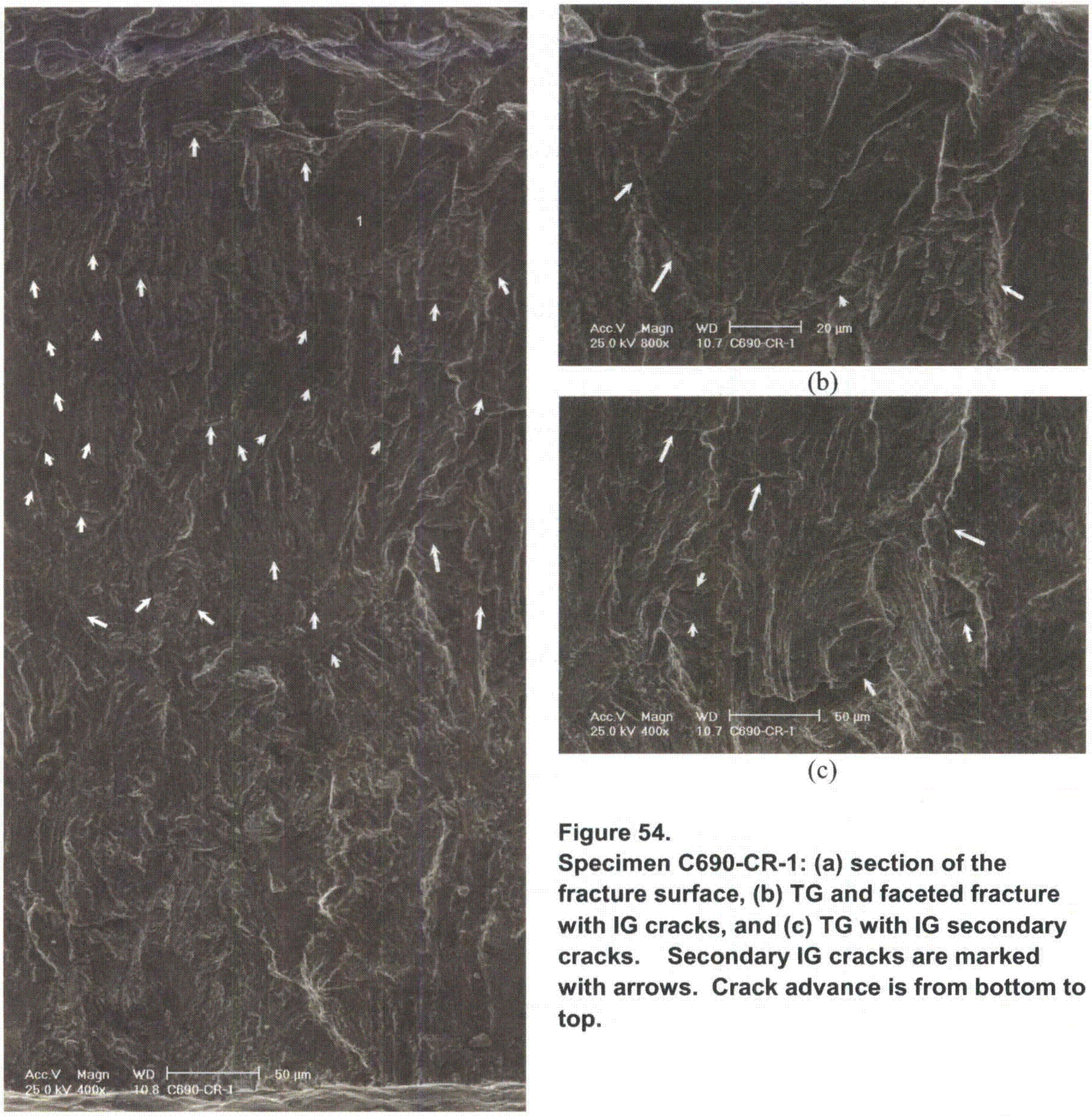

(a)

(b)

(c)

Figure 54.
Specimen C690-CR-1: (a) section of the fracture surface, (b) TG and faceted fracture with IG cracks, and (c) TG with IG secondary cracks. Secondary IG cracks are marked with arrows. Crack advance is from bottom to top.

Figure 54 shows an additional set of micrographs from the fracture surface of specimen C690-CR-1 at higher magnification. Figure 54a shows a section of the fracture surface of specimen C690-CR-1, and as the transitioning ends (approximately halfway through the test), the fracture surface appears to become faceted and smooth in appearance. Secondary IG cracks are also present in the second part of the test, and several are identified by arrows in the figure. Figure 54b shows a region near the end of the test, again with IG cracks and smooth facets visible. Figures 54c is a micrograph from the TG region where secondary IG cracks begin to develop.

In support of the previous observation, Fig. 55 shows pairs of low and high magnification micrographs taken near the end of the test. Areas with smooth facets and IG secondary cracks are visible. Figure 56 shows additional examples of areas with smooth facets and IG secondary cracks on the fracture surface of specimen C690-CR-1.

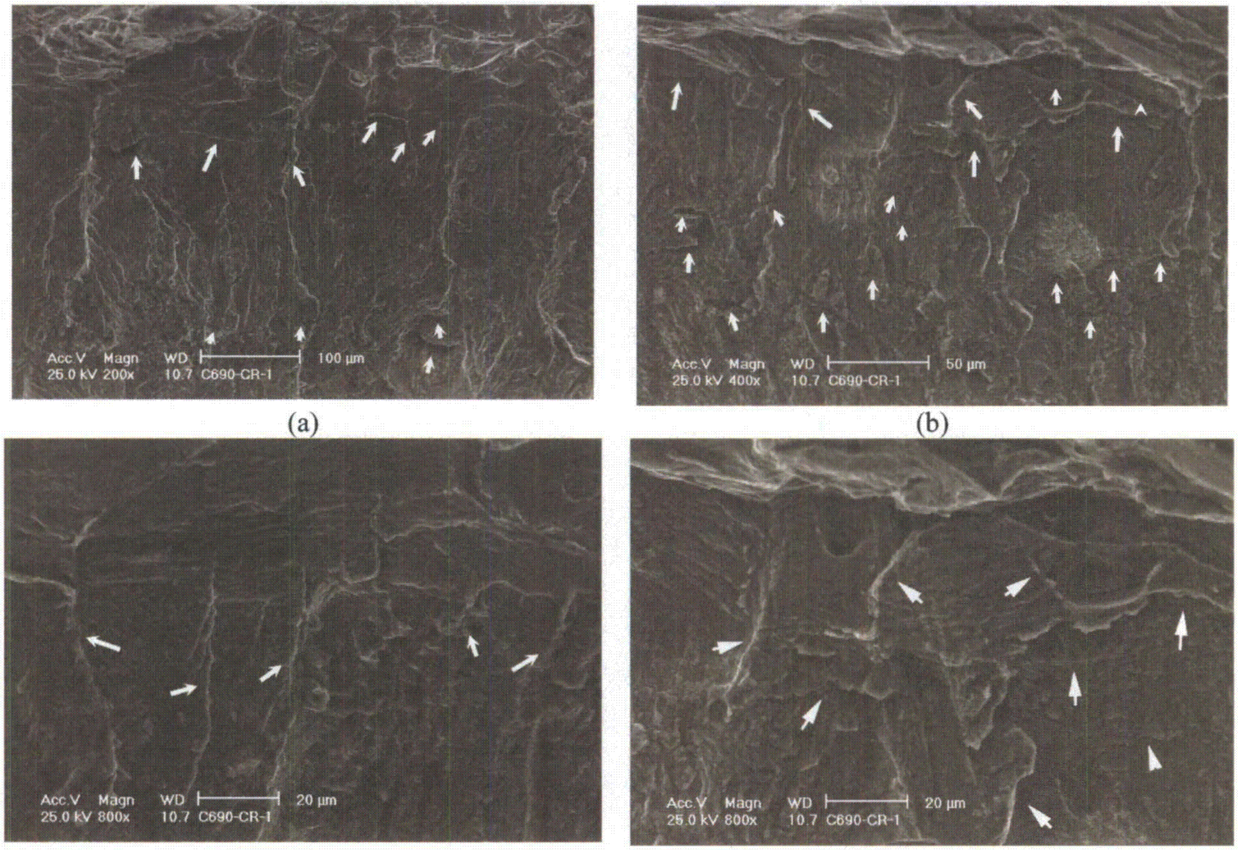

(a) (b)

(c) (d)

Figure 55. Fracture surface of specimen C690-CR-1: (a,b) regions near the end of the test, and (c,d) higher magnification micrographs showing the same areas, with smooth facets and IG secondary cracks. Secondary IG cracks are identified with arrows. Crack advance is from bottom to top.

In summary, the fracture surface of specimen C690-CR-1 did not show the smooth IG fracture mode characteristic of fast propagating SCC cracks. Secondary IG cracking on the fracture surface was extensive. Occasionally, those were accompanied by smooth facets.

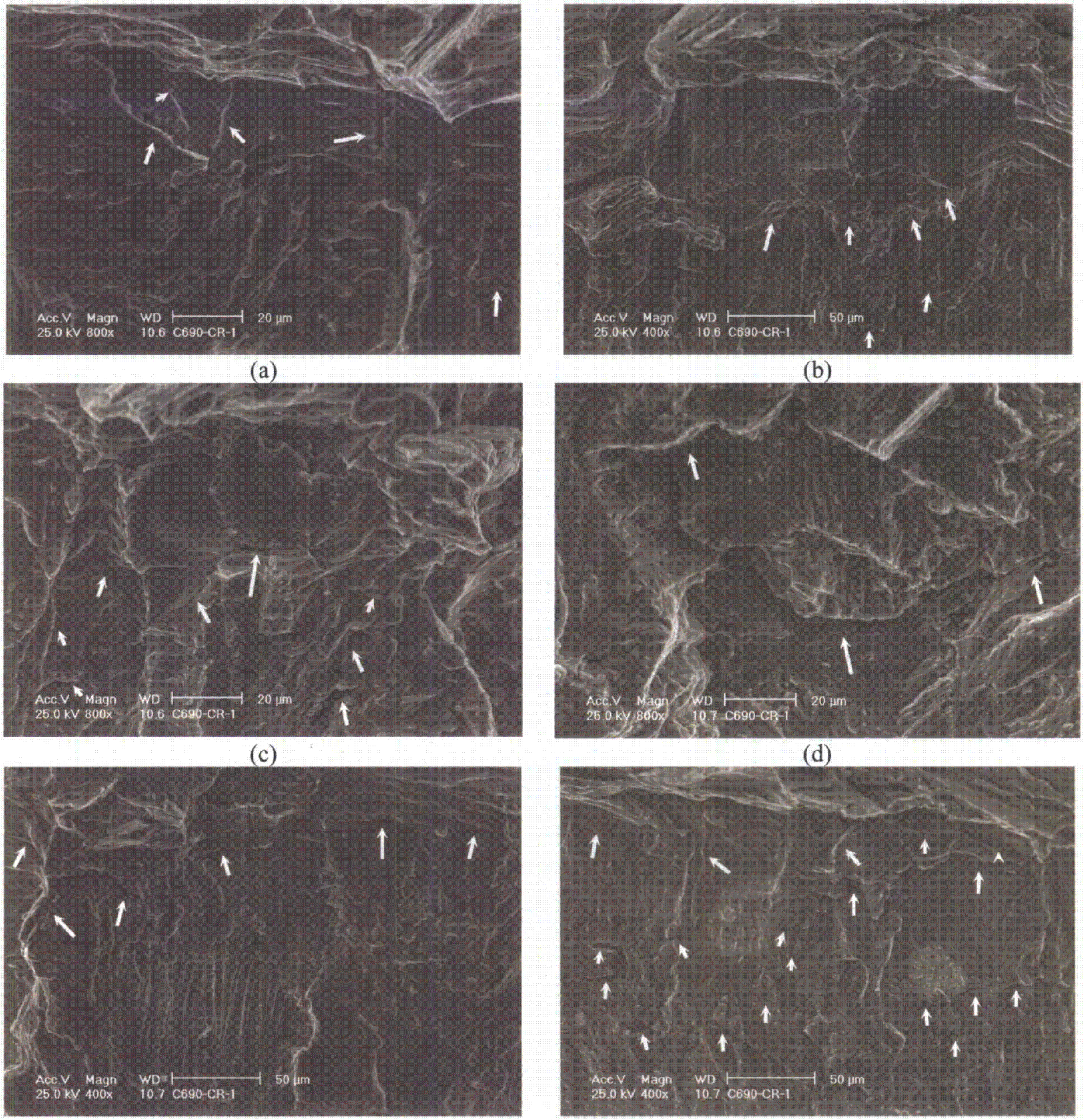

(a) (b)

(c) (d)

(e) (f)

Figure 56. Examples of areas with smooth facets and IG secondary cracks on the fracture surface of specimen C690-CR-1. Crack advance is from bottom to top.

4.3.2 Specimen C690-LR-2

The test on specimen C690-LR-2 complements that on specimen C690-CR-1, but in a different orientation. The objective was twofold. First, the SCC CGR at 320°C was needed in order to determine the effect of orientation. Second, once steady-state SCC was established, the temperature was increased to 350°C (662°F) in an attempt to determine the activation energy for SCC crack growth in Alloy 690. The premise was that if the SCC CGR for this specimen was comparable to that of C690-CR-1, then an activation energy close to that for Alloy 600 (130 kJ/mol) would cause the SCC CGR at 350°C (662°F) to be in the low-10^{-11} m/s range. To further facilitate SCC, the hydrogen concentration was maintained at 23 cc/kg, that is, close to a value that makes the specimen potential close to that for the Ni/NiO transition (Table 6). The testing conditions are given in Table 14, and the changes in crack length and K_{max} with time are shown in Fig. 57.

Table 14. Crack growth data for specimen C690-LR-2 of Alloy 690 in PWR water.[a]

Test Period	Test Time, h	Temp., °C	Load Ratio R	Rise Time, s	Down Time, s	Hold Time, s	K_{max}, MPa·m$^{1/2}$	ΔK, MPa·m$^{1/2}$	CGR_{env}, m/s	Estimated CGR_{air}, m/s	Crack Length, mm
Pre a	79	321.5	0.29	5	5	0	18.3	13.0	3.81E-10	1.59E-09	11.614
Pre b	94	321.5	0.29	50	50	0	18.3	13.0	6.14E-12	1.58E-10	11.616
Pre c	102	321.6	0.29	5	5	0	18.3	13.0	1.42E-11	1.58E-09	11.618
Pre d	118	321.6	0.29	50	50	0	18.3	13.0	6.04E-11	1.58E-10	11.616
Pre e	126	321.8	0.29	1	1	0	18.3	13.0	1.19E-09	7.89E-09	11.631
Pre f	194	321.8	0.29	50	50	0	18.3	13.0	6.74E-11	1.58E-10	11.639
Pre g	199	321.9	0.29	1	1	0	18.4	13.0	2.44E-09	7.98E-09	11.662
Pre h	215	321.6	0.29	50	50	0	18.4	13.1	1.32E-10	1.60E-10	11.667
Pre i	222	321.9	0.30	1	1	0	18.6	13.0	4.00E-09	8.05E-09	11.717
Pre j	239	321.5	0.30	50	50	0	18.6	13.0	1.90E-10	1.62E-10	11.728
Pre k	248	321.6	0.30	1	1	0	18.8	13.2	6.76E-09	8.53E-09	11.833
Pre l	263	321.5	0.30	50	50	0	18.9	13.2	3.35E-10	1.72E-10	11.845
Pre m	272	321.6	0.29	1	1	0	19.3	13.7	1.00E-08	9.70E-09	12.003
Pre n	287	321.6	0.30	50	50	0	19.3	13.5	5.15E-10	1.88E-10	12.017
Pre o	293	321.6	0.30	1	1	0	19.6	13.7	1.36E-08	1.01E-08	12.173
Pre p	359	321.6	0.29	50	50	0	19.8	14.1	6.86E-10	2.18E-10	12.258
Pre q	367	321.8	0.29	1	1	0	20.5	14.5	1.71E-08	1.24E-08	12.489
Pre r	383	321.8	0.29	50	50	0	20.5	14.6	9.15E-10	2.51E-10	12.519
Pre s	386	321.9	0.30	1	1	0	20.9	14.6	2.06E-08	1.30E-08	12.631
1	391	321.9	0.49	50	12	0	20.9	10.7	5.62E-10	1.20E-10	12.641
2	450	321.7	0.49	300	12	0	21.0	10.7	1.14E-10	2.01E-11	12.663
3	507	322.1	0.49	600	12	0	21.0	10.7	5.09E-10	1.01E-11	12.692
4	559	322.0	0.49	1000	12	0	21.1	10.8	3.45E-11	6.21E-12	12.694
5	1,125	319.7	0.49	1000	12	14,400	21.2	10.8	5.95E-12	4.06E-13	12.724
6	1,411	321.4	1	0	0	0	21.3	0.0	3.78E-12	-	12.728
7	2,013	350.3	1	0	0	0	21.2	0.0	8.0E-12	-	12.731
8	3,726	349.8	0.48	1000	12	14,400	21.5	11.2	8.19E-12	5.53E-13	12.775

[a] Simulated PWR water with 2 ppm Li, 1100 ppm B, DO <10 ppb. Conductivity was 21 ± 3 μS/cm, and pH 6.4.

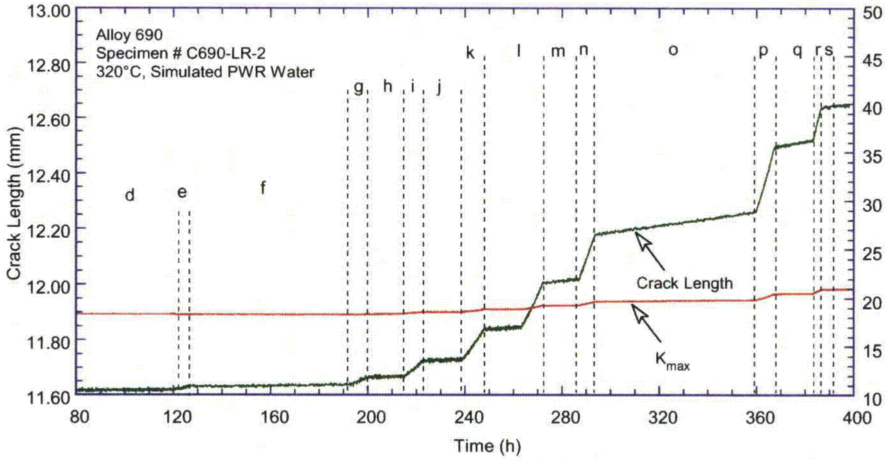

(a)

Figure 57. Crack length vs. time for Alloy 690 Specimen C690-LR-2 in simulated PWR environment during test periods (a) precracking, (b) 1-5, and (c) 6-8.

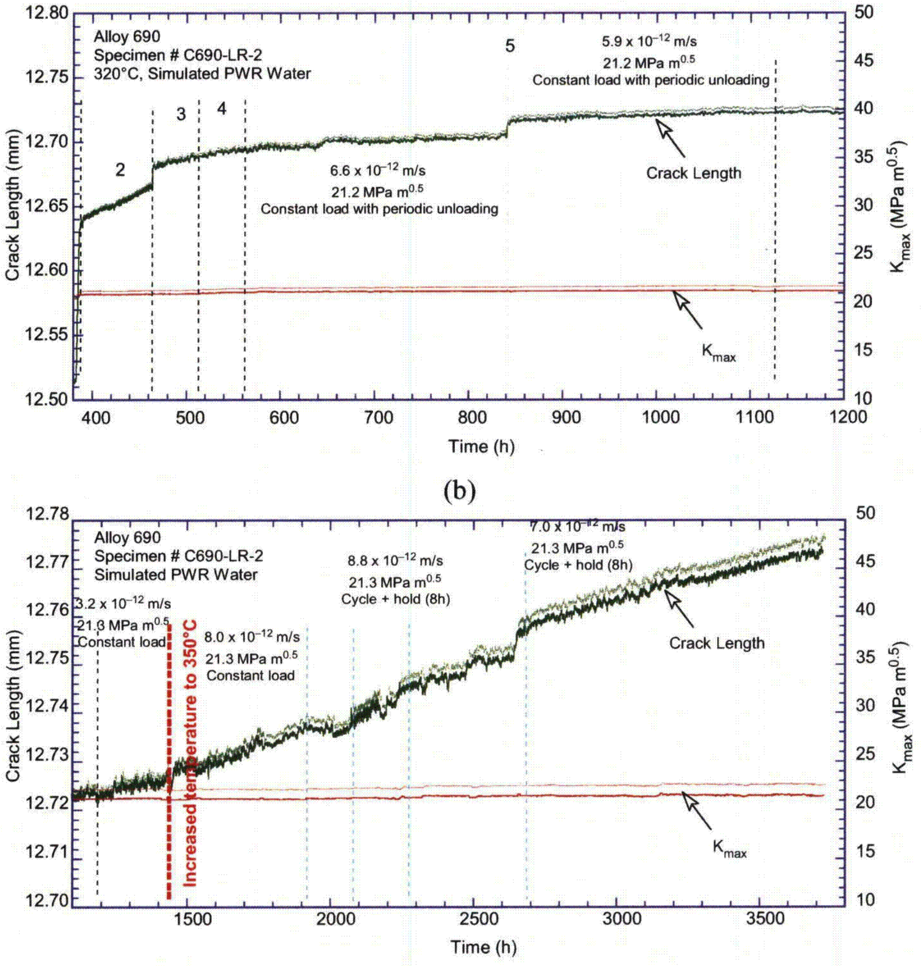

(b)

(c)

Figure 57. **(cont.)**

The SCC CGRs were determined during both cycle + hold and constant-load conditions. For example, period 5 (Table 14, Fig. 57b) consists of a cycle + hold, with a hold time of 4 h. The resulting rates (5.9-6.6 x 10^{-12} m/s) are in good agreement with those obtained on the previous specimen in the as-received condition. Since the mechanical contribution due to cycling is approximately an order of magnitude lower than the measured rate, the measured crack growth rates are due to SCC. Next, the periodic unloading was removed in period 6, and the SCC CGR measured at constant load was 3.8 x 10^{-12} m/s, again, consistent with previous observations. After approximately 200 h, the temperature was increased to 350ºC (662ºF). The SCC CGR rate at constant load increased to 8.0 x 10^{-12} m/s, then apparently stalled. Cycle + hold (8 h) was introduced in an attempt to reactivate the crack, and a similar CGR of 8.8 x 10^{-12} m/s was measured. The rate appeared to decrease again, followed by another increase to 7.0 x 10^{-12} m/s. While the rates seem consistent with each other, the cause for this occasional stalling is unknown. Nevertheless, the SCC CGR rate in this as-received alloy appears to respond to temperature changes, although not to the extent expected based on Alloy 600 experience.

The resulting fracture surface was examined by SEM. One observation was that the fracture surface was covered with oxide filaments (Fig. 58). Such oxides have been observed previously by Mintz and Devine during corrosion tests of Alloy 600 in the vicinity of the Ni/NiO line.[41] Figure 59 shows the full fracture surface of the specimen, imaged such that there is a contrast between the oxides and the metal surface. This image was used to determine the correction factors for the DC potential data. The correction was small, 10%, although not as small as that for specimen C690-CR-1, and was probably a reflection of the fracture surface not being as straight. Nevertheless, in both cases the fact that a cycling component was almost always present helped with DC potential accuracy.

Figure 59 shows that the fracture mode appears to be predominantly TG for the entire test. However, features similar to those observed on the fracture surface of specimen C690-CR-1 were observed, and these will be discussed next.

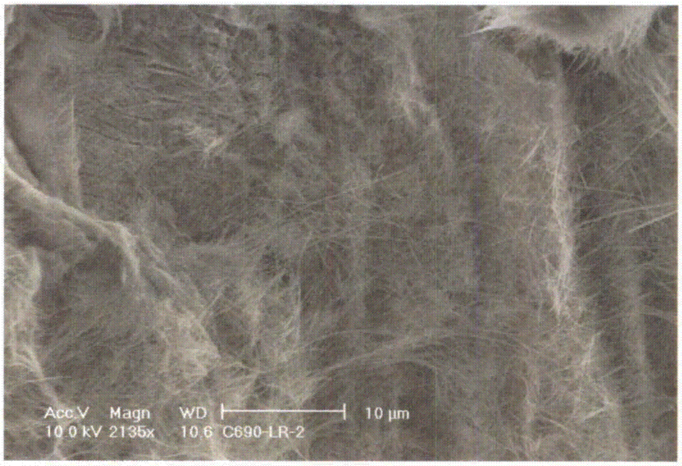

Figure 58.
Oxides on the fracture surface of Specimen C690-LR-2.

Figure 59. Fracture surface of specimen C690-LR-2. Crack advance is from bottom to top.

Figure 60 shows micrographs from the fracture surface of specimen C690-LR-2. As with the previous specimen, the surface has secondary IG cracks, which are identified by arrows in the figure. Occasional smooth facets are also visible.

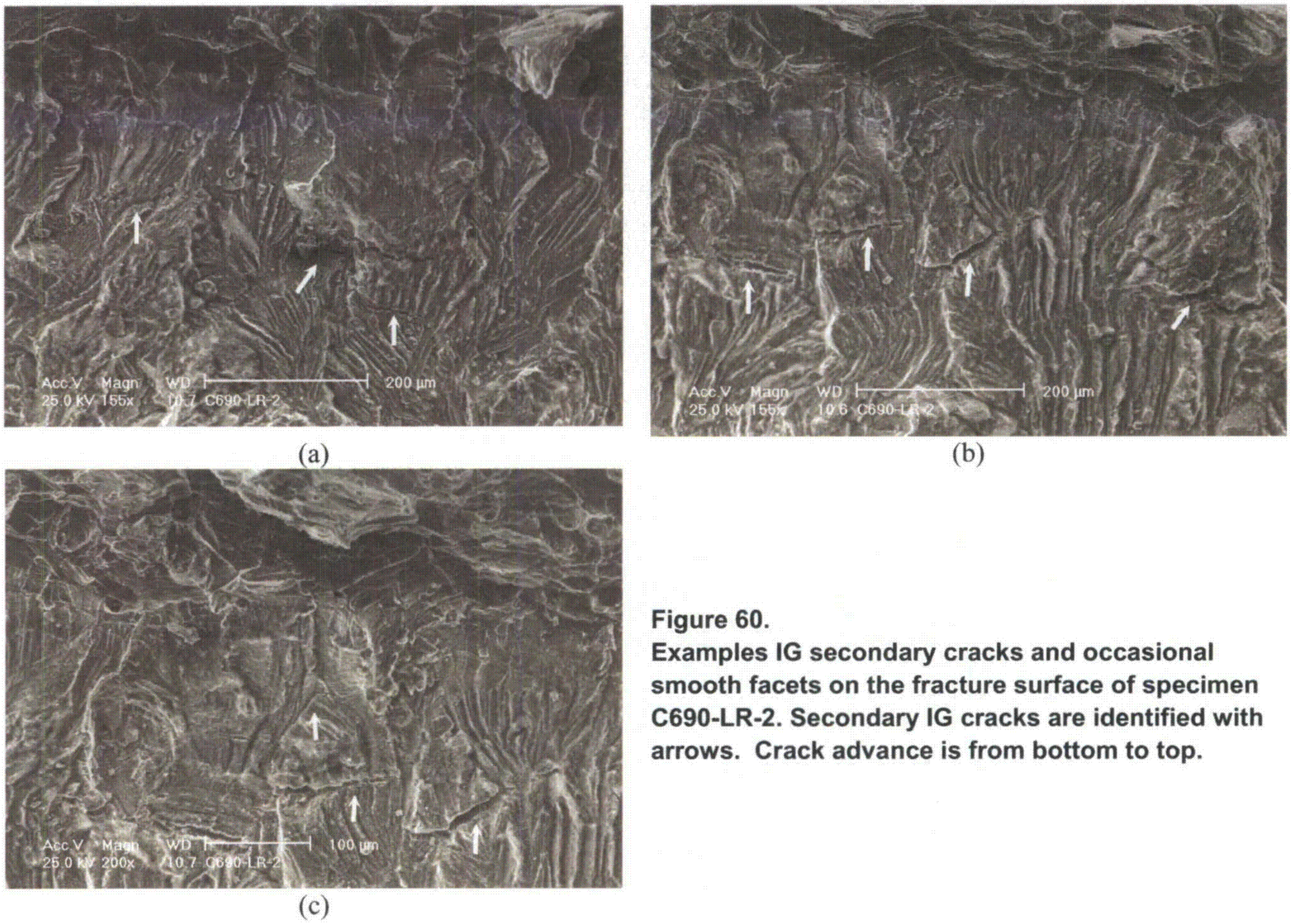

Figure 60.
Examples IG secondary cracks and occasional smooth facets on the fracture surface of specimen C690-LR-2. Secondary IG cracks are identified with arrows. Crack advance is from bottom to top.

Figure 61 shows additional examples of secondary cracking 50-70 µm from the crack front at the end of the test. By comparison with the seemingly isolated cracks observed on the fracture surface of specimen C690-CR-1 (see, for example, Fig. 55), the cracks here are extensive and may be due to the increased test temperature during the portion of the test when this cracking occurred.

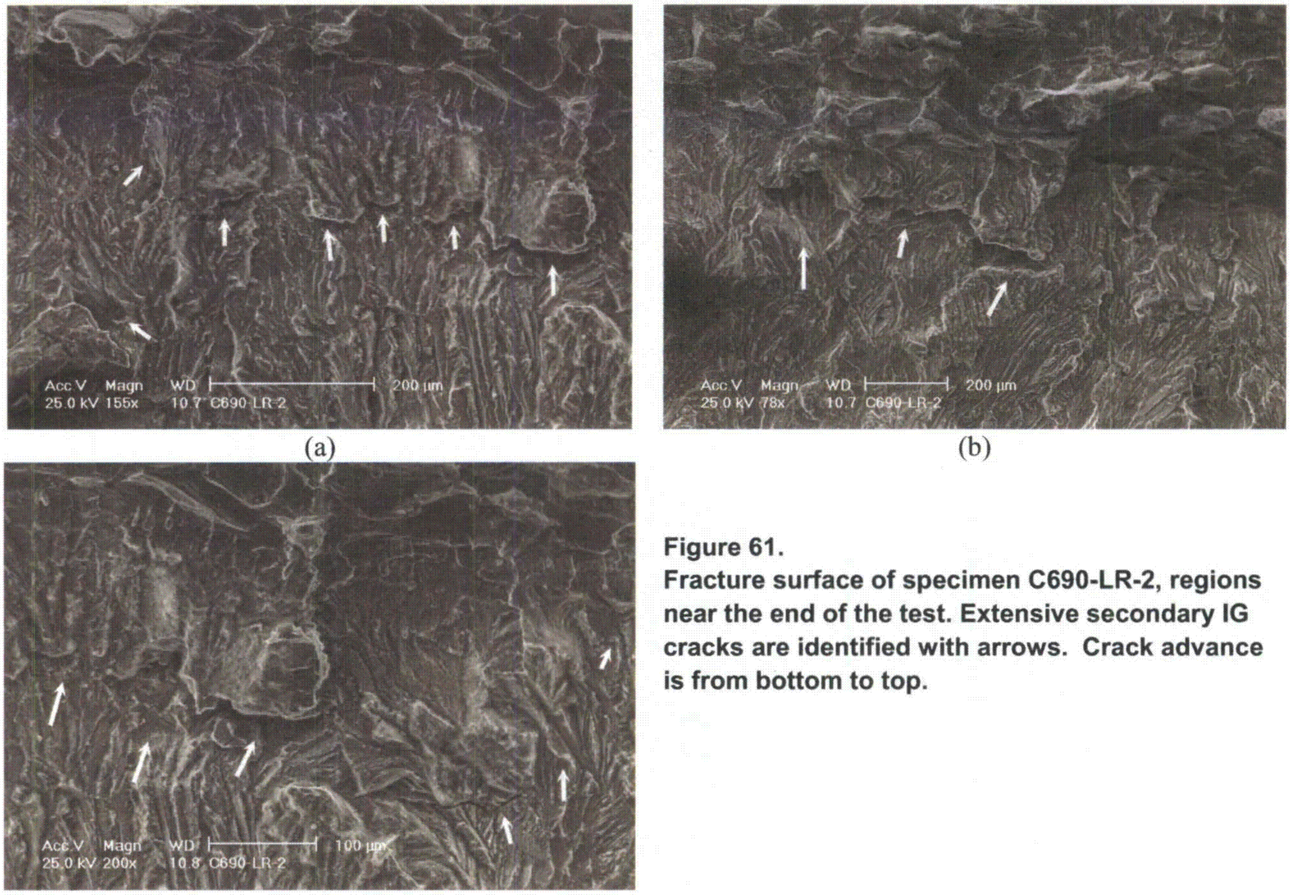

(a) (b) (c)

Figure 61.
Fracture surface of specimen C690-LR-2, regions near the end of the test. Extensive secondary IG cracks are identified with arrows. Crack advance is from bottom to top.

Finally, Fig. 62 provides additional examples of areas with smooth facets and IG secondary cracks on the fracture surface of specimen C690-LR-2. At these magnifications, several facets indicate striations consistent with the cycle + hold loading (Figs. 62b, 62c, and 62d).

In summary, the fracture surface of specimen C690-LR-2 was similar to that of specimen C690-CR-1, and it did not show the smooth IG fracture mode characteristic of fast propagating SCC cracks. Secondary IG cracking was present, and during the test period at 350°C (662°F), appeared to be more extensive than what was observed on the fracture surface of specimen C690-CR-1. Occasionally, secondary IG cracking was accompanied by smooth facets.

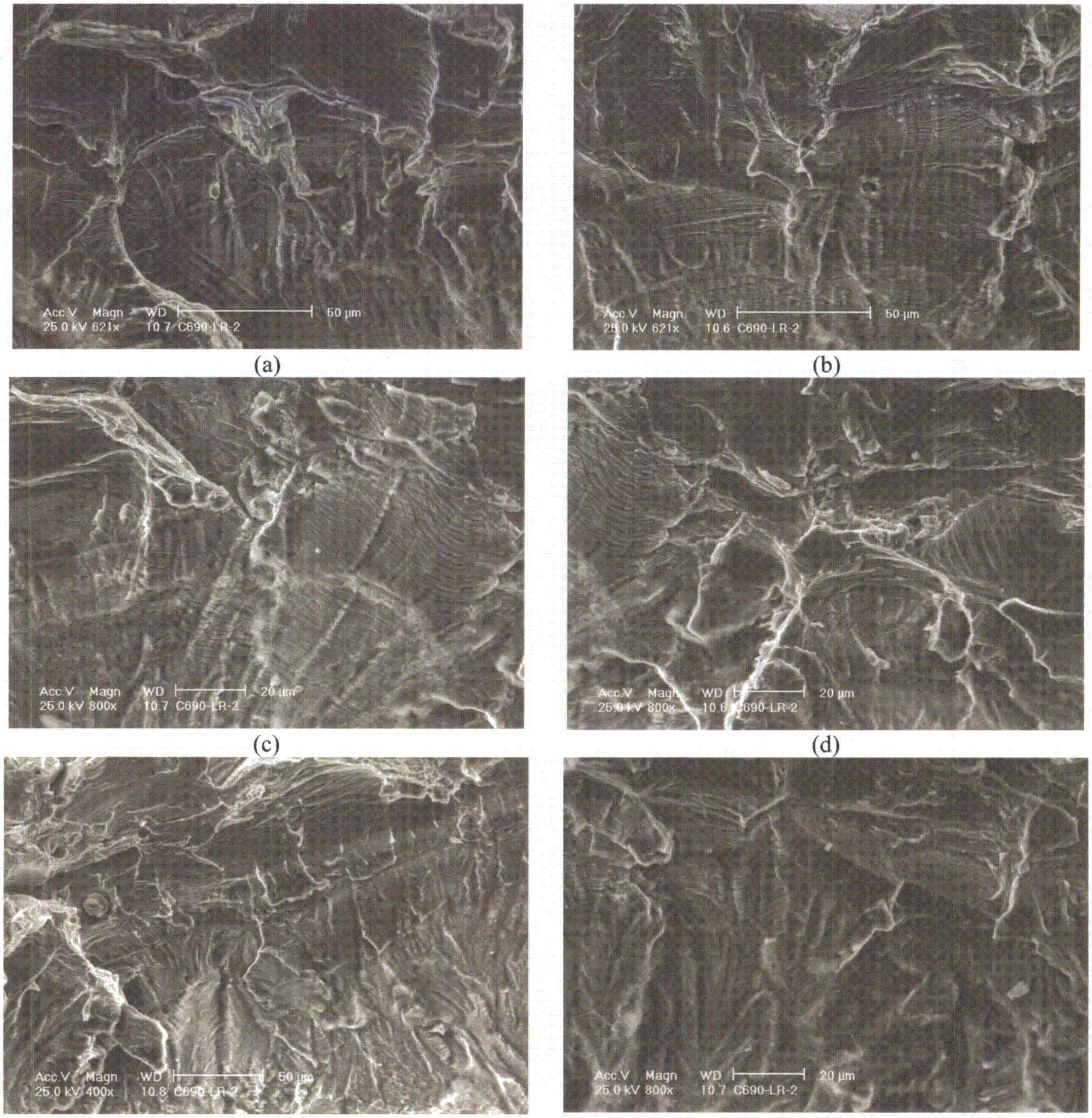

(a) (b)

(c) (d)

(e) (f)

Figure 62. Examples of areas with smooth facets and IG secondary cracks on the fracture surface of specimen C690-LR-2. Crack advance is from bottom to top.

4.4 Crack Growth Data for Alloy 152 Weld

Two CGR tests in simulated PWR environment were completed on Alloy 152 in an as-welded condition. These tests were conducted on 1-T CT specimens designated A152-TS-2 and A152-TS-4.

4.4.1 Specimen A152-TS-2

This test was a "screening" test performed at a time when no other similar data were available, and was conducted at the same time as the test on Alloy 690 cold-rolled by 26% (specimen A690WC-SL-1). The weld specimen orientation was chosen to be TS, along the dendritic grains, as this orientation was expected to be the most susceptible to SCC. Standard transitioning procedures developed for Alloy 182/82 were applied, and no hold times or periodic unloading was used.

The testing conditions for Specimen A152-TS-2 are given in Table 15, and the changes in crack length and K_{max} with time are shown in Fig. 63. Surprisingly, transitioning from TG to IG SCC occurred readily. The measured CGR at constant load was 5.0 x 10^{-11} m/s for $K_{max} = 30.2$ MPa·m$^{1/2}$ (27.5 ksi·in.$^{1/2}$).

Table 15. Crack growth data for specimen A152-TS-2 of Alloy 152 weld in PWR water.[a]

Test Period	Test Time, h	Temp., °C	Load Ratio R	Rise Time, s	Down Time, s	Hold Time, s	K_{max}, MPa·m$^{1/2}$	ΔK, MPa·m$^{1/2}$	CGR_{env}, m/s	Estimated CGR_{air}, m/s	Crack Length, mm
Pre a	48.0	322.5	0.3	1	1	0	20.3	14.2	2.26E-08	2.78E-08	12.683
Pre b	115.0	322.2	0.3	100	100	0	20.3	14.2	6.41E-10	2.82E-10	12.751
Pre c	132.0	322.1	0.3	1	1	0	20.7	14.5	2.83E-08	3.07E-08	13.183
Pre d	134.0	321.9	0.3	10	10	0	21.0	14.7	5.01E-09	3.21E-09	13.333
Pre e	150.0	322.0	0.3	1	1	0	21.9	15.3	4.09E-08	3.81E-08	14.174
Pre f	162.0	321.8	0.3	10	10	0	22.0	15.4	7.07E-09	3.91E-09	14.303
Pre g	172.0	321.9	0.3	1	1	0	22.8	16.0	4.67E-08	4.53E-08	14.999
Pre h	173.0	321.8	0.3	10	10	0	23.0	16.1	7.26E-09	4.69E-09	15.183
Pre i	186.0	321.7	0.3	1	1	0	23.9	16.7	4.92E-08	5.45E-08	15.887
Pre j	194.0	321.7	0.3	10	10	0	24.2	16.9	7.86E-09	5.73E-09	16.115
Pre k	210.0	321.8	0.3	1	1	0	24.8	17.4	6.65E-08	6.42E-08	16.701
1	216.0	321.8	0.5	300	12	0	29.5	14.8	2.85E-10	1.88E-10	16.783
2	384.0	321.8	0.5	600	12	0	29.7	14.8	1.95E-10	9.55E-11	16.847
3	721.0	322.0	0.5	1000	12	0	29.8	14.9	1.54E-10	5.84E-11	17.020
4	1724.0	321.5	1	-	-	0	30.3	0.0	5.07E-11	-	17.336

[a] Simulated PWR water with 2 ppm Li, 1000 ppm B, DO <10 ppb. Conductivity was 21 ± 3 µS/cm, and pH 6.4.

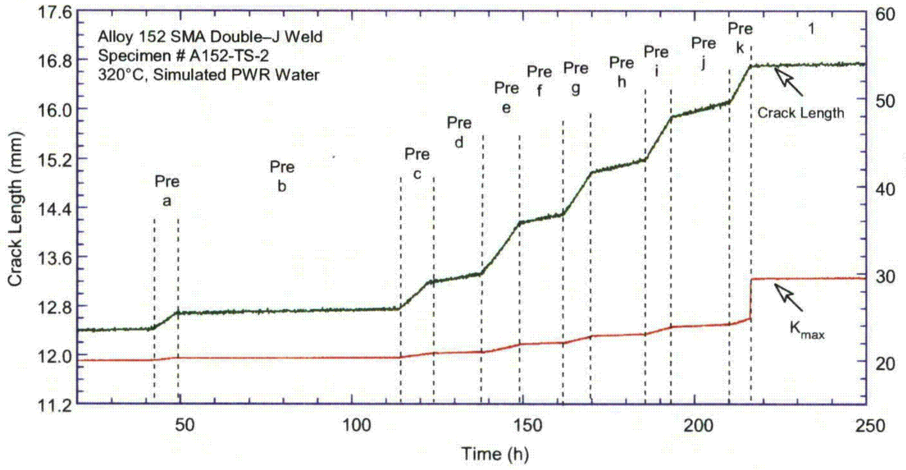

(a)

Figure 63. Crack length vs. time for Alloy 152 weld specimen A152-TS-2 in simulated PWR environment during test periods (a) precracking, (b) 1-3, and (c) 4.

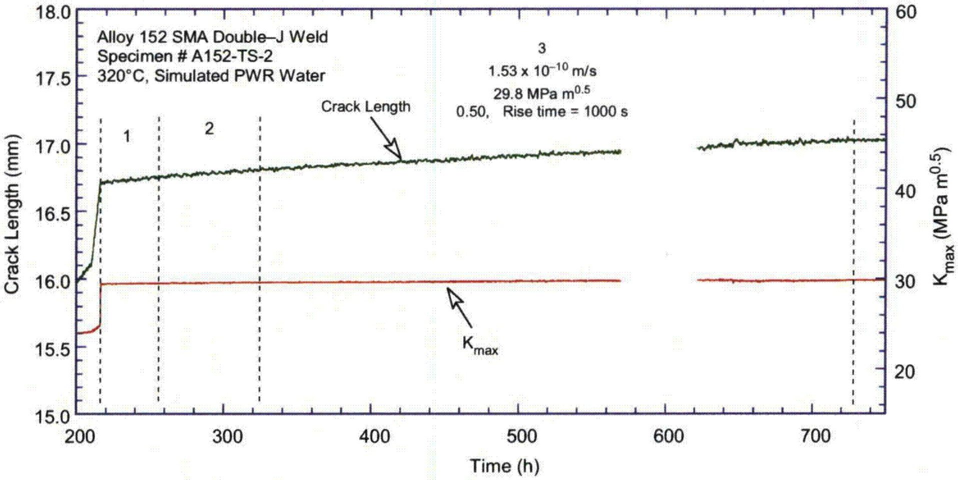

(b)

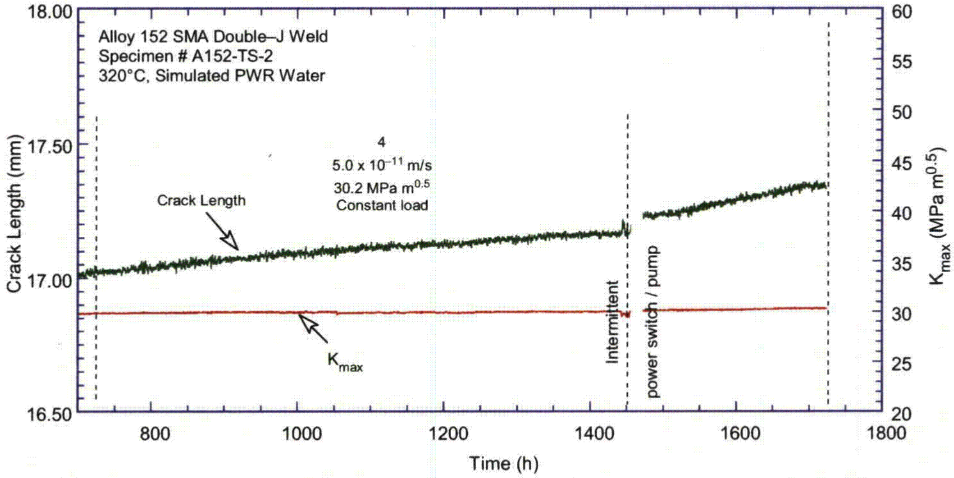

(c)

Figure 63. (cont.)

The SCC CGR [5.0 x 10^{-11} m/s for $K_{max} = 30.2$ MPa·m$^{1/2}$ (27.5 ksi·in.$^{1/2}$)] reported in the previous paragraph for this weld alloy was calculated for the time period 720-1450 h; hence, it does not include the period of apparently faster growth that followed. This latter period began after a malfunction of the power switch to the pump. The malfunctioning switch caused the pump to turn on and off intermittently every few seconds. Figure 64 shows that, as the pump began the on/off cycle at around 1450 h (the stress intensity factor K reflects that behavior), the crack growth first displayed a jump (consistent with the breaking of ligaments), then appeared to follow the oscillations in the stress intensity factor until the switch was replaced. After the switch was replaced, the constant load conditions were restored; however, the subsequent CGR doubled. The cause for the observed behavior is not understood.

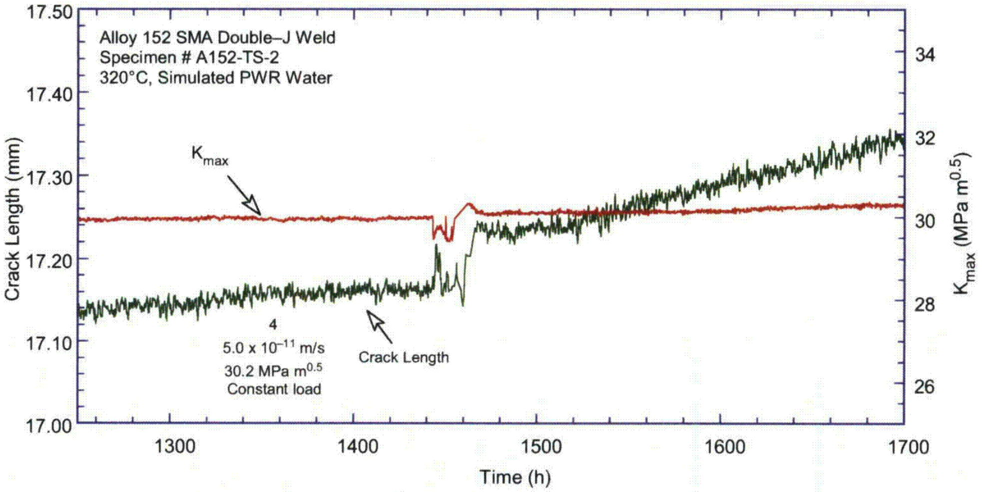

Figure 64. **Crack length vs. time for Alloy 152 weld specimen A152-TS-2 in simulated PWR environment during constant-load test period 4.**

The resulting fracture surface was examined by optical microscopy and SEM. Figure 65 shows images of the two halves of the specimen. These indicate that the testing procedure resulted in a straight, uniform fracture surface. These images were also used to determine the correction for the DC potential data. The correction was small (16%) as growth under constant load (where ligaments that confound the DC potential measurements are expected to form) was small when compared with the total crack advance.

The cracking seems to have propagated on four fronts on slightly different planes, resulting in an arched appearance (Fig. 65b). Letters A-D indicate the intersections of these planes. The ductile fracture mode observed at the intersections of the planes (e.g., at locations A-D) most likely occurred when the specimen was fractured at the end of the test, and this finding substantiates the previous observation that the cracking occurred on different planes. Nevertheless, the fracture mode was predominantly IG for each of the four arches. For example, Fig. 66 shows the region between locations A and B with predominant IG cracking and a band-like appearance. Overall, the engagement of the IG fracture mode was 82% for this specimen.

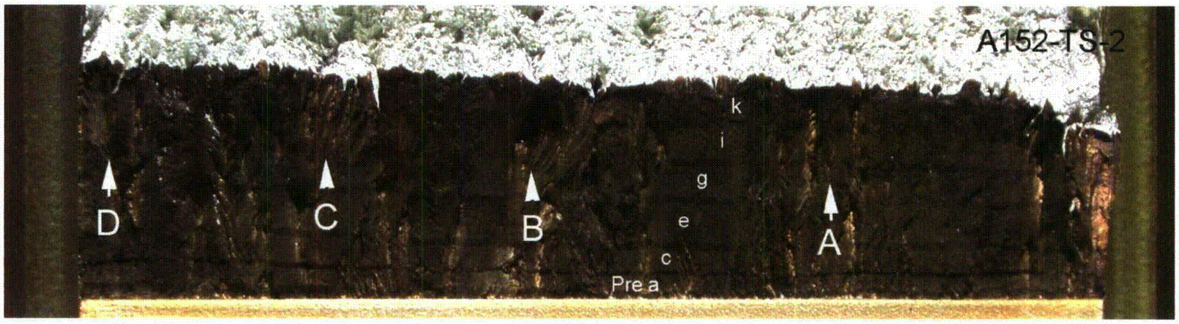

(a)

Figure 65. **Fracture surface of specimen A152-TS-2 by (a) optical and (b) electron microscopy. Crack advance is from bottom to top.**

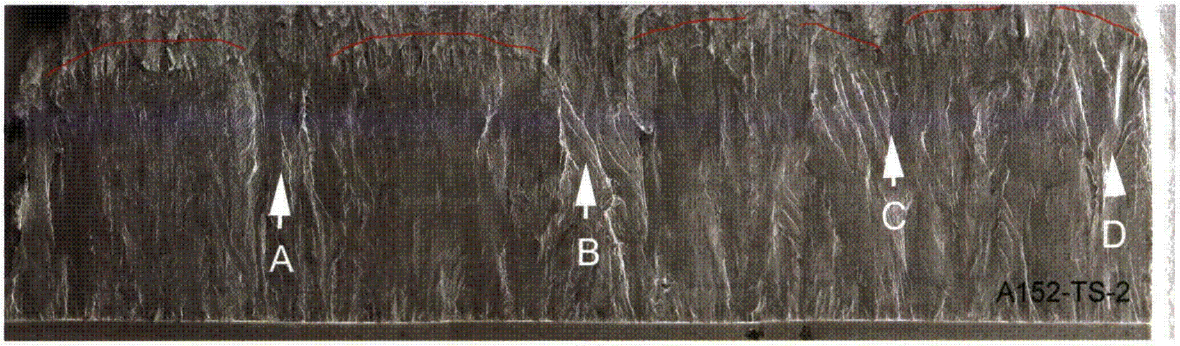

(b)

Figure 65. (cont.)

Figure 66. Intergranular cracking on the fracture surface of specimen A152-TS-2 between A and B in Fig. 65. Crack advance is from bottom to top.

The portion of the fracture surface after the transition to a predominantly IG mode is shown in additional detail in Figs. 67-69. For this purpose, the crack front is divided in three regions. In each region, several features of interest are shown at higher magnification and discussed. While the fracture mode appears to be predominantly IG, of particular interest were areas that appeared to be more resistant to IG SCC.

Figure 67a shows the first of the three regions. Figures 67b and 67c are high magnification micrographs taken at locations 1 and 2 in Fig. 67a. While the fracture mode appears to be predominantly IG in Fig. 67 a, Fig. 67b shows a region of TG fracture. The ductile fracture found in this area (location 1) suggests that the cracks may be propagating on slightly different planes. Also, there are secondary cracks perpendicular to the direction of the crack front, but no secondary IG cracks. By contrast, Fig. 67c shows a region where the fracture mode is mostly IG with an interdendritic appearance. The grain in the center of the micrograph has interdendritic features, although not as prominent as those of its neighbors. Moreover, as indicated by arrows, apparently all grain boundaries adjacent to this grain are cracked.

Figure 68a shows the second of the three regions, and Figs. 68b and 68c are high magnification micrographs taken at locations 1 and 3 in Fig. 68a. As with the previous example, while the fracture mode appears to be predominantly IG in Fig. 68a, Fig. 68b shows a region of TG fracture. This region appears similar to that shown in Fig. 67b; however, in addition to the secondary cracks, dendritic elements can also be observed. A common feature is the absence of secondary IG cracks. Figure 68c was taken at location 3 in Fig. 68a and corresponds to location C of Fig. 65. The ductile fracture suggests that the cracks propagated on slightly different planes and became connected only when the specimen was fractured at the end of the test.

Finally, Fig. 69a shows the third of the three regions, and Figs. 69b and 69c are high magnification micrographs taken at locations 1 and 2 in Fig. 69a. These show areas with an apparent mixed fracture mode. Nevertheless, secondary IG cracks are observed. Figure 69a shows a case where what appears to be a smooth faceted fracture is actually preceded by an interdendritic fracture, and illustrates how the IG crack indicated by the arrow turns into an interdendritic fracture. In a similar fashion, the two IG cracks shown in Fig. 69c turn into an interdendritic fracture.

Figure 70 further illustrates the role of secondary IG cracks. These types of cracks appear to develop during transitioning and signal the onset of IG/interdendritic cracking. For example, the IG crack indicated by an arrow seems to have initiated well ahead of the constant load region; however, it apparently propagated sideways, toward the side groove of the specimen.

In summary, the engagement of the IG fracture mode was 82% for this specimen. However, areas of TG and mixed TG/IG were found. A common feature for the TG areas is secondary cracking across the crack propagation direction. Also, secondary IG cracks were observed in some cases, suggesting that the IG engagement would have probably been even higher if this (screening) test had lasted longer.

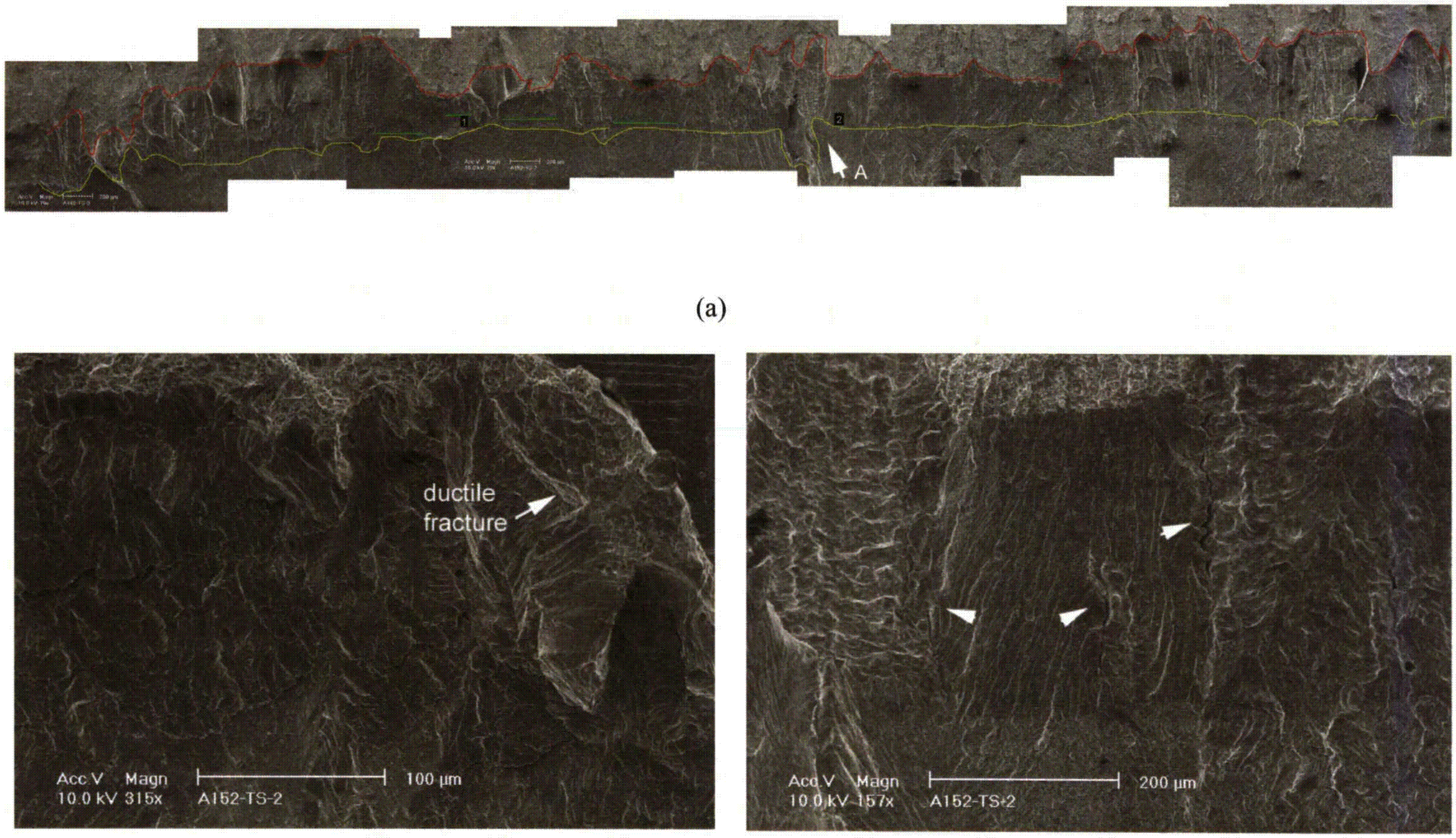

(a)

(b)

(c)

Figure 67. **Specimen A152-TS-2: (a) first third of fracture surface, (b) detail at location 1, and (c) detail at location 2. Crack advance is from bottom to top.**

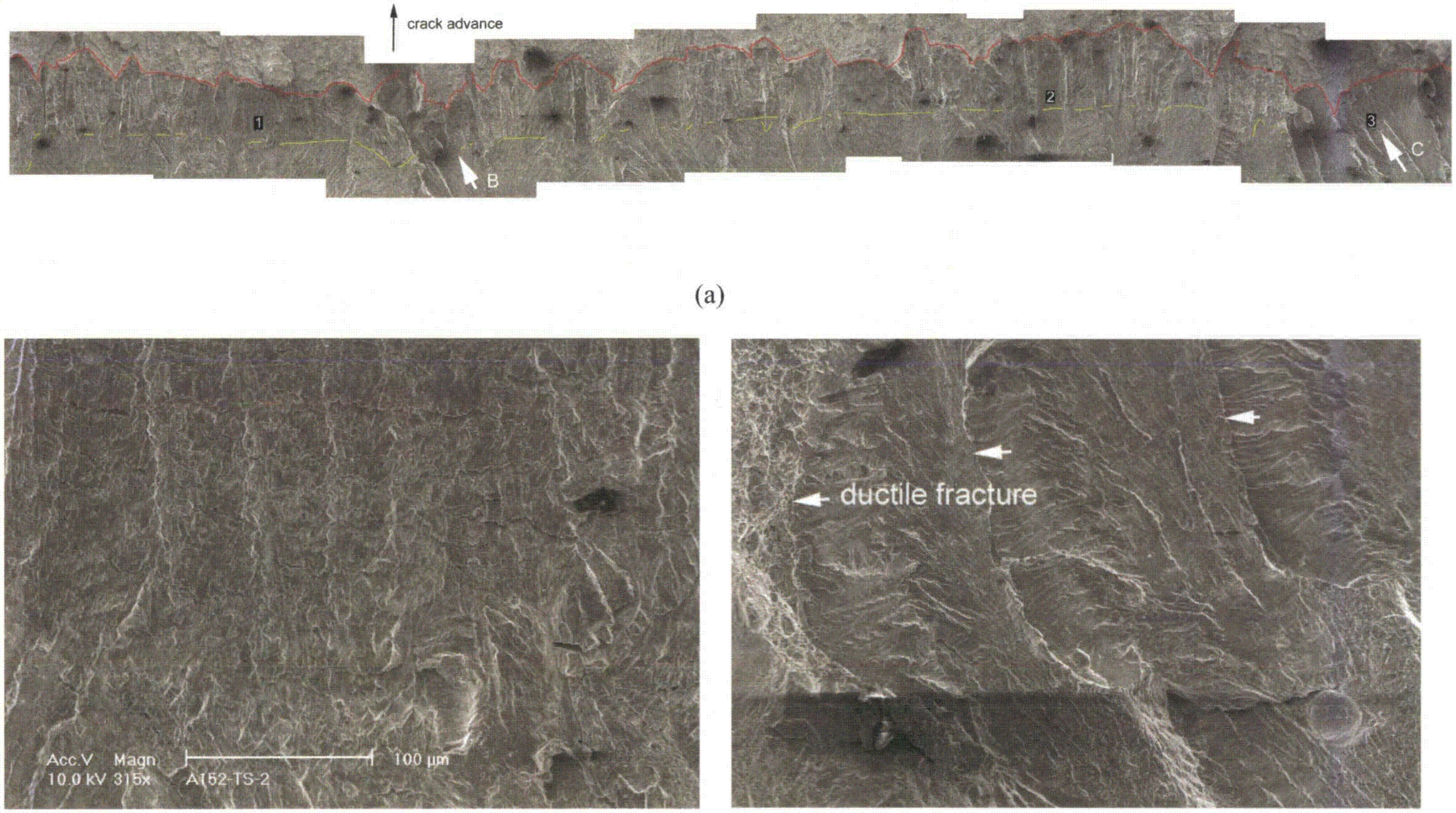

(a)

(b)

(c)

Figure 68. **Specimen A152-TS-2: (a) second third of fracture surface, (b) detail at location 1, and (c) detail at location 3. Crack advance is from bottom to top.**

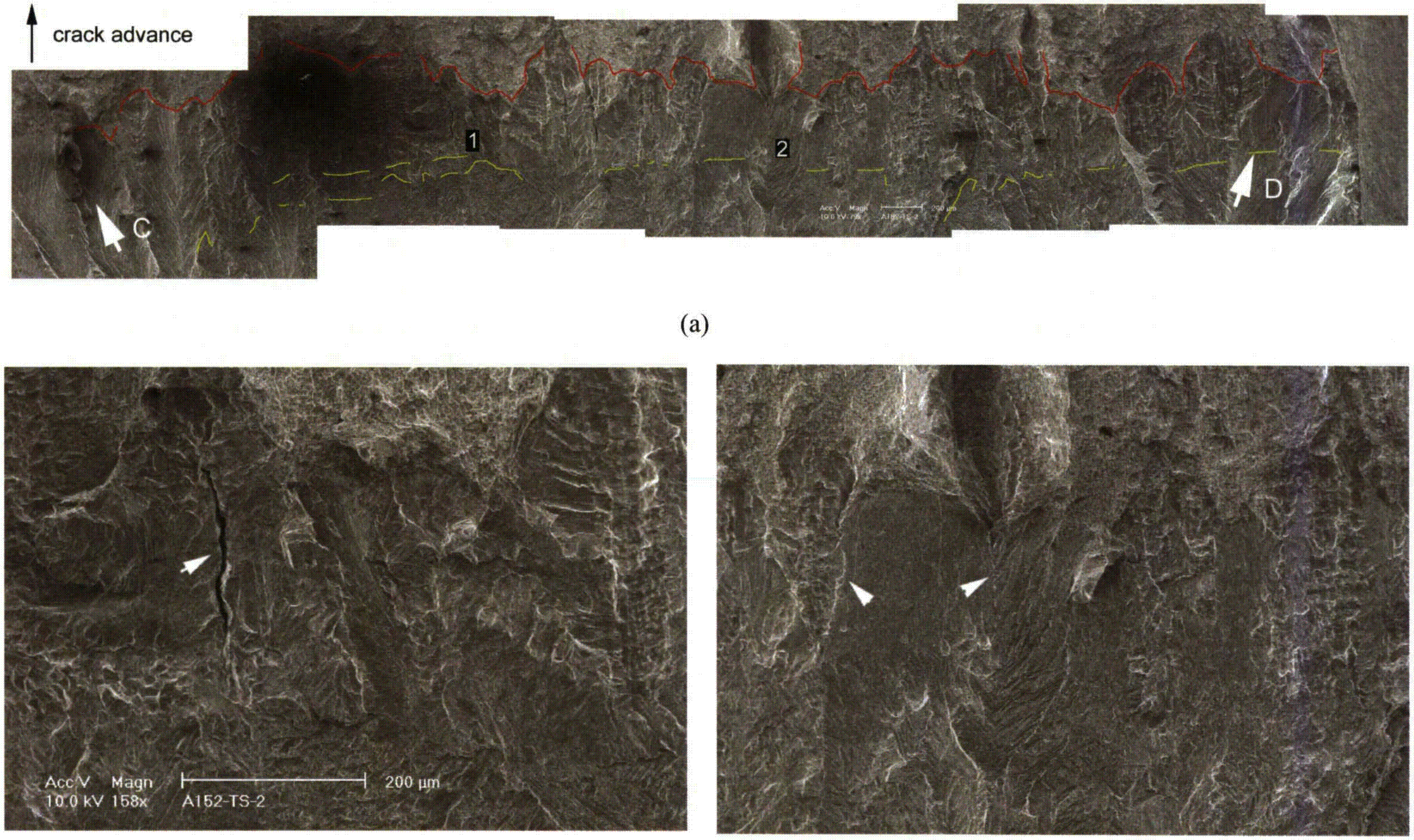

(a)

(b) (c)

Figure 69. **Specimen A152-TS-2: (a) last third of fracture surface, (b) detail at location 1, and (c) detail at location 2. Crack advance is from bottom to top.**

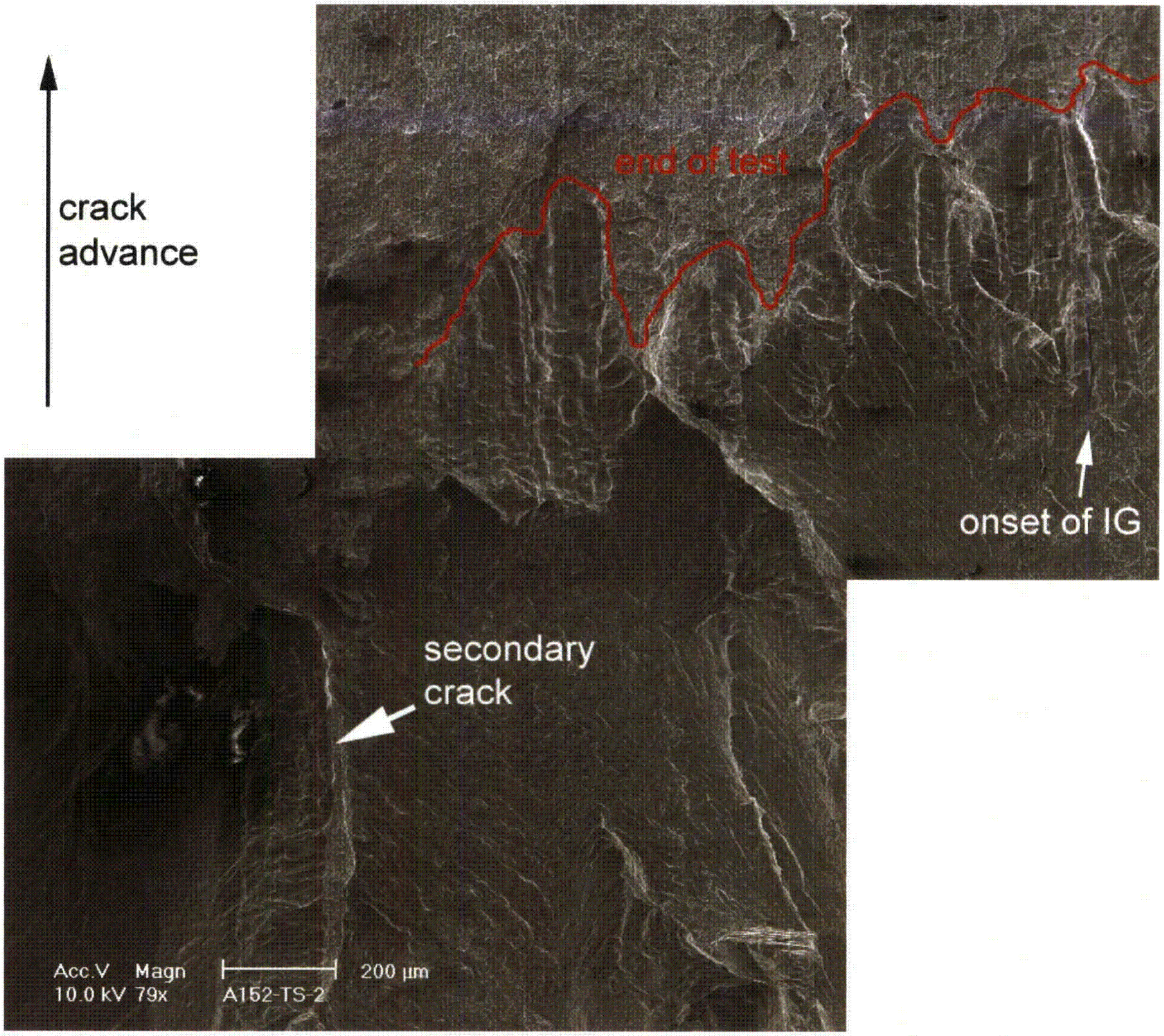

Figure 70. Region of fracture surface of specimen A152-TS-2. Crack advance is from bottom to top.

4.4.2 Specimen A152-TS-4

This test was conducted on an Alloy 152 weld specimen similar to the one described previously. The test conditions for specimen A152-TS-4 are given in Table 16, and the changes in crack length and K_{max} with time are shown in Fig. 71.

Table 16. Crack growth data for specimen A152-TS-4 of Alloy 152 weld in PWR water.[a]

Test Period	Test Time, h	Temp., °C	Load Ratio R	Rise Time, s	Down Time, s	Hold Time, s	K_{max}, MPa·m$^{1/2}$	ΔK, MPa·m$^{1/2}$	CGR_{env}, m/s	Estimated CGR_{air}, m/s	Crack Length, mm
Pre a	32	319.8	0.3	0.5	0.5	0	19.4	13.6	4.61E-08	4.51E-08	13.111
Pre b	96	319.7	0.3	50	50	0	19.5	13.7	1.17E-09	4.57E-10	13.235
Pre c	104	319.7	0.3	0.5	0.5	0	20.5	14.4	5.94E-08	5.62E-08	14.130
Pre d	119	319.7	0.3	50	50	0	20.5	14.4	1.52E-09	5.68E-10	14.173
Pre e	128	319.3	0.3	0.5	0.5	0	21.8	15.3	8.15E-08	7.29E-08	15.327
Pre f	144	319.4	0.3	50	50	0	21.8	15.3	1.76E-09	7.36E-10	15.399
Pre g	152	319.4	0.3	0.5	0.5	0	23.9	16.7	1.18E-07	1.06E-07	17.148
Pre h	168	319.5	0.3	50	50	0	24.0	16.8	3.03E-09	1.09E-09	17.267
Pre i	173	319.4	0.3	1	1	0	25.0	17.5	7.71E-08	6.42E-08	18.056
1	200	319.4	0.49	50	12	0	25.3	12.9	1.36E-09	6.12E-10	18.141
2	264	319.8	0.49	300	12	0	25.3	12.9	3.22E-10	1.03E-10	18.225
3	336	319.1	0.49	600	12	0	25.3	12.9	8.63E-11	5.07E-11	18.255
4	626	319.4	0.49	1000	12	0	25.3	12.9	5.85E-11	3.07E-11	18.303
5	817	319.3	0.69	1000	12	0	25.3	7.8	7.41E-12	8.03E-12	18.306
6	960	319.6	0.49	1000	12	0	25.4	13.0	7.92E-11	3.12E-11	18.355
7	1293	319.3	1	0	0	0	25.4	0.0	negligible	-	18.355
8	1,651	319.4	0.49	300	12	0	25.6	13.0	3.89E-10	1.06E-10	18.480
9	2,141	320.0	1	0	0	0	25.6	0.0	5.07E-12	-	18.490
10	2,170	320.3	0.48	300	12	0	30.0	15.6	5.18E-10	2.18E-10	18.554
11	2,375	319.8	1	0	0	0	30.1	0.0	negligible	-	18.554
12	2,448	319.5	0.48	300	12	0	30.2	15.7	5.51E-10	2.22E-10	18.682
13	2,616	319.6	0.48	300	12	3600	30.3	15.8	6.69E-11	1.73E-11	18.725
14	2,856	319.4	1	0	0	0	30.3	0.0	negligible	-	18.725
15	2,888	320.0	0.48	50	12	0	30.7	16.0	2.17E-09	1.42E-09	18.936
16	2,952	320.1	0.48	300	12	0	30.9	16.1	5.42E-10	2.43E-10	19.067
17	3,023	319.5	0.48	600	12	0	31.0	16.1	2.67E-10	1.23E-10	19.146
18	3,120	319.7	0.48	1000	12	0	31.1	16.2	2.92E-10	7.54E-11	19.221
19	3,694	319.8	1	0	0	0	31.0	0.0	6.09E-12	-	19.224
20	3,722	320.3	0.48	50	12	0	31.4	16.3	2.34E-09	1.56E-09	19.399
21	3,816	320.4	0.48	300	12	0	31.7	16.5	5.19E-10	2.71E-10	19.569
22	3,828	320.9	0.22	1	1	0	26.0	20.2	6.64E-08	9.85E-08	20.752
23	3,840	320.6	0.22	50	50	0	26.1	20.3	4.49E-09	2.00E-09	20.832
24	3,870	320.3	0.48	50	12	0	34.4	17.9	3.57E-09	2.29E-09	21.164
25	3,894	320.1	0.48	300	12	0	34.5	17.9	8.07E-10	3.83E-10	21.233
26	4,017	320.5	0.48	600	12	0	34.9	18.1	5.00E-10	2.02E-10	21.452
27	4,064	320.5	0.48	1000	12	0	35.0	18.2	3.35E-10	1.23E-10	21.505
28	4,399	320.1	1	0	0	0	35.3	0.0	8.28E-12	-	21.515
29	4,655	319.4	0.48	300	12	7200	35.2	18.3	7.19E-11	1.66E-11	21.561
30	4,828	319.6	1	0	0	0	35.2	0.0	negligible	-	21.561
31	4,969	319.3	0.70	600	12	0	35.4	10.6	1.12E-10	4.80E-11	21.602
32	5,136	319.6	0.70	600	12	3600	35.5	10.6	1.41E-11	6.96E-12	21.607
33	5,812	319.0	0.70	600	12	7200	35.5	10.7	1.81E-11	3.74E-12	21.659
34	5,863	319.1	1	0	0	0	35.5	0.0	negligible	-	21.659
35	5,966	318.9	0.7	600	12	7200	35.5	10.7	1.02E-11	3.74E-12	21.662
36	6,081	319.2	0.7	600	12	0	35.4	10.6	1.24E-10	4.84E-11	21.704
37	6,103	319.1	0.5	600	12	0	35.8	17.9	5.30E-10	1.99E-10	21.753
38	6,152	319.2	0.5	1000	12	0	36.0	18.0	3.54E-10	1.22E-10	21.803
39	7,657	319.1	1[b]	0	0	0	36.2	18.1	3.08E-11	-	21.957
40	7,665	319.2	0.5	12	12	0	36.5	18.2	7.99E-09	1.10E-08	22.087

[a] Simulated PWR water with 2 ppm Li, 1000 ppm B, DO <10 ppb. Conductivity was 21 ± 3 μS/cm, and pH 6.4.

[b] Also includes periodic unloading by 50% every 7200 s. Unload/reload times were 12 s/12 s.

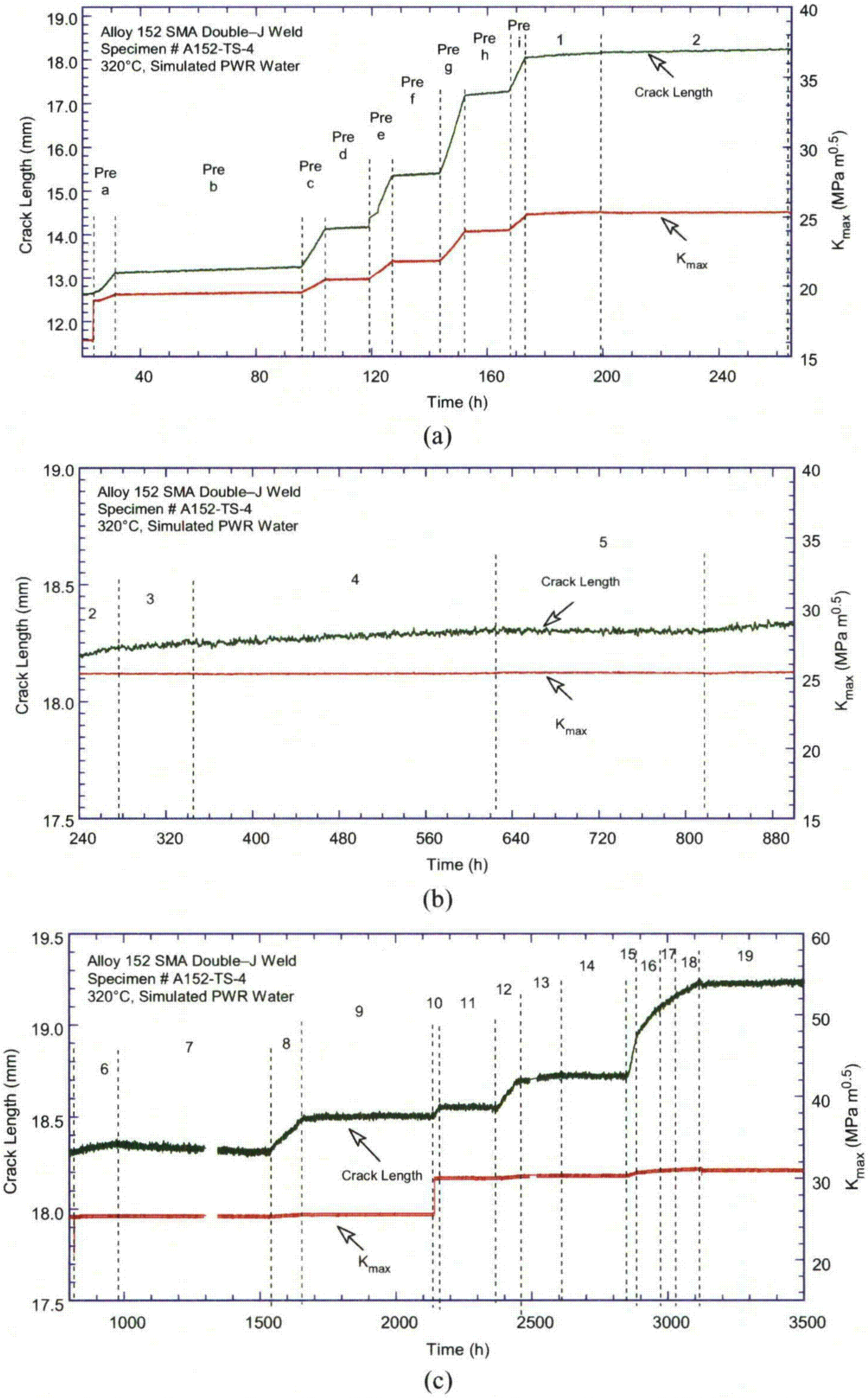

(a)

(b)

(c)

Figure 71. **Crack length vs. time for Alloy 152 weld specimen A152-TS-4 in simulated PWR environment during test periods (a) precracking-2, (b) 3-5, (c) 6-19, (d) 20-25, (e) 26-37, and (f) 38-39.**

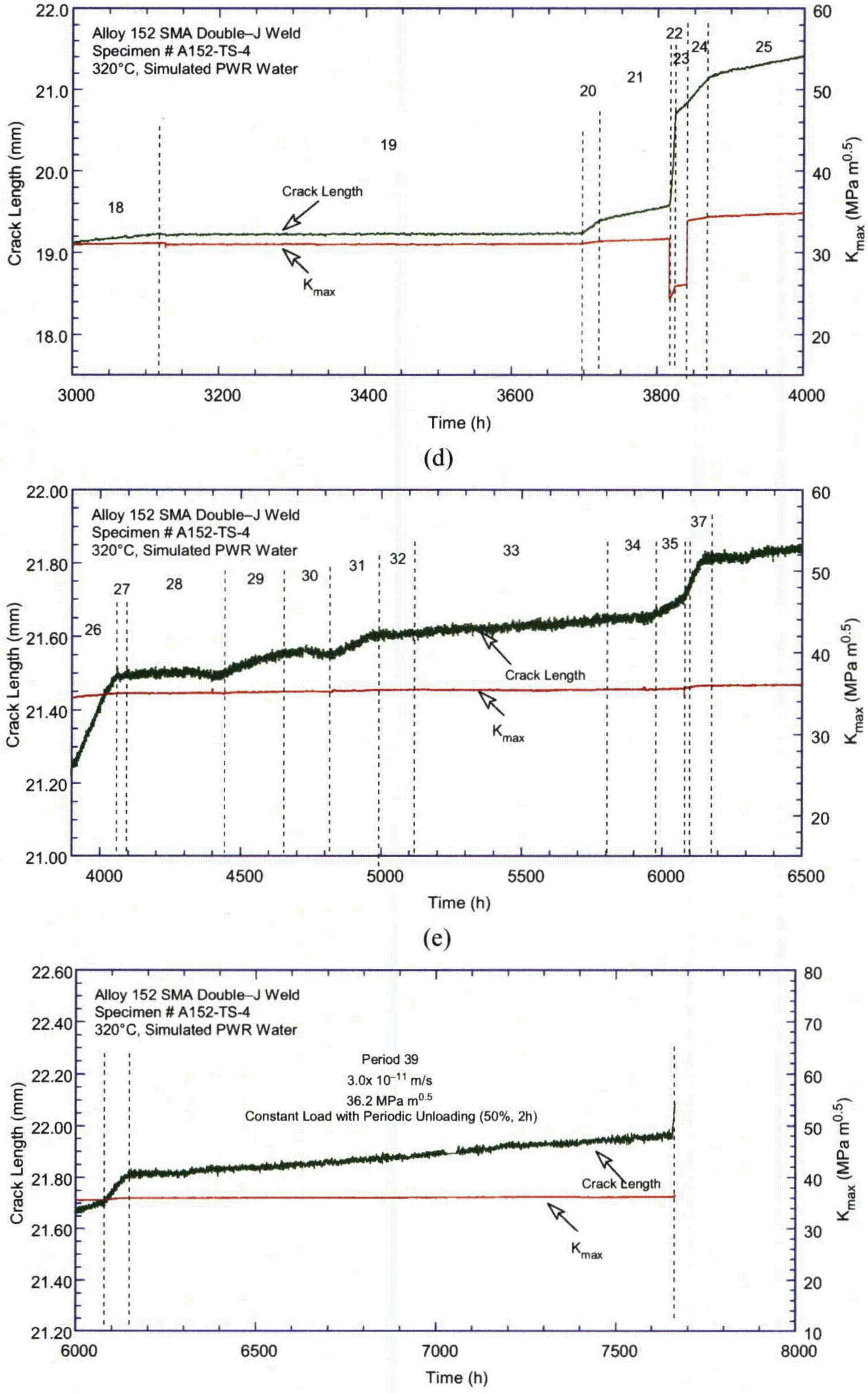

(d)

(e)

(f)

Figure 71. **(cont.)**

The resulting fracture surface was examined by optical microscopy and SEM. Figure 72 shows a photograph of the entire fracture surface. Transitioning to IG was attempted in two microstructural regions approximately 1 mm (0.04 in.) apart. Between these two regions, the crack was advanced by fatigue (period 22), and this period appears lighter on the fracture surface. The image indicates that the testing procedure resulted in a straight, uniform fracture surface. This image was used to determine the correction factors for the DC potential data. The correction was small (9.5%), as a cyclic component was almost always present and, thus, ligament formation was kept to a minimum.

Figure 73 shows the fracture surface during the final periods of the test when the SCC CGRs were determined. To provide additional detail, the fracture surface was divided into three regions along the width. The fracture mode was almost entirely IG with interdendritic features. Overall, the engagement of the IG fracture mode was 92%, which is larger than that for the previous specimen; this difference is not surprising given the much longer time allotted to this test.

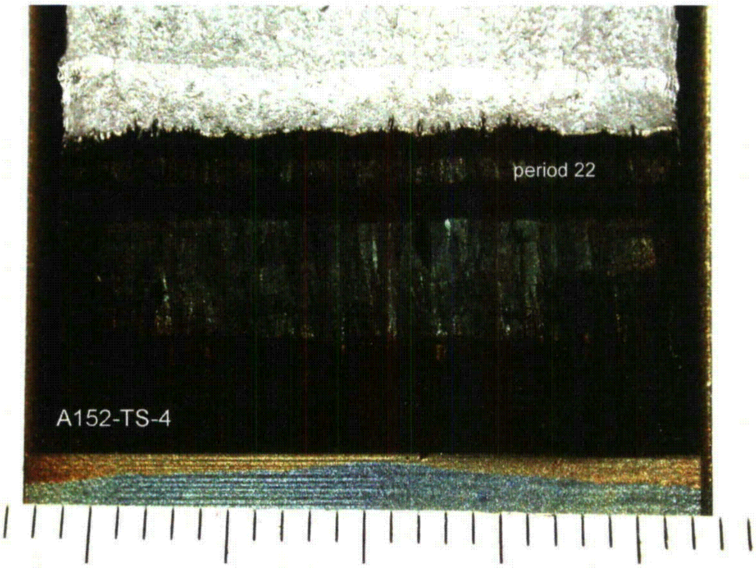

Figure 72.
Fracture surface of specimen A152-TS-4. Crack advance is from bottom to top.

The approach to transitioning from TG to IG was similar to that used in the previous test. However, the environmental enhancement was initially lower than that observed previously (compare, for example, periods 4 and 6 of Table 16 vs. period 3 of Table 15). Hence, the initial attempts to measure a CGR at constant load were unsuccessful.

A degree of environmental enhancement comparable with specimen A152-TS-2 was obtained only later in the test. However, the inability to sustain a CGR at constant load consistent with the previous specimen ($\approx 10^{-11}$ m/s) suggested the formation of ligaments. To attempt to break the ligaments, in the second part of the test (after period 22), alternative loading conditions – slow/fast cycling with hold times or constant load with periodic unloading – were chosen. These loading procedures were successful in keeping the formation of "fingers" and ligaments at a minimum (hence, the small correction factor reported for this specimen). The SCC CGRs were calculated during several slow/fast cycling tests with hold times or periodic unloading (see Table 16). Typically, a well-characterized, environmentally enhanced slow/fast condition was chosen, and a hold period was introduced. The expectation was that the SCC CGR component would grow during the hold period. The SCC CGR was then calculated by superposition (Eq. 10). As such, based on the results of periods 21 and 29 (Table 16) the SCC CGR was calculated to be 2.80 x 10^{-11} m/s for period 29 (2-h hold). In a similar fashion, using the crack growth rate measured in period 31, the SCC CGR was calculated to be 1.60 x 10^{-11} m/s once period 33 (2-h hold) was completed. Note that by increasing the hold times from 3600 s in period 32 to 7200 s in period 33, the measured crack growth rates stayed largely the same (≈ 1.5 x 10^{-11} m/s). This observation further substantiates the premise that at that stage of the test the SCC CGR component (and IG fracture) was dominant, although some degree of cycling appears necessary to sustain the crack growth over long periods of time. Finally, the SCC CGR was measured at constant load with periodic unloading. During period 39 a steady growth at a rate of 3.08 x 10^{-11} m/s was measured. The unload/reload cycle was relatively fast (12-s rise, 12-s down, R= 0.5) compared with the hold time (2 h), and by itself does not typically result in an IG fracture. As expected, when the hold time was removed (period 40), the measured CGR was equivalent to that expected in air, and the fracture mode reverted to TG for the final 100 μm of the test (Fig. 74). Therefore, the CGR measured in period 39 is due to IG SCC growth that occurred primarily during the hold periods at constant load. In summary, the SCC CGRs measured at constant load with periodic unloading or calculated from cycle + hold periods are consistent with those measured at constant load.

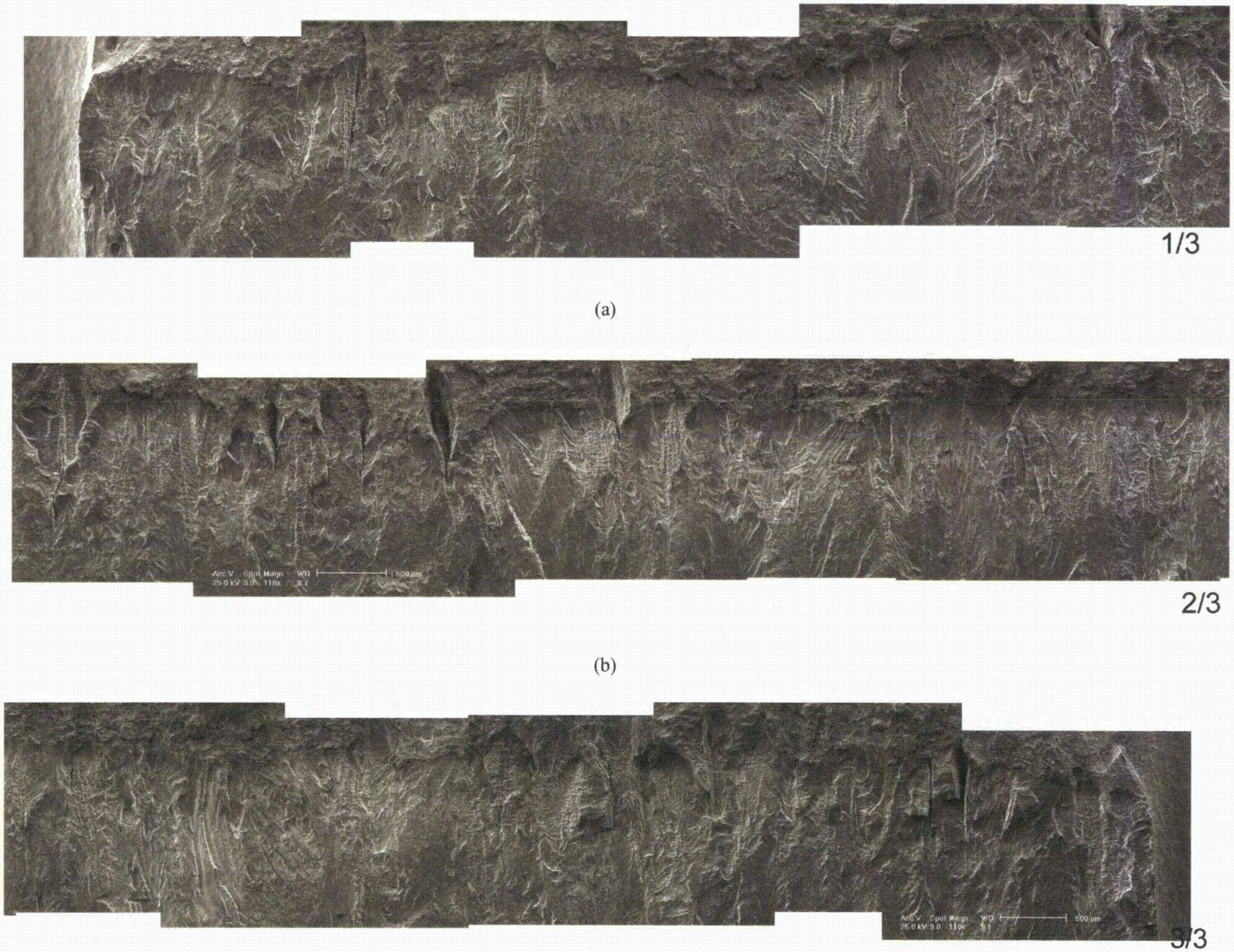

(a)

(b)

(c)

Figure 73. Intergranular region at the end of specimen A152-TS-4. The image was broken into three regions. Crack advance is from bottom to top.

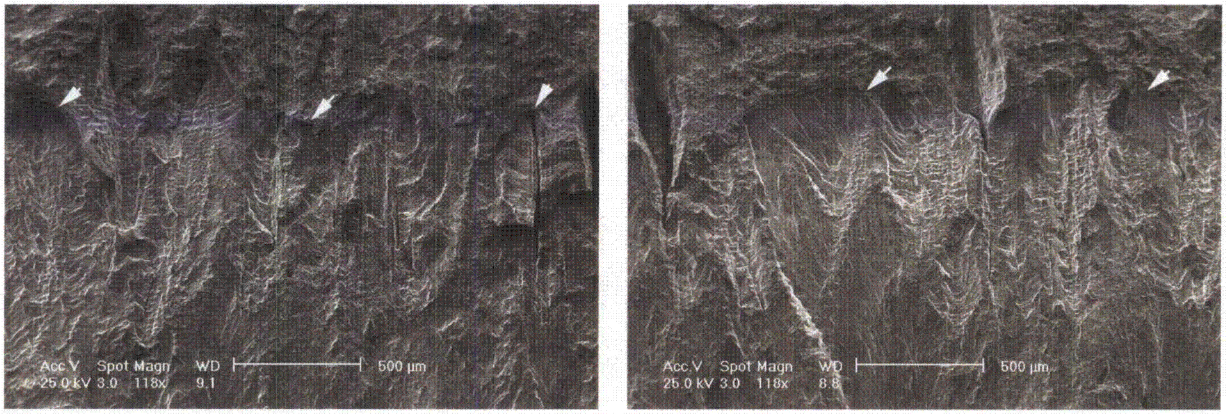

Figure 74. **Fracture surface of specimen A152-TS-4 at the end of the test (arrows). Crack advance is from bottom to top.**

At the end of the test, the fracture surface was also examined for evidence of ligaments to provide additional validity to the rationale behind the test management described previously. Two examples are shown in Fig. 75. Figure 75a shows a predominantly IG fracture mode, with a high density of secondary IG cracks. In the center of the image, the IG crack went out of plane, forming the ligament indicated by the arrow. Figure 75b shows a high magnification micrograph of the two fracture modes: IG on the left side and TG on the right side. Interdendritic features are also recognizable on the TG side, as well as secondary cracks similar to those observed on the previous specimen (Fig. 67b), suggesting a crack-resistant grain. Striations are also visible, consistent with a fatigue-driven crack advance. In other words, the cyclic component broke through such grains (and ligaments) and enabled a CGR to be measured in real time.

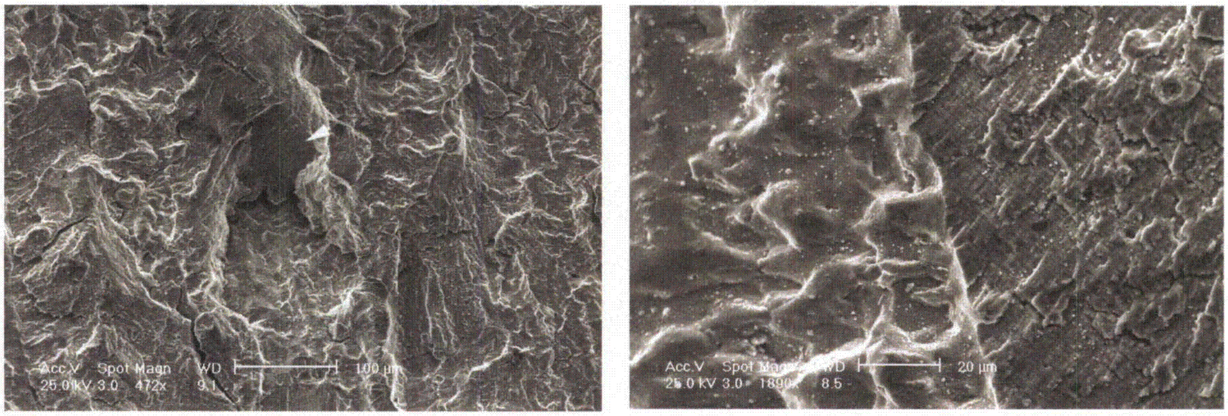

Figure 75. **Ligaments on the fracture surface of specimen A152-TS-4: (a) out-of-plane crack and (b) interdendritic (left) and TG (right) fracture modes. Crack advance is from bottom to top.**

Upon the destructive examination of the specimen, IG fracture features were also observed prior to period 22 (Table 16), as shown in Fig. 76.

Figure 76.
Fracture surface of specimen A152-TS-4 prior to period 22. Crack advance is from bottom to top.

5. Discussion

The section summarizes the crack growth rate results for Alloy 690 and 152 weld and compares these results with similar data obtained earlier at ANL and elsewhere. The significance of the results is discussed in the context of data obtained previously on Alloy 600 and 82/182 welds. The activation energy for crack growth in Alloy 690 is also discussed.

5.1 Alloy 690

5.1.1 Cyclic Crack Growth Rates

Cyclic CGRs for Alloy 690 obtained in previous testing programs at ANL have been evaluated to develop correlations for estimating the cyclic CGRs in Alloy 690 as a function of loading and environmental conditions. The data were obtained from tests conducted with a triangular or slow/fast sawtooth waveform. The load ratio R was in the range of 0.2-0.9, K_{max} was in the range of 30-50 MPa·m$^{1/2}$ (27-46 ksi·in.$^{1/2}$), and the rise time was 12 s for most of the tests.[2-4,7]

Figure 77 shows cyclic CGR data for Alloy 690 in the mill annealed (MA), solution annealed [SA, 1093°C (1999°F) for 1 h], and thermally treated [TT, 715°C (1319°F) for 5 h] conditions from previous ANL[7] and Babcock & Wilcox[42] (B&W) tests. The cyclic rates measured in primary water are plotted vs. the cyclic rates predicted for Alloy 690 under the same loading conditions in air (see Eqs. 11 and 13). Figure 77a shows excellent agreement between the measured and predicted rates. It also indicates that under the testing conditions employed, no environmental enhancement occurred. Previous ANL cyclic data on Alloy 690 obtained in high purity water at 320°C (608°F) with low DO content are shown in Fig. 77b. The data indicate that under certain loading conditions, the rates in the environment begin to drop – an effect consistent with the existence of a threshold, ΔK_{th}, for cyclic rates.

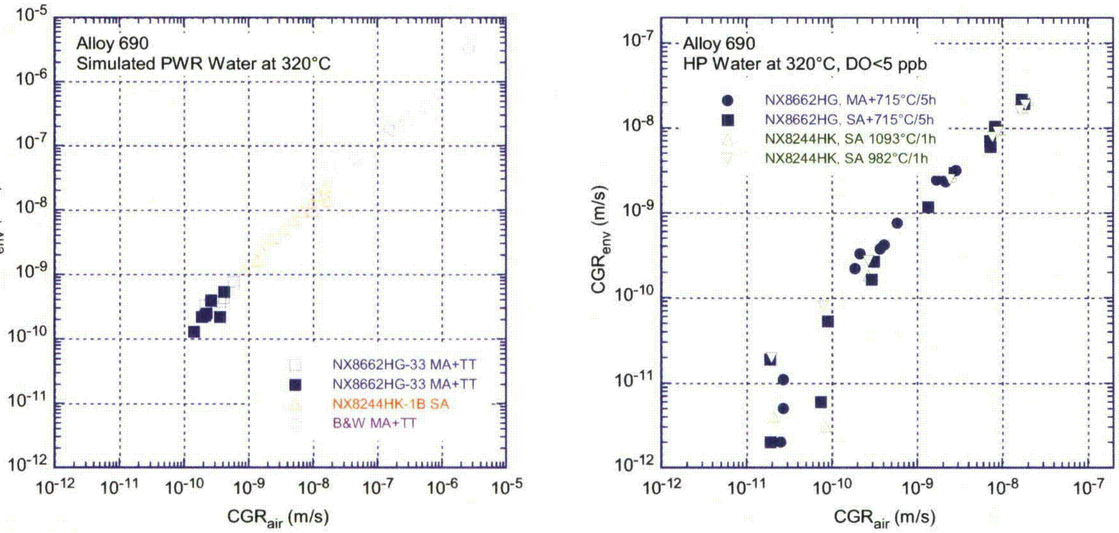

(a) (b)

Figure 77. **Cyclic CGR data for (a) Alloy 690 in SA and TT conditions from previous ANL and B&W tests in PWR environment and (b) Alloy 690 in high purity water with low DO as a function of growth rates for Alloy 690 in air. Test temperature is 320°C (608°F).**

Figure 78 shows the cyclic CGR data for Alloy 690 in the 26% cold-rolled condition and data for Alloy 600 from the Davis-Besse CRDM nozzle #3.[9] Also included is a best fit curve for the Davis-Besse Alloy 600 data, as the rates for this alloy were generally higher than those for other heats of Alloy 600 tested previously. The plot shows that in the mechanical fatigue regime (≈ 1-3 x 10^{-8} m/s), both data sets are in good agreement. The test protocol employed for the purpose of transitioning from TG to IG led to environmental enhancement for the two cold-worked specimens, and these rates were typically higher than predicted by the corrosion fatigue curve for Davis-Besse Alloy 600. The exceptions are two data points obtained on specimen A690WC-ST-1 that fall on the corrosion fatigue curve. These correspond to periods 5 and 7 of Table 11, which were conducted with the intention of briefly exploring the effect of a larger load ratio and were not used as final transitioning conditions. The relatively large environmental enhancement of cold-rolled Alloy 690 suggests that transitioning to IG occurs readily, and relatively high SCC CGRs are expected.

The high levels of environmental enhancement observed in both Davis-Besse CRDM nozzle Alloy 600 and 26% cold-rolled Alloy 690 are reflected in the respective fracture surfaces (Fig. 79). A unique feature of the Davis-Besse Alloy 600 was the predominantly IG fracture even during loading, leading to the high rates of mechanical fatigue crack growth. For example, the fracture surface of the Davis-Besse specimen N3CL-1 changed to IG near the machine notch, where the first grain boundary is encountered (Fig. 79a). The IG growth taking place in a regime dominated by mechanical fatigue (which normally results in TG cracking) suggests a weakness of the grain boundaries. Similarly, grain contours, some smooth facets, and IG cracks were observed on the fracture surface of the cold-rolled Alloy 690 specimen (Fig. 79b). Such features observed in an inherently more resistant alloy suggest a similar weakness at the grain boundaries. While the reason for the weakness of the grain boundaries in the Davis-Besse Alloy 600 is unknown, it may be a result of grain boundary segregation during fabrication. By contrast, the cracked grain boundary carbides observed in the cold-rolled Alloy 690 indicate, in a straightforward fashion, a weakness at grain boundaries. This possible effect of cracked grain boundary carbides on SCC will be addressed.

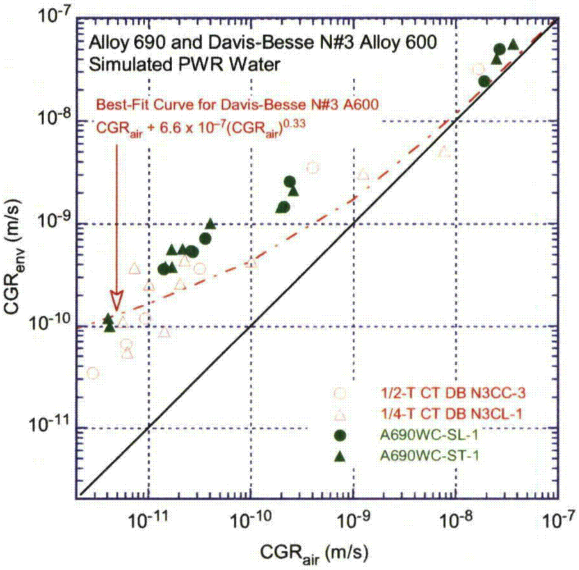

Figure 78.
Cyclic CGR data for 26% cold-rolled Alloy 690 and Alloy 600 from Davis-Besse in PWR environment at 320°C (608°F).

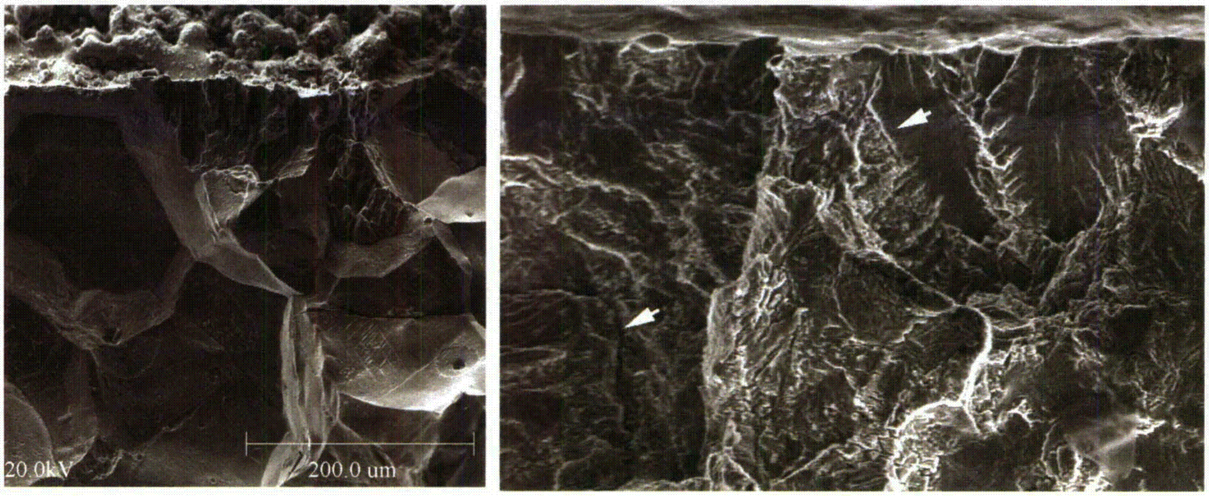

(a) (b)

Figure 79. (a) Transition from TG to IG fracture in Alloy 600 from Davis-Besse Nozzle #3, and (b) predominant TG fracture during transitioning in Alloy 690 cold-rolled by 26%. Grain contours, some smooth facets, and IG cracks are evident. In both cases, the sample notch is at the top of the figure, and crack advance is from top to bottom.

Figure 80 shows the cyclic CGR data for Alloy 690 CRDM tubing in the as-received condition and, for comparison, the Alloy 690 plate in the 26% cold-rolled condition. The rates for the alloy in the as-received condition appear to show some environmental enhancement, although much less than that for the cold-rolled alloy. Moreover, the cyclic rates for the as-received alloy also appear to be lower than the corrosion fatigue curve for Alloy 600. Hence, it is expected that as-received Alloy 690 is more resistant to SCC than Alloy 600.

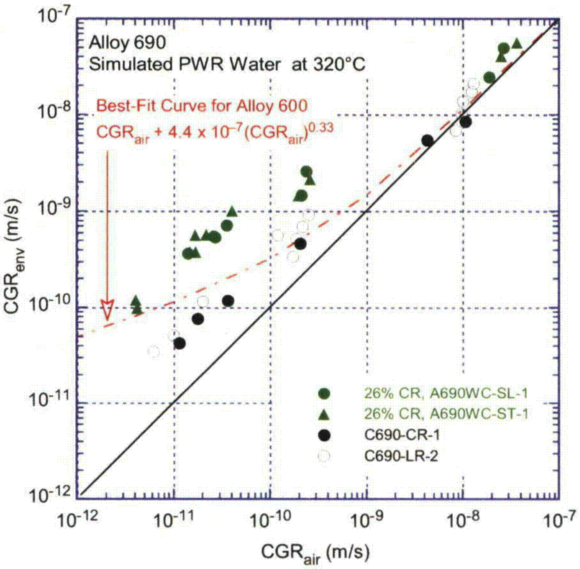

Figure 80.
Cyclic CGR data for 26% cold-rolled and as-received Alloy 690 specimens in PWR environment at 320°C (608°F).

5.1.2 SCC Crack Growth Rates

Figure 81 summarizes the SCC CGR data for Alloy 690 at various levels of cold work. Since the activation energy for SCC growth is not yet known for Alloy 690, the data presented in the figure were restricted to the temperature range 320-340°C (608-644°F), close to the operating temperature of PWRs. Likewise, the data included were obtained at dissolved hydrogen levels of 23-30 cc/kg. The data presented are from ANL for 26% cold-rolled material, Bettis Atomic Power Laboratory for 24% cold-rolled and 32% tensile prestrained alloys,[37] and Institute for Nuclear Safety System INSS for 20% and 50% cold-rolled alloys.[43] The proposed 75th and 50th percentile disposition curves for Alloy 600 (EPRI MRP-55[23]) are included for comparison.

The SCC CGR data developed at ANL on 26% cold-rolled Alloy 690 are in excellent agreement with those from 20% cold-rolled material developed at INSS,[43] especially for the tests conducted at a similar temperature (320°C, 608°F). These data are lower than those from 24% cold-rolled developed at Bettis[37] and from 50% cold-rolled material developed at INSS.[43] It is worth noting that the Bettis CGRs on the 24% cold-rolled alloy tested at 338°C (640°F) were the highest in their matrix, which also included tests at 360°C (680°F). Despite the different methods used to produce the deformation (cold rolling vs. tensile prestraining) and different deformation levels, the results show, in general, good agreement. The Alloy 600 75th percentile curve (EPRI MRP-55[23]) seems to bound most of the data.

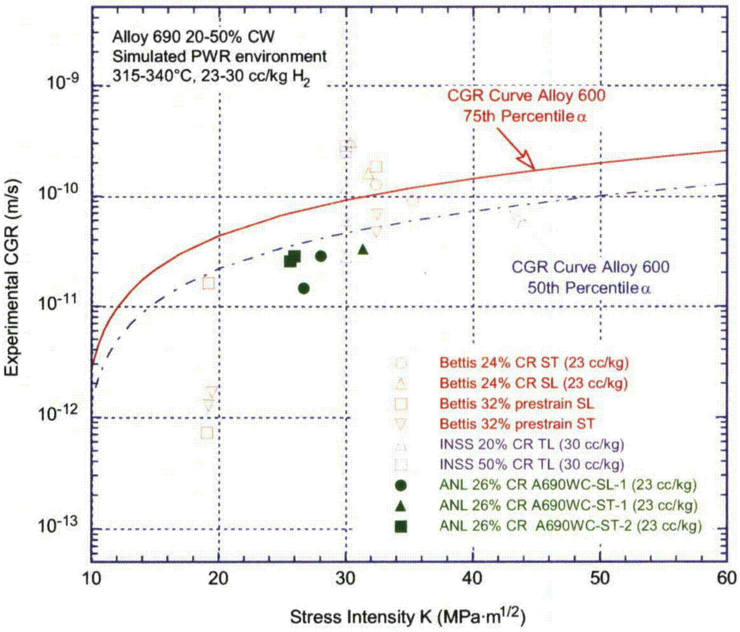

Figure 81.
SCC CGR data for cold-worked Alloy 690 in PWR environment at 320-340°C (608-644°F). The ANL data are shown with solid green symbols.

Figure 82 shows the data obtained for as-received Alloy 690 (solid black symbols). In order to put this data set in perspective, the plot includes data on cold-worked alloys as well as the proposed disposition curves for Alloy 600. The CGR rates measured for the alloys in the as-received condition are about an order of magnitude less than those obtained on the 26% cold-rolled alloy.

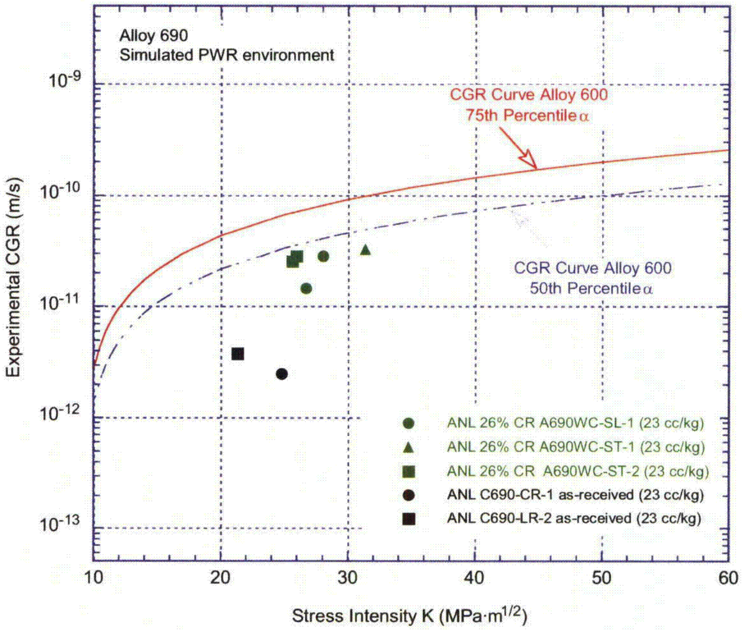

Figure 82.
SCC CGR data for as-received and cold-worked Alloy 690 in PWR environment at 320-340°C (608-644°F).

5.1.3 Activation Energy

Researchers at ANL and elsewhere have attempted to determine the activation energy for Alloy 690 in the cold-worked and as-received conditions. While scarce, the available data are summarized in Fig. 83.

An early attempt to determine the activation energy for 24% cold-rolled Alloy 690 was reported by Bettis[37] (Fig. 83a), and there was a rather weak dependence of SCC CGR on temperature . The ease of crack initiation and moderately high CGRs measured on the Alloy 690 plate cold-rolled by 26% made it attractive to attempt to determine the activation energy for SCC crack growth. The approach was to observe the effect of temperature on a crack that is already propagating. Figure 47c shows that temperature changes in the range 300-320°C (572-608°F) have little effect on the CGR ($\approx 3 \times 10^{-11}$ m/s that was initially established at 320°C (608°F). Similar behavior was observed in tests at GE on this 26% cold-rolled alloy,[38] albeit at a higher CGR [the GE tests were designed to maximize the initial SCC CGRs by starting the test at 360°C (680°F) at a potential near the Ni/NiO line]. While the SCC CGRs measured at ANL and GE seem to be in agreement via an activation energy close to that established for Alloy 600 (Fig. 83a), the lack of temperature effect observed in the individual tests, as well as in the Bettis data, is still not understood. Unlike the 24-26% cold-rolled alloys, the alloys cold-rolled by 20% responded to temperature changes in both GE[38] (Fig. 83b) and INSS[43] (Fig. 83c) tests, yielding activation energies close to that for Alloy 600 (130 kJ/mol). Alloy 690 in the as-received condition tested at ANL (Fig. 83c) also responded to temperature change in a manner similar to Alloy 600 (Fig. 83b). By contrast, the SCC rate in Alloy 690 cold-rolled by 50% was not found to be dependent on temperature in INSS tests (Fig. 83c).[43]

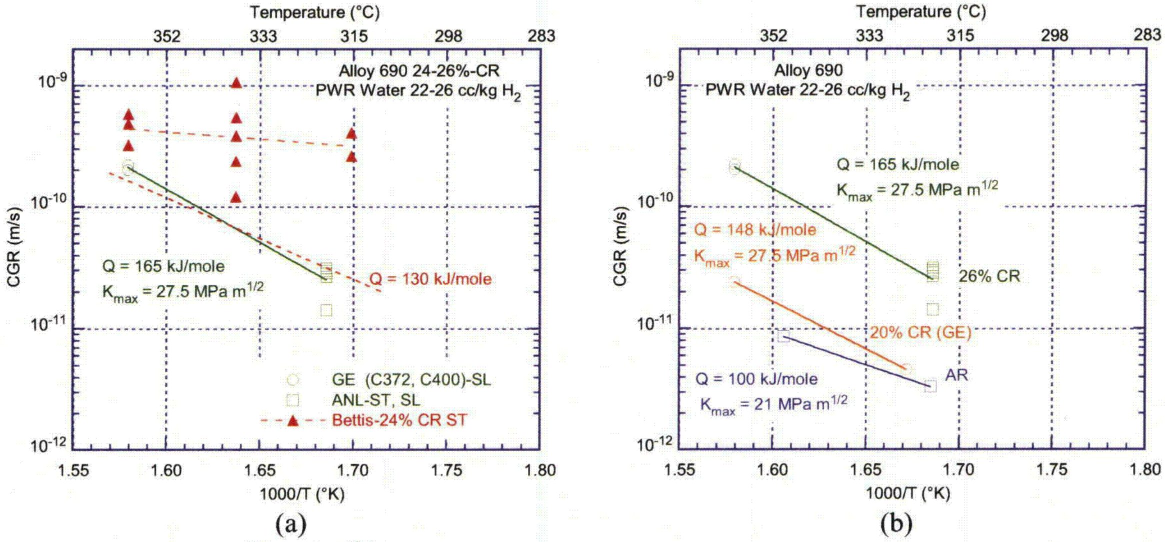

(a)

(b)

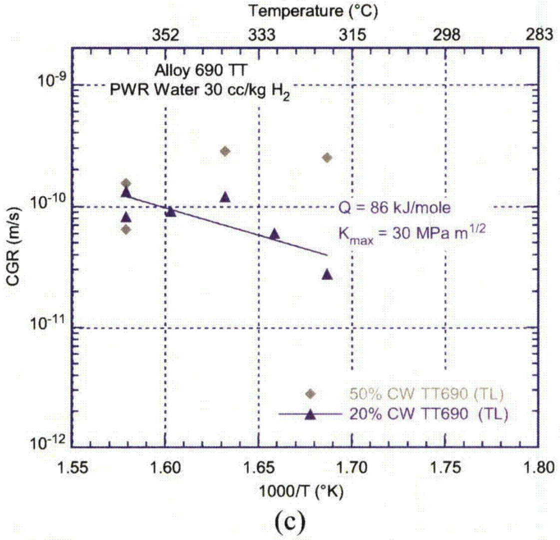

(c)

Figure 83.
Temperature dependence of the CGR data for Alloy 690: (a) 26% and 24% cold-rolled and as-received conditions obtained at ANL, GE,[38] and Bettis[37]; (b) 26% and 20% cold-rolled and as-received conditions obtained at ANL and GE[38]; and (c) 20% and 50% cold-rolled conditions obtained at INSS.[43]

In summary, despite the large scatter in CGR data, the results to date indicate that the activation energy for Alloy 690 is strongly affected by the deformation level of the alloy. Although there are substantial uncertainties in the present activation energies, alloys in the as-received condition and at deformation levels of up to 20% cold work appear to have an activation energy for SCC growth similar to that for Alloy 600 (130 kJ/mol). At higher deformation levels (24-26%), the effect of temperature seems to weaken, and by 50% cold work, the temperature appears to have no effect on SCC CGR.

Figure 84 explores the effect of normalizing the available SCC CGR data on cold-rolled alloys to 320°C (608°F) when using an activation energy of 130 kJ/mol. The plot contains the same data set shown in Fig. 81, except for the data obtained on the alloy cold-rolled by 50%. Data obtained at GE on 20-26% deformed alloy at 360°C (680°F) were normalized and included. The figure shows reasonable agreement among the data sets obtained at different laboratories. For this data set (Alloy 690 deformed by 20-32%), the Alloy 600 (MRP-55[23]) 50th percentile curve seems to bound most of the data.

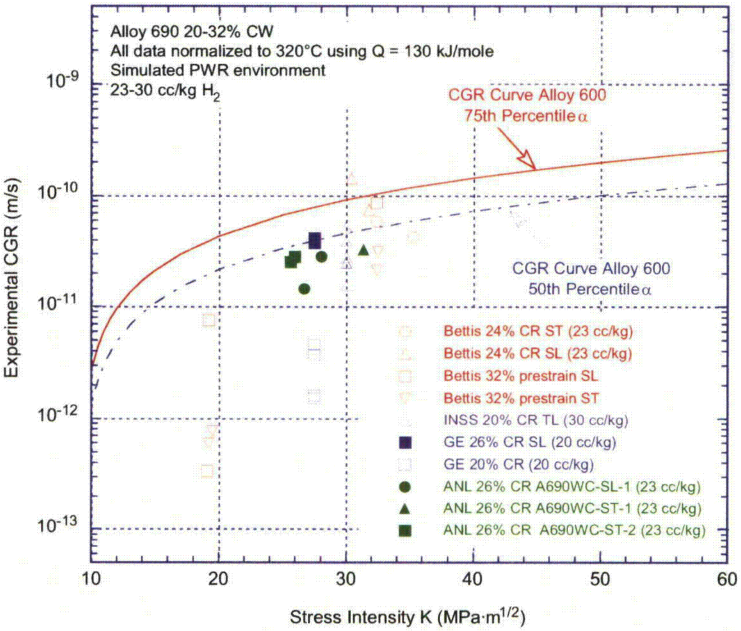

Figure 84.
SCC CGRs in PWR water for Alloy 690 heats deformed by 20-32%. The data were normalized to 320°C (608°F) in de-aerated water using an activation energy of 130 kJ/mol.

5.1.4 SCC of Cold-Worked Alloy 690 from a Mechanistic Perspective

The fundamental processes responsible for primary water SCC in Alloy 600 are not fully understood. Nevertheless, some key dependencies are known, and the current section attempts to discuss the SCC data for Alloy 690 based on the Alloy 600 experience. Specifically, the discussion considers a grain boundary deformation mechanism for SCC and attempts to explain the relatively high SCC CGRs measured on cold-worked Alloy 690.

This discussion is prompted by recent data by Arioka et al.,[43] at INSS, who found an excellent correlation between creep rates and susceptibility to SCC of Alloy 690 (Fig. 85a). The data also suggest that the activation energy for creep and SCC is similar; therefore, creep is a limiting factor for SCC. Fundamentally, the finding is very similar to that of Was et al.[44] for Alloy 600 (Fig. 85b), who showed that the steady-state creep rate and the percent cracked boundaries both correlate well with the CSLB fraction. The manner by which the creep correlates with cracking via the CSLB fraction suggests that creep and cracking are intimately linked. Since the macroscopic creep rate also reflects the rate of deformation at grain boundaries, the increased resistance of CSLBs to cracking may stem from their increased resistance to creep deformation. The similarity of the two data sets implys a fundamentally identical cracking mechanism for the two alloys and warrants a discussion of SCC behavior of Alloy 690 from the perspective of the proposed mechanisms for SCC of Alloy 600.

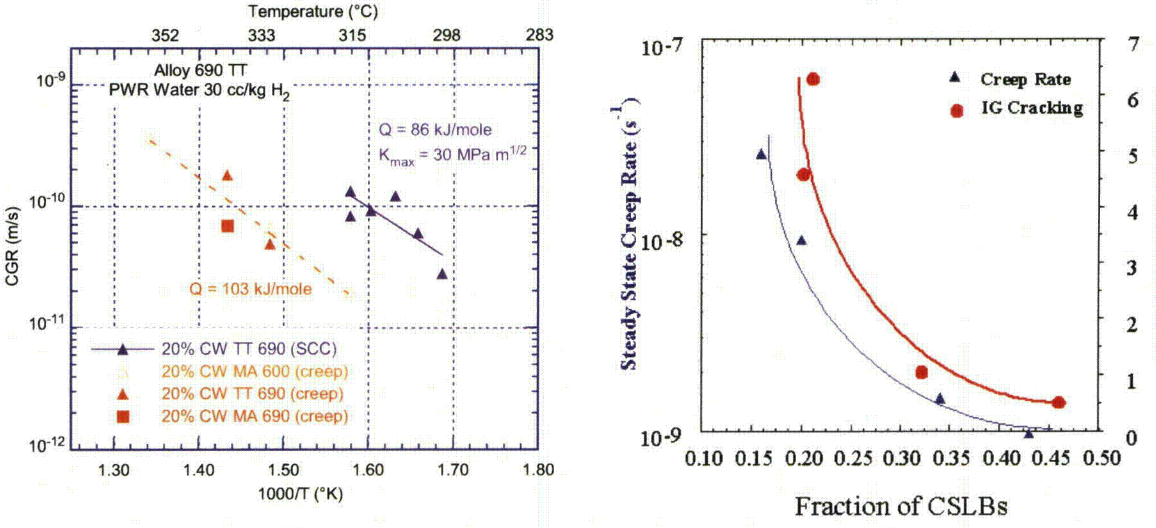

(a)　(b)

Figure 85. **(a) Temperature dependence of SCC CGR data for 20% cold-rolled Alloy 690 and creep data for Alloys 690 and 600 [43] and (b) dependence of steady-state creep at 360°C and percent cracked boundaries in primary water on the fraction of CSLBs in Ni-16Cr-9Fe alloys.[44]**

Some of the most convincing evidence that grain boundary deformation is a critical element in IG SCC stress comes from a study by Vaillant et al.,[45] in which they were able to correlate IG SCC in Alloys 600 and 690 in the MA and TT conditions tested in primary water at 360°C (680°F) to grain boundary deformation data from tests in Ar at the same temperature. Their results are summarized in Fig. 86, which provides a relationship between the crack growth rate, $\dot{a}$ (as measured in constant extension rate experiments, not fracture mechanics tests), and the grain boundary viscosity, η. The grain boundary viscosity is a function of several factors, including stress, grain size, grain boundary carbide coverage, and most importantly, grain boundary sliding rate. A direct cause-and-effect relationship between grain boundary deformation and SCC initiation for Alloy 600 was demonstrated by Alexandreanu and Was.[46] The mechanism was further supported by an analysis of the SCC crack path in Alloy 182 weld.[8]

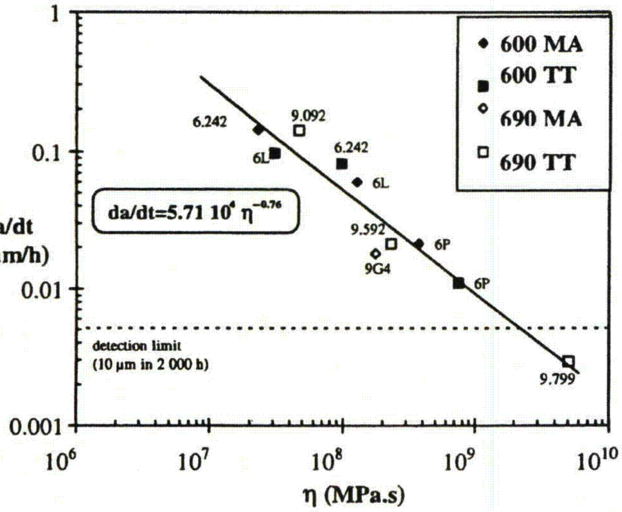

Figure 86.
Crack growth rate in Alloy 600 and 690 samples in the MA and TT conditions vs. the grain boundary viscosity, η.[45]

In the framework of a mechanism for IG SCC induced by grain boundary deformation, one can envision that those factors that significantly affect this deformation (chromium, grain boundary carbides, etc.) also affect SCC behavior. While the chromium content of the alloy is known to affect a number of processes that bear on SCC susceptibility through corrosion mechanisms, chromium is also a solid solution strengthener. The addition of chromium increases the stacking fault energy and decreases the dislocation absorption rate in the grain boundary by hindering dislocation motion. As such, in terms of mechanical behavior, the primary effect of chromium would be to suppress grain boundary cavitation and sliding, hence, SCC initiation. A high density of grain boundary carbides would reduce SCC susceptibility by hindering grain boundary sliding directly.

Cold-worked Alloy 690 showed relatively high CGRs, comparable to those for Alloy 600 in some instances (Fig. 81). In this context, the comparison drawn by Arioka et al. [43] between creep in cold-rolled Alloy 690 and Alloy 600 and CGRs in Alloy 690 and Alloy 600 is extremely significant. The parallelism indicates a similar behavior for the two alloys and, further, suggests that the mechanisms developed for Alloy 600 have a direct application to Alloy 690. It is also important to note that the increased chromium content was believed to suppress grain boundary cavitation; however, this was observed in cold-worked Alloy 690. In fact, grain boundary cavitation forms the basis of the mechanism proposed by Arioka et al.[43] to explain the high CGRs in cold-worked Alloy 690.

Based on Alloy 600 experience, the relatively high CGRs observed for cold-worked Alloy 690 can be understood in the framework of a grain-boundary-deformation-induced mechanism for SCC. The microstructural features described previously – TiN inclusions, cracked grain boundary carbides, carbide "streaks," and grain size banding – all can affect the susceptibility to grain boundary deformation. Also, TiN inclusions can impede intra-granular dislocation motion and, thus, improve creep properties. While these inclusions would benefit the overall IG SCC resistance, they are not expected to affect the grain boundaries directly. It is not clear how the "streaks" of thick grain boundary carbides might affect the SCC behavior of an alloy. In one scenario they could be expected to benefit IG SCC behavior by hindering grain boundary sliding. However, in a heavily cold-worked microstructure, those carbides could crack, creating regions with a large amount of damage both at grain boundaries and in the matrix. This effect coupled with a strain differential due to grain size banding could provide a path for SCC, perhaps in a mixed IG/TG fracture mode. Nevertheless, the one feature that would be detrimental to the IG SCC behavior is the cracked grain boundary carbides in the cold-worked materials. One can readily envision that a grain boundary with cracked carbides is more susceptible to deformation (sliding) and, therefore, more susceptible to cracking. All microstructures for which high CGR rates were measured had cracked grain boundary carbides, including the alloys cold-rolled by ANL and GE (Figs. 15 and 16). Such cracked grain boundary carbides were also observed by Arioka et al.[43] in the INSS 20% cold-rolled alloy. Finally, carbides on the grain facets on the fracture surfaces of these specimens (similar to those shown in Fig. 40 for a specimen tested at ANL) were observed by Paraventi et al.[37] in several Alloy 690 heats deformed to various levels of cold work by both cold-rolling and tensile pre-straining. It is important to note that cracked carbides on the fracture surface seem to be a unique feature of cold-worked Alloy 690 alloys, and were not observed on cold-worked Alloy 600 specimens. For example, Fig. 87 shows the fracture mode of Alloy 600 cross-rolled by 30% and tested in a similar PWR environment. The fracture mode observed for this specimen was smooth IG, with no evidence of cracked carbides of the facets.

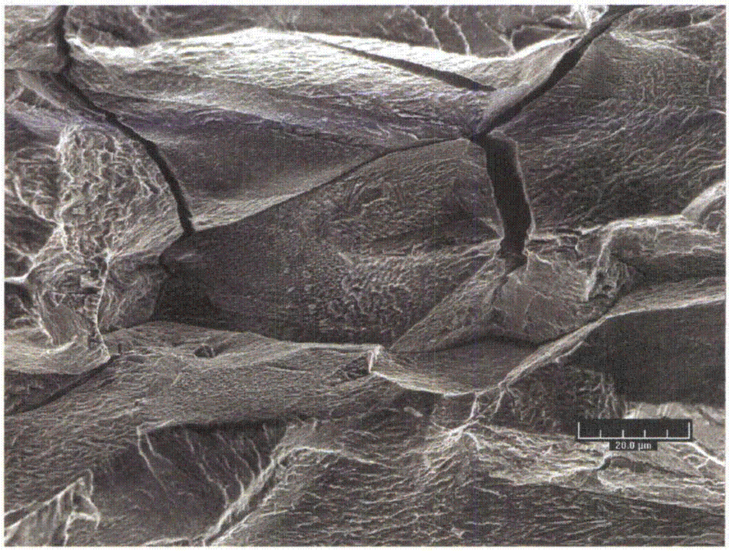

Figure 87.
Smooth IG fracture in Alloy 600 cross-rolled by 30%. Crack advance is from left to right.

The metallographic examinations reported to date show that a cold-work level as low as 20% (INSS Alloy 690)[43] can cause grain boundary carbides to crack. However, the extent of carbide cracking in these alloys is not clear. Unlike the tensile pre-strained alloy where the deformation is uniformly distributed in the material, in cold-rolled alloys, depending on the cold-work level and number of passes undertaken to achieve that level, the deformation is likely to be nonuniform. In fact, hardness measurements performed on cold-rolled alloys of interest for this program have indicated that the deformation concentrates near the surfaces in contact with the rolls (Fig. 12). Similar measurements are not available for other alloys that displayed relatively high SCC CGRs, so the microstructures and extent of grain boundary carbide cracking cannot be readily compared. Likewise, based on the limited number of metallographic examinations available, the extent of carbide cracking and SCC CGRs cannot be directly compared at this time.

5.2. Alloy 152 Weld

5.2.1 Cyclic Crack Growth Rates

A database of cyclic CGRs for Ni-alloy welds in simulated PWR environments is available from ≈120 tests conducted on Alloys 182, 82, 152, and 52 at 243-345°C (469-653°F).[42,47-49] The loading conditions for these tests include $R = 0.1\text{-}0.75$, $K_{max} = 20\text{-}100\ \mathrm{MPa{\cdot}m^{1/2}}$ ($18.2\text{-}91\ \mathrm{ksi{\cdot}in^{1/2}}$), and rise time of 0.5-5000 s. The results indicate little effect of PWR environment on the cyclic CGRs of these welds. However, only about 10% of the data was obtained under conditions for which significant environmental enhancement would be expected.

As described previously, the approach taken in ANL tests is to first determine those conditions that display environmental enhancement, and then use those conditions to transition from a TG to an IG fracture mode. For example, Fig. 88 shows the cyclic data for an Alloy 182 specimen tested previously in the program. Environmentally enhanced conditions were identified, and this specimen was transitioned successfully to an IG fracture mode. Figure 89 focuses on this transition. The images indicate that IG secondary cracks apparently preceded the interdendritic IG fracture. Similar behavior was observed on Alloy 152 specimen A152-TS-2 (Fig. 70). The IG crack (indicated by an arrow in Fig. 70) apparently initiated well ahead of the main crack front; however, it propagated sideways, toward the side groove of the specimen.

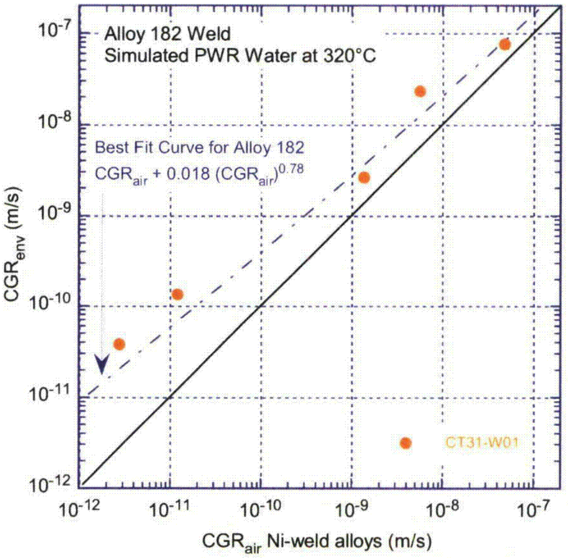

Figure 88.
Cyclic CGR data for Alloy 182 weld in PWR environment at 320°C (608°F).

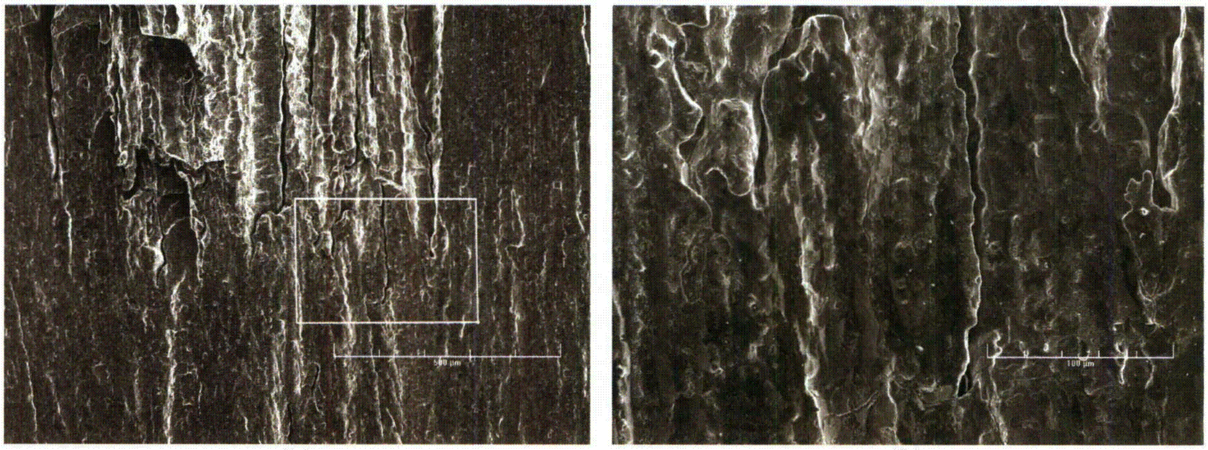

(a) (b)

Figure 89. **(a) Transition from TG to IG fracture and (b) higher magnification micrograph of the boxed area showing the tip of a few secondary cracks. Crack extension from bottom to top.**

Figure 90 shows the cyclic CGR data for the two Alloy 152 weld specimens tested in a PWR environment at 320°C (608°F). For comparison, similar cyclic CGR data obtained by Van der Sluys et al.[42] of B&W are included. The cyclic CGR data sets obtained from the two different Alloy 152 welds are in good agreement. The data resulting from the two specimens tested at ANL suggest that there exist conditions of R and rise time that lead to environmental enhancement. The conditions that resulted in environmental enhancement of cyclic CGRs in Alloy 152 are load ratios of $R \approx 0.5$ and rise times of 600-1000 s. At R values beyond 0.5 the environmental enhancement begins to diminish. When R is 0.7 and the rise time is 1000 s, the rate in the environment equals that in air, that is, the environmental enhancement appears to be completely lost. This behavior is consistent with that observed for Alloy 690 in previous tests (Figs. 78 and 80) and suggests that it may be difficult to maintain a CGR under true constant load.

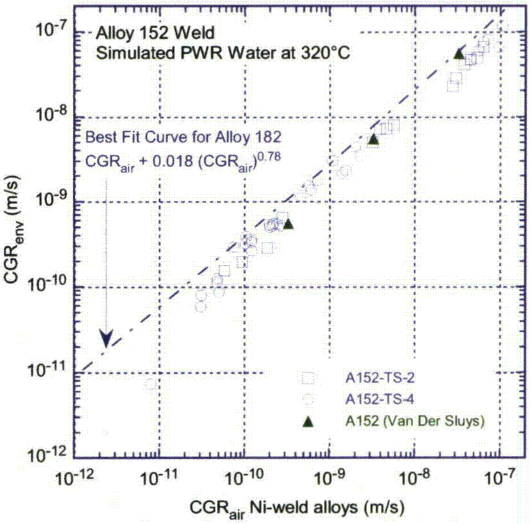

Figure 90.
Cyclic CGR data for Alloy 152 weld in PWR environment at 320°C (608°F) obtained at ANL and B&W.[42]

5.2.2 SCC Crack Growth Rates

The available SCC CGRs obtained on Alloy 152 weld are plotted as a function of stress intensity factor K in Fig. 91. The proposed 75th and 25th percentile disposition curves for Alloys 182/82 (EPRI MRP-115[24]) are also included for comparison. The plot shows the data obtained at ANL from the two tests described previously in this report. The SCC CGR data were measured at constant load (CL), measured at constant load with periodic unloading, or calculated from cycle + hold conditions (est CL). For the data obtained elsewhere,[40,38,50] the hold periods are provided in the legend. To analyze those data points that may include mechanical fatigue components, CGR$_{air}$ curves were also included. These were obtained from Eq. 11 by noting that for a constant frequency, hold time, and R, CGR$_{air}$ is a function of only K$_{max}$ and temperature.

The CGRs obtained at KAPL[40] are similar to those obtained at ANL, although the nominal K values are much higher. This similarity is remarkable given the fact that the KAPL tests did not involve any period of transitioning. The alloys used in KAPL tests contained 27.3% and 29.8% Cr, and the results suggest that this modest decrease in Cr content resulted in a two-fold increase in CGRs. The reported increase in IG SCC engagement was ten-fold. The differences in IGSCC engagement may make comparisons of CGRs tentative, but the difference in engagement may be a better measure of relative SCC susceptibility. For comparison, the Alloy 152 filler that was used for the ANL weld had a Cr content of 28.7%, and an analysis found the Cr content of the deposited weld to be 28.4%. The uncertainty in Cr content (measured by inductively coupled plasma mass spectrometry) is 5%, which is fairly large compared to the measured differences in Cr concentration. Nevertheless, these observations taken together suggest a strong dependence of SCC susceptibility on Cr content in the 27-30% range.

Figure 91 includes additional data from the experimental programs at GE[38] and Pacific Northwest National Laboratory (PNL).[50] The testing protocol used by the two laboratories was nearly identical and always used R = 0.7, f = 0.001 Hz, and 2.5-h hold as a transitioning step. For the purpose of analyzing these data sets, the air fatigue curves, CGR$_{air}$, calculated for these conditions at two temperatures, 320°C (608°F) and 350°C (662°F), are included in the plot. These CGR$_{air}$ curves are shown with dashed lines. With one exception, the CGR data with 2.5-h hold (purple open symbols) do not seem to exhibit the dependence on K expected for SCC CGRs (e.g., the disposition curves[24]), but appear to be parallel to the

CGR_{air} curve. This trend suggests that SCC is not the main driving force for these rates, which appear to be driven primarily by corrosion or mechanical fatigue. Further increases of hold times to 24 h appear to decrease the rates accordingly – a fact that substantiates the previous point. Finally, constant-load conditions confirm that the SCC components are minimal. This observation is consistent with the lack of,[38] or minimal,[50] IG engagement reported for these tests.

The proposed 25th percentile disposition curve for Alloys 182/82 (EPRI MRP-115[24]) appears to bound most of the data.

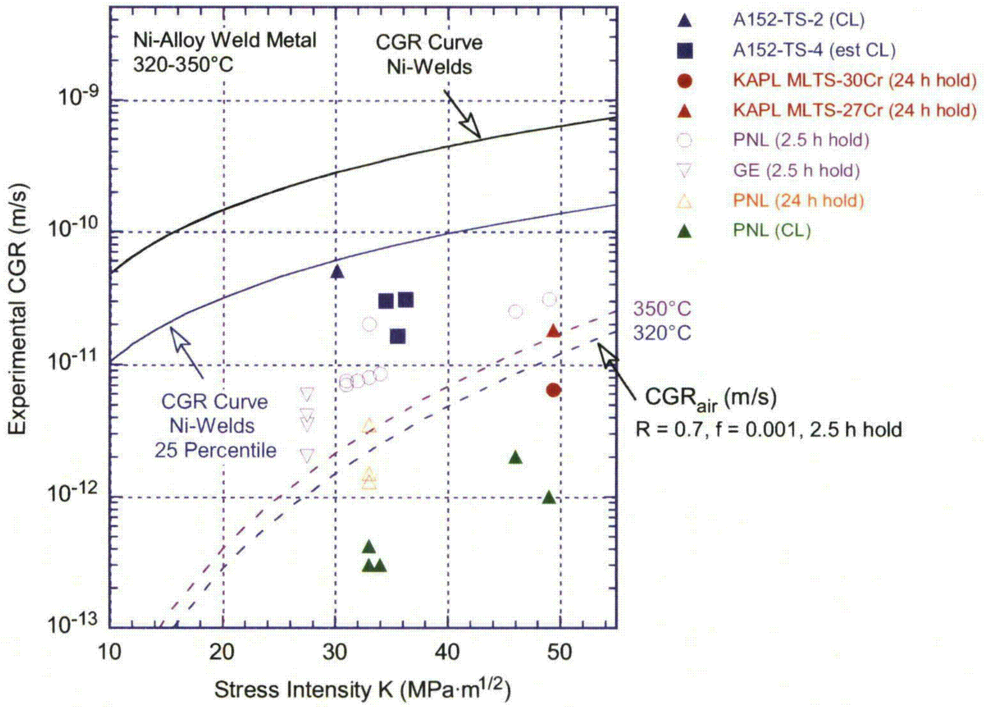

Figure 91. **SCC CGR data for Alloy 152 welds as a function of stress intensity in PWR environment.**

6. Summary

Tensile and CGR tests were performed on Alloy 690 in the cold-rolled and as-received conditions and on Alloy 152 weld in the as-welded condition. Samples were also subjected to metallographic examination. The principal findings are summarized as follows:

1. The microstructure of Alloy 690 plate cold-rolled by 26% contains TiN inclusions and cracked boundary carbides. The areas close to the two edges of the plate are decorated with carbide streaks – regions with thick grain boundary carbides. In addition, grain size banding occurs near both edges. The mid-plane of the plate – the region where the CGR tests were conducted – is free of carbide streaks and grain size banding. The CSLB fraction is approximately 28%, which is much less than is typical for a Ni-base alloy in this condition. Hence, the proportion of SCC-susceptible random boundaries is approximately 50% higher than that in a typical alloy.

2. The microstructure of CRDM Alloy 690 is typical of that of a Ni-base alloy, with equiaxed grains and dense grain boundary carbide coverage. The grain boundary character distribution is also typical of a Ni-base alloy. The CSLB fraction is approximately 53%, a large proportion of which is twins.

3. The microstructure of Alloy 152 is also typical of that for a Ni-base alloy weld, with Al-oxide inclusions. The grain boundary character distribution is also typical of a Ni-base alloy weld. The CSLB fraction is approximately 36%, a large proportion of which is low-angle boundaries.

4. The tensile properties of the alloys tested in the program over a wide temperature range 25-870°C (81-1598°F) meet the minimum requirements of ASME SB-167, and agree well with data obtained elsewhere on similar alloys. As such, the data set for Alloy 690 is in good agreement with control data on Alloy 600. In addition, the data set for Alloy 152 is in good agreement with the Alloy 82/182 tensile data obtained elsewhere.

5. The cyclic CGR data for Alloy 690 cold-rolled by 26% indicate significant environmental enhancement, comparable to that observed for Davis-Besse Alloy 600. The cyclic CGR data for the as-received alloy also indicate some environmental enhancement, although much less than that for the cold-rolled alloy. Moreover, the cyclic rates for the as-received alloy are smaller than the corrosion fatigue curve for Alloy 600. Hence, Alloy 690 in the as-received condition is expected to be more resistant to SCC than Alloy 600.

6. The SCC CGR in the PWR environment at 320°C (608°F) for Alloy 690 cold-rolled by 26% is 1-3 x 10^{-11} m/s for moderate stress intensity factors. These rates agree well with data obtained elsewhere on similar alloys deformed in the 20-32% range by either cold-rolling or tensile pre-straining. The cracked grain boundary carbides are a common feature of all cold-worked alloys that display relatively high CGR. The SCC CGR for as-received Alloy 690 is about an order of magnitude lower. These results imply that while Alloy 690 in the as-received condition is more resistant to SCC compared to Alloy 600, cold work can increase SCC susceptibility.

7. The available data on the temperature dependence of SCC CGRs obtained at ANL and elsewhere indicate that the activation energy for Alloy 690 is strongly affected by the deformation level of the alloy. Alloys in the as-received condition and at deformation levels of

up to 20% cold work appear to have an activation energy close to that for Alloy 600 (130 kJ/mol). At higher deformation levels (24-26%), the effect of temperature seems to weaken, and by 50% cold work, the temperature appears to have no effect on SCC CGRs.

8. The cyclic CGR data for the two Alloy 152 specimens tested suggest that loading conditions (load ratios of $R \approx 0.5$ and rise times of 600-1000 s) lead to environmental enhancement. At R values beyond 0.5, the environmental enhancement begins to diminish. When R is 0.7 and the rise time is 1000 s, the rate in the environment equals that in air, that is, the environmental enhancement appears to be completely lost. The enhanced rates are always lower than the corrosion fatigue curve for Alloys 82/182. Hence, it is expected that Alloy 152 is more resistant to SCC than Alloys 82/182.

9. The SCC CGRs in PWR environment at 320°C for as-welded Alloy 152 are $1.6\text{-}5 \times 10^{-11}$ m/s for moderate stress intensity factors. The 25th percentile of the proposed CGR curve for Alloys 82/182 (EPRI MRP-115) bounds the available data.

References

1. Bamford, W. H., and J. F. Hall, "A Review of Alloy 600 Cracking in Operating Nuclear Plants: Historical Experience and Future Trends," Vessel Penetration Inspection, Crack Growth and Repair Conference, Gaithersburg, MD, October 2, 2003.

2. Ruther, W. E., W. K. Soppet, and T. F. Kassner, "Corrosion Fatigue of Alloys 600 and 690 in Simulated LWR Environments," NUREG/CR-6383, ANL-95/37, April 1996.

3. Ruther, W. E., W. K. Soppet, and T. F. Kassner, "Environmentally Assisted Cracking of Alloys 600 and 690 in Simulated LWR Water," Environmentally Assisted Cracking in Light Water Reactors, Semiannual Report, July 1997-December 1997, NUREG/CR-4667, Vol. 25, ANL-98/18, pp. 42-75, September 1998.

4. Ruther, W. E., W. K. Soppet, T. F. Kassner, and W. J. Shack, "Environmentally Assisted Cracking of Alloys 600 and 690 in Simulated LWR Water," Environmentally Assisted Cracking in Light Water Reactors, Semiannual Report, January 1998-July 1998, NUREG/CR-4667, Vol. 26, ANL-98/30, pp. 25-32, March 1999.

5. Ruther, W. E., W. K. Soppet, T. F. Kassner, and W. J. Shack, "Environmentally Assisted Cracking of Alloys 600 and 690 in Simulated LWR Water," Environmentally Assisted Cracking in Light Water Reactors, Semiannual Report, July 1998-December 1998, NUREG/CR-4667, Vol. 27, ANL-99/11, pp. 45-54, October 1999.

6. Soppet, W. K., O. K. Chopra, and W. J. Shack, "Environmentally Assisted Cracking of Alloys 600 and 690 in Simulated LWR Water," Environmentally Assisted Cracking in Light Water Reactors, Semiannual Report, July 1999-December 1999, NUREG/CR-4667, Vol. 29, ANL-00/23, pp. 39-45, November 2000.

7. Chopra, O. K., W. K. Soppet, and W. J. Shack, "Effects of Alloy Chemistry, Cold Work, and Water Chemistry on Corrosion Fatigue and Stress Corrosion Cracking of Nickel Alloys and Welds," NUREG/CR-6721, ANL-01/07, April 2001.

8. Alexandreanu, B., O. K. Chopra, and W. J. Shack, "Crack Growth Rates of Nickel Alloy Welds in a PWR Environment," NUREG/CR-6907, ANL-04/3, May 2006.

9. Alexandreanu, B., O. K. Chopra, and W. J. Shack, "Crack Growth Rates of Nickel Alloys from the Davis-Besse and V. C. Summer Power Plants in a PWR Environment," NUREG/CR-6921, ANL-05/55, November 2001.

10. American Society for Testing and Materials, "Standard Test Method for Measurement of Fatigue Crack Growth Rates," ASTM E647-08, DOI 10.1520/E0647-08, West Conshohocken, PA, 2008.

11. American Society for Testing and Materials, "Standard Test Method for Determining a Threshold Stress Intensity Factor for Environment-Assisted Cracking of Metallic Materials," ASTM E1681-03, DOI 10.1520/E1681-03R08, West Conshohocken, PA, 2008.

12. Electric Power Research Institute, "PWR Primary Water Chemistry Guidelines," Volume 1, Revision 4, TR-105714-V1R4, Palo Alto, CA, 1999.

13. Macdonald, D. D., A. C. Scott, and P. Wentrcek, "External Reference Electrodes for Use in High Temperature Aqueous Systems," J. Electrochem. Soc., 126, pp. 908-911, 1979.

14. Attanasio, S. A., and D. S. Morton, "Measurement of the Nickel/Nickel Oxide Transition in Ni-Cr-Fe Alloys and Updated Data and Correlations to Quantify the Effect of Aqueous Hydrogen on Primary Water SCC," Proc. 11th Intl. Conf. on Environmental Degradation of Materials in Nuclear Power Systems--Water Reactors, NACE International, Houston, TX, 2003.

15. Attanasio, S. A., D. S. Morton, M. A. Ando, N. F. Panayotou, and C. D. Thompson, "Measurement of the Nickel/Nickel Oxide Phase Transition in High Temperature Hydrogenated Water Using the Contact Electric Resistance (CER) Technique," Proc. Tenth Intl. Conf. on Environmental Degradation of Materials in Nuclear Power Systems--Water Reactors, NACE International, Houston, TX, 2001.

16. Morton, D. S., S. A. Attanasio, and G. A. Young, "Primary Water SCC Understanding and Characterization Through Fundamental Testing in the Vicinity of the Nickel/Nickel Oxide Phase Transition," Proc. Tenth Intl. Conf. on Environmental Degradation of Materials in Nuclear Power Systems--Water Reactors, NACE International, Houston, TX, 2001.

17. Andresen, P. L., and P. G. Campbell, "The Effects of Crack Closure in High-Temperature Water and its Role in Influencing Crack Growth Data," Proc. of the Fourth Intl. Symp. on Environmental Degradation of Materials in Nuclear Power Systems--Water Reactors, D. Cubicciotti, ed., NACE International, Houston, TX, pp. 4.86-4.111, 1990.

18. Cassagne, T. B., and A. Gelpi, "Crack Growth Rate Measurements on Alloy 600 Steam Generator Tubes in Steam and Primary Water," Proc. of the Fifth Intl. Symp. on Environmental Degradation of Materials in Nuclear Power Systems--Water Reactors, American Nuclear Society, La Grange Park, IL, pp. 518-524, 1991.

19. Foster, J. P., W. H. Bamford, and R. S. Pathania, "Initial Results of Alloy 600 Crack Growth Rate Testing in a PWR Environment," Proc. of the Seventh Intl. Symp. on Environmental Degradation of Materials in Nuclear Power Systems--Water Reactors, NACE International, Houston, TX, pp. 25-39, 1995.

20. Magdowski, R., F. Vaillant, C. Amzallag, and M. O. Speidel, "Stress Corrosion Crack Growth Rates of Alloy 600 in Simulated PWR Coolant," Proc. of the 8th Intl. Symp. on Environmental Degradation of Materials in Nuclear Power Systems--Water Reactors, S. M. Bruemmer, ed., American Nuclear Society, La Grange Park, IL, pp. 333-338, 1997.

21. Le Hong, S., C. Amzallag, and A. Gelpi, "Modeling of Stress Corrosion Crack Initiation on Alloy 600 in Primary Water of PWRs," Proc. of the Ninth Intl. Symp. on Environmental Degradation of Materials in Nuclear Power Systems--Water Reactors, F. P. Ford, S. M. Bruemmer, and G. S. Was, eds., Minerals, Metals, and Materials Society, Warrendale, PA, pp. 115-122, 1999.

22. Raquet, O., and G. Santarini, "Stress Corrosion Crack Propagation Rate of Alloy 600 in the Primary Water of PWR Influence of a Cold Worked Layer," Proc. of the Ninth Intl. Symp. on Environmental Degradation of Materials in Nuclear Power Systems--Water Reactors, F. P. Ford, S. M. Bruemmer, and G. S. Was, eds., Minerals, Metals, and Materials Society, Warrendale, PA, pp. 207-213, 1999.

23. Electric Power Research Institute, "Materials Reliability Program (MRP) Crack Growth Rates for Evaluating Primary Water Stress Corrosion Cracking (PWSCC) of Thick-Wall Alloy 600 Materials (MRP-55)," Revision 1, 1006695, Palo Alto, CA, 2002.

24. Electric Power Research Institute, "Materials Reliability Program Crack Growth Rates for Evaluating Primary Water Stress Corrosion Cracking (PWSCC) of Alloy 82, 182, and 132 Welds (MRP-115)," 1006696, Palo Alto, CA, 2004.

25. Norring, K., J. Engstrom, and P. Norberg, "Intergranular Stress Corrosion Cracking in Steam Generator Tubing: Testing of Alloy 690 and Alloy 600 Tubes," Proc. of the Third Intl. Symp. on Environmental Degradation of Materials in Nuclear Power Systems--Water Reactors, G. J. Theus and J. R. Weeks, eds., Metallurgical Society, Warrendale, PA, p. 587, 1988.

26. Norring, K., J. Engstrom, and H. Timblom, "Intergranular Stress Corrosion Cracking of Steam Generator Tubing: 25000 Hours of Testing of Alloy 690 and Alloy 600 Tubes," Proc. of the Fourth Intl. Symp. on Environmental Degradation of Materials in Nuclear Power Systems--Water Reactors, D. Cubicciotti, ed., NACE International, Houston, TX, pp. 12-1, 1990.

27. Was, G. S. and K. Lian, "Role of Carbides in Stress Corrosion Cracking Resistance of Alloy 600 and Controlled-Purity Ni-16% Cr-9% Fe in Primary Water at 360 Degrees C," Corrosion, 54 (9), p. 675, 1998.

28. Hertzberg, J. L. and G. S. Was, "Isolation of Carbon and Grain Boundary Carbide Effects on the Creep and Intergranular Stress Corrosion Cracking Behavior of Ni-16Cr-9Fe-xC Alloys in 360 Degrees C Primary Water," Metallurgical and Materials Transactions A, 29 (3A), pp. 1035-1046, 1998.

29. Palumbo, G., K. T. Aust, E.M. Lehockey, U. Erb, and P. Lin, "On a More Restrictive Geometric Criterion for 'Special' CSL Grain Boundaries," Acta Metallurgica, 14, pp. 1685-1690, 1998.

30. Was, G., V. Thaveeprungsriporn, and D. C. Crawford, "Grain Boundary Misorientation Effects on Creep and Cracking in Ni-Based Alloys," Journal of Materials, 50 (2), pp. 44-49, 1998.

31. Alexandreanu, B., B. Capell, and G. S. Was, "Combined Effect of Special Grain Boundaries and Grain Boundary Carbides on IGSCC of Ni-16Cr-9Fe-xC Alloys," Materials Science and Engineering A, 300, pp. 94-104, 2001.

32. Lehockey, E. M., G. Palumbo, and P. Lin, "Improving the Weldability and Service Performance of Nickel- and Iron-Based Superalloys by Grain Boundary Engineering," Metallurgical and Materials Transactions, 29 (12), pp. 369-379, 1998.

33. Palumbo, G., P. J. King, and K. T. Aust, "Grain Boundary Design and Control for Intergranular Stress Corrosion Resistance," Scripta Metallugica et Materialia, 25 (8), pp. 1775-1780, 1991.

34. Cheung, C., U. Erb, and G. Palumbo, "Application of Grain Boundary Engineering Concepts to Alleviate Intergranular Cracking in Alloys 600 and 690," Materials Science and Engineering A, 185, pp. 39-43, 1994.

35. Pan, Y., B. L. Adams, T. Olson, and N. Panayotou, "Grain-Boundary Structure Effects on Intergranular Stress Corrosion Cracking of Alloy X-750," Acta Materialia, 44 (12), pp. 4685-4695, 1996.

36. Lehockey, E. M., A. M. Brennenstuhl, and I. Thompson, "On the Relationship between Grain Boundary Connectivity, Coincident Site Lattice Boundaries, and Intergranular Stress Corrosion Cracking," Corrosion Science, 46, pp. 2383-2404, 2004.

37. Paraventi, D. J., and W. C. Moshier, "Alloy 690 SCC Growth Rate Testing," Proc. Workshop on Cold Work in Iron- and Nickel-Base Alloys, R.W. Staehle and J. Gorman, eds., Electric Power Research Institute, Palo Alto, CA, June 2007.

38. Andresen, P.L., M. M. Morra, A. Ahluwalia and J. Wilson "Effect of Deformation and Orientation on SCC of Alloy 690", Proc. of the 14th Intl. Conference on Environmental Degradation of Materials in Nuclear Power Systems--Water Reactors, Virginia Beach, VA, August 23-27, 2009.

39. American Society for Testing and Materials, "Standard Test Methods for Tension Testing of Metallic Materials," ASTM E8/ E8M-09, DOI 10.1520/E0008_E0008M-09, West Conshohocken, PA, 2009.

40. Etien, R., G. Young, J. Mullen, and T. Capobianco, EPRI 690 Meeting, St. Petersburg, FL, November 8-9, 2007.

41. Mintz, T. S., Y. V. Bhargava, S. A. Thorne, R. Chopdekar, V. Radmilovic, Y. Suzuki, and T. M. Devine, "Electrochemical Synthesis of Functionalized Nickel Oxide Nanowires," Electrochemical and Solid-State Letters, 8 (9), pp. D26–D30, 2005.

42. Van Der Sluys, W. A., B. A. Young, and D. Doyle, "Corrosion Fatigue Properties on Alloy 690 and Some Nickel-Based Weld Metals," Assessment Methodologies for Preventing Failure: Service Experience and Environmental Considerations, PVP Vol. 410-2, R. Mohan, ed., American Society of Mechanical Engineers, New York, pp. 85-91, 2000.

43. Arioka, K., T. Yamada, T. Miyamoto, and T. Terachi, "Dependence of Stress Corrosion Cracking of Alloy 690 on Temperature, Cold Work, and Carbide Precipitation—Role of Diffusion of Vacancies at Crack Tips", Corrosion 67, 035006, 2011.

44. Was, G., V. Thaveeprungsriporn, and D. C. Crawford, "Grain Boundary Misorientation Effects on Creep and Cracking in Ni-Based Alloys," Journal of Materials, 50 (2), pp. 44-49, 1998.

45. Vaillant, F., J.-D. Mithieux, O. de Bouvier, D. Vacon, G. Zacharie, Y. Brechet, and F. Louchet, "Influence of Chromium Content and Microstructure on Creep and PWSSC Resistance of Nickel Base Alloys," Proc. of the Ninth Intl. Symp. on Environmental Degradation of Materials in Nuclear Power Systems--Water Reactors, F. P. Ford, S. M. Bruemmer, and G. S. Was, eds., Minerals, Metals, and Materials Society, Warrendale, PA, pp. 251-258, 1999.

46. Alexandreanu, B., and G. S. Was, "Grain Boundary Deformation-Induced Intergranular Stress Corrosion Cracking of Ni-16Cr-9Fe in 360°C Water," Corrosion, 59 (8), pp. 705, 2003.

47. Amzallag, C., G. Baudry, and J. L. Bernard, "Effects of PWR Environment on the Fatigue Crack Growth of Different Stainless Steels and Inconel Type Alloy," Proc. IAEA Specialists Meeting on Subcritical Crack Growth, NUREG/CP-0044, Vol. 1, pp. 263-294, 1983.

48. James, L. A., and W. J. Mills, "Fatigue-Crack Propagation Behavior of Wrought Alloy 600 and Weld-Deposited EN82H in an Elevated Temperature Aqueous Environment," Service Experience, Structural Integrity, Severe Accident, and Erosion in Nuclear and Fossil Plants, PVP Vol. 303, American Society of Mechanical Engineers, pp. 21-36, 1995.

49. Lindstrom, R., P. Lidar, and J. Lagerstrom, "Crack Growth of Alloy 182 in Simulated Primary Side PWR Environment," Proc. of the 8th Intl. Symp. on Environmental Degradation of Materials in Nuclear Power Systems--Water Reactors, S. M. Bruemmer, ed., American Nuclear Society, La Grange Park, IL, pp. 422-429, 1997.

50. Toloczko M. B., and S. M. Bruemmer, "Crack Growth Response of Alloy 152 and 52 Weld Metals in Simulated PWR Primary Water," Proc. of the 14th Intl. Conference on Environmental Degradation of Materials in Nuclear Power Systems--Water Reactors, Virginia Beach, VA, August 23-27, 2009.

NRC FORM 335
(12-2010)
NRCMD 3.7

U.S. NUCLEAR REGULATORY COMMISSION

BIBLIOGRAPHIC DATA SHEET

(See instructions on the reverse)

1. REPORT NUMBER
(Assigned by NRC, Add Vol., Supp., Rev., and Addendum Numbers, if any.)
NUREG/CR-7137

2. TITLE AND SUBTITLE
Stress Corrosion Cracking in Nickel-Base Alloys 690 and 152 Weld in Simulated PWR Environment - 2009

3. DATE REPORT PUBLISHED

MONTH	YEAR
June	2012

4. FIN OR GRANT NUMBER

5. AUTHOR(S)
B. Alexandreanu, Y. Yang, Y. Chen, and W. J. Shack

6. TYPE OF REPORT
Technical

7. PERIOD COVERED (Inclusive Dates)
5/2006 to 9/2009

8. PERFORMING ORGANIZATION - NAME AND ADDRESS (If NRC, provide Division, Office or Region, U. S. Nuclear Regulatory Commission, and mailing address; if contractor, provide name and mailing address.)
Argonne National Laboratory
Nuclear Engineering Division
9700 S. Cass Avenue
Argonne, IL 60439

9. SPONSORING ORGANIZATION - NAME AND ADDRESS (If NRC, type "Same as above", if contractor, provide NRC Division, Office or Region, U. S. Nuclear Regulatory Commission, and mailing address.)
Division of Engineering,
Office of Nuclear Regulatory Research,
U.S. Nuclear Regulatory Commission,
Washington, DC 20555-0001

10. SUPPLEMENTARY NOTES

11. ABSTRACT (200 words or less)

Alloys 690 and 152 are the replacement materials pressurized water reactors (PWRs) for Alloys 600 and 182 that have been found to undergo stress corrosion cracking (SCC). The objectives of this work were to determine the crack growth rates (CGRs) in a simulated PWR water environment and obtain tensile data as a function of temperature for the replacement alloys. Compared to Alloy 600, the as-received Alloy 690 proved to be more resistant to SCC in the simulated PWR environment at 320°C (608 °F). However after cold rolling, the SCC CGRs increased by an order of magnitude compared to as-received Alloy 690. The environmental enhancement of cyclic CGRs for Alloy 152 was minimal and SCC CGR rates for the higher chromium weld metal in the simulated PWR environment at 320°C (608 °F), was about an order of magnitude lower than the typical SCC CGR measured for Alloy 182. Tensile test data for Alloy 690 and Alloy 152 welds in the temperature range of 25-870°C (81-1598°F) meet the minimum requirements of ASME SB-167, and are in agreement with data on similar alloys.

12. KEY WORDS/DESCRIPTORS (List words or phrases that will assist researchers in locating the report.)

alloy 690
alloy 152
primary water stress corrosion cracking
crack growth rate
tensile test data
pressurized water reactor

13. AVAILABILITY STATEMENT
unlimited

14. SECURITY CLASSIFICATION
(This Page)
unclassified
(This Report)
unclassified

15. NUMBER OF PAGES

16. PRICE

UNITED STATES
NUCLEAR REGULATORY COMMISSION
WASHINGTON, DC 20555-0001

OFFICIAL BUSINESS

NUREG/CR-7137

Stress Corrosion Cracking in Nickel-Base Alloys 690 and 152 Weld in Simulated PWR Environment - 2009

June 2012